CARBON NANOSTRUCTURES-QUANTUM DOT HYBRIDS: SELF-ASSEMBLY AND PHOTO-PHYSICAL INVESTIGATIONS OF SINGLE-MOLECULE HETEROSTRUCTURES

Antonio Attanzio

Supervised by Dr Matteo Palma

School of Biological and Chemical Sciences

Queen Mary University of London

July 2018

This dissertation is submitted for the degree of Doctor of Philosophy

DECLARATION

I, Antonio Attanzio, confirm that the research included within this thesis is my own work or that where it has been carried out in collaboration with, or supported by others, that this is duly acknowledged below and my contribution indicated. Previously published material is also acknowledged below.

I attest that I have exercised reasonable care to ensure that the work is original, and does not to the best of my knowledge break any UK law, infringe any third party's copyright or other Intellectual Property Right, or contain any confidential material.

I accept that the College has the right to use plagiarism detection software to check the electronic version of the thesis.

I confirm that this thesis has not been previously submitted for the award of a degree by this or any other university.

Signature: 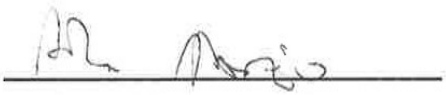

Date: 2/11/2018

PUBLICATIONS

Antonio Attanzio, Andrei Sapelkin, Felice Gesuele, Arend van der Zande, William P. Gillin, Ming Zheng, and Matteo Palma, "Carbon Nanotube-Quantum Dot Nanohybrids: Coupling with Single-Particle Control in Aqueous Solution", *Small*, **2017**, 13, 1603042.

Mark Freeley, Antonio Attanzio, Alessandro Cecconello, Giuseppe Amoroso, Pierrick Clement, Gustavo Fernandez, Felice Gesuele, and Matteo Palma, "Tuning the Coupling in Single-Molecule Heterostructures: DNA-Programmed and Reconfigurable Carbon Nanotube-Based Nanohybrids", *Adv. Sci., Submitted.*

Antonio Attanzio, Martin Rosillo-Lopez, Andrea Zampetti, Ioannis Ierides, Franco Cacialli, Christoph G. Salzmann and Matteo Palma, "Graphene Nanoflakes-quantum dots hybrids in aqueous solution", *Submitted.*

ABSTRACT

The possibility of integrating materials with different properties into heterostructures is crucial in the field of nanotechnology and can lead to new functionalities and emergent behaviour at the interfaces. In this regard, whereas semiconductor quantum dots (QDs) are tuneable emitters and efficient broadband light harvesting systems for new generation photovoltaic devices and light-emitting diodes, carbon nanomaterials are ideal scaffolds to collect and transport charges for device implementation. Therefore, the combination of carbon nanomaterials and QDs into novel nanohybrid structures has drawn interdisciplinary attention for a wide range of applications including photovoltaics, photocatalysis, sensing, bioimaging, and quantum information processing.

In this thesis, the assembly, via covalent approaches, of semiconductor quantum dots with carbon-based nanomaterials in solution and at the single-molecule level is reported. First, a controlled assembly strategy for the formation of carbon nanotube-quantum dot nanohybrids is presented, where the terminal ends of individual single-walled carbon nanotubes (SWCNTs) were selectively functionalised with single semiconductor quantum dots. This was followed by a further study of these heterostructures, where different bridging linkers were used to control the electronic coupling between the two nanomoieties. Notably, the assembly, in environmentally friendly and biocompatible aqueous solution, was controlled towards the formation of monofunctionalized SWCNT-QD structures. Additionally, photo-physical investigations in solution and at the single-molecule level allowed us to cast light on the electronic coupling between the two components of the heterostructures.

We further developed a covalent assembly strategy for the formation of semiconductor quantum dot-graphene hybrids, and we explored the application of these nanohybrids in a solar cell device. Atomic force microscopy was used to image the nanostructures and allowed us to identify the morphology of the nanohybrids investigated, while photoluminescence studies were employed to assess the light induced processes at the interface.

Finally, we present an approach to investigate the chemical groups present at the edges of graphene pre-patterned nanogaps - generated by electroburning - where selective reactions for specific chemical groups carboxyl groups (COOH), aldehyde groups (CHO) and hydroxyl groups (OH)) were carried out towards the attachment of QDs, allowing to

indirectly locate and identify, via AFM, the chemical groups for the specific reaction performed.

By and large, the strategies developed in this work contribute to the tailored fabrication of nanohybrid materials with single-particle control, an important feature in the design of novel QD-based optoelectronic and light-energy conversion devices.

ACKNOWLEDGEMENTS

I would like to thank my supervisor Dr Matteo Palma for giving me the opportunity to work in his group, it has been a great pleasure to work with him, always working in a supportive and scientific stimulating atmosphere, he helped me to be become a better scientist.

I want to thank all the members of my group, Dr Mark Freeley, Dr Da Huang, Dr Jingyuan Zhu, Dr Joseph McMorrow, Sandra Perez-Garrido, Dr Pierrick Clement, Dr Keitel Cenvantes Salguero, Xinzhao Xu, Giuseppe Amoroso, Qingyu Ye, Dr Alessandro Cecconello and William Hawkes.

I am also grateful to the different research groups that collaborated to the work presented here. In particular I would like to thank: Dr Felice Gesuele from the University of Naples; Dr Andrei Sapelkin and Prof William Gillin, from Queen Mary University of London for their contribution in the photo-physical characterization of QD-CNT nanohybrids; Dr Rachel Crespo-Otero and Prof Tovy Vlcek from Queen Mary University of London for useful discussions on fluorescence data interpretations; Dr Ken Scott and Dr Jianxu Hu from Queen Mary University of London for their help in time resolved fluorescence measurements; Dr Chris Jones from Queen Mary University of London for useful discussions about organic chemistry and reaction mechanisms; Dr Christoph Salzmann and Dr Martin Rosillo-Lopez from University College London for the synthesis of the graphene nanoflakes and Raman measurements; Dr Jan Mol and Dr Xinya Bian from the University of Oxford for the graphene electrodes fabrication; Dr Andrea Zampetti, Prof Franco Cacialli and Ioannis Ierides from University College London for the solar cell devices fabrication and photocurrent measurements.

TABLE OF CONTENTS

LIST OF TABLES

LIST OF FIGURES

LIST OF ABBREVIATIONS AND ACRONYMS

0D zero dimensional

1D one dimensional

2D two dimensional

3D three dimensional

A adenine

AFM atomic force microscopy

bp base pair

C cytosine

C60 fullerene

CNT carbon nanotubes

CS core shell

CT charge transfer

CVD chemical vapor deposition

DMF Dimethylformamide

DPBS Dulbecco's phosphate buffered saline

DNA deoxyribonucleic acid

DSC *N*,*N*-Disuccinimidyl carbonate

dsDNA double strand DNA

EDC 1-ethyl-3-(3-dimethylaminopropyl) carbodiimide hydrochloride

e-h electron-hole pair

EtOH ethanol

FRET fluorescence resonance energy transfer

FTIR Fourier transform infrared spectroscopy

GNF graphene nanoflakes

G guanine

G conductance

GO graphene oxide

HEPES 4-(2-hydroxyethyl)-1-piperazineethanesulfonic acid

HOMO highest occupied molecular orbital

I current

IR infrared

IRF instrument response function

I-V current-voltage

LUMO lowest unoccupied molecular orbital

MES 2-(N-morpholino) ethanesulfuric acid

MWCNT multi walled carbon nanotubes

NC nanocrystal

NHS N-hydroxysuccunimide

PL photoluminescence

PMT photomultiplier tube

QD quantum dots

QY quantum yield

rGO reduced graphene oxide

SEC size exclusion chromatography

SLG single layer graphene

S-NHS (sulfo-NHS) N-hydroxysufosuccinimide

ssDNA single strand DNA

SSPL stationary state photoluminescence

SWCNT single walled carbon nanotubes

T Thymine

TRPL time-resolved photoluminescence

UV ultra violet

UV-vis Ultraviolet-visible

V voltage

1 INTRODUCTION

In the last few decades, there has been a great interest in the field of nanoscience and nanotechnology;[1] different nanoscale materials and nanostructures have been developed showing unique optical, electronic, thermal, and mechanical properties. As a result of the quantum confinement within nanoscale domains, and due to a relatively low number of atoms or molecules,[2] the chemical and physical properties of nanomaterials are considerably altered compared to the corresponding bulk materials. Moreover, nanomaterials allowed the development of nanoscale devices providing not only a way to scale down, in terms of dimensions, conventional technology, but also providing a route to cheaper and more environmentally friendly production. In this regard, mimicking nature's efficient way of building sophisticated materials and structures via (self)assembly[3] has shown to be a valuable strategy for the fabrication of nanoscale and microscale materials and devices, via a so called "bottom-up" approach.

Several aspects arise when materials are scaled down to nanometer dimensions, such as the exponential increase in the specific surface area of the material itself; these affect the materials' efficiency and sensitivity for different applications including catalysis, energy conversion, electrochemistry, and environmental chemistry.[4] In this regard, the ability to synthesizing materials with monodisperse sizes, uniform morphologies, and functionalized surfaces results in a fully controlled synthetic pathway which can accurately match the requirements for a specific application. Moreover, the integration of two or more components into functional heterostructures, provides not only a way to combine materials with different properties but in many cases the resulting hybrids show novel properties different from those of their individual constituents.

The unique, innovative, and important aspect of this high control over the physical-chemical properties of individual nanostructures allows further investigation over the junction interfaces, whose properties are inherently manipulable, tailorable, and hence, predictable. In this regard a crucial aspect is represented by the synergistic effects that arise when different components are combined into hybrid frameworks and hence the role played by the interface towards the optimization of the hybrids characteristics: a narrow interface can promote charge and energy transfer processes while strong interactions will improve cyclability and longer device life-time. Therefore, a rational design of nanomaterials is a critical aspect to understand and tailor electronic structures, carrier trapping and delocalization as well as charge transport processes for optoelectronic applications; this is essential for the incorporation of nanomaterials as building blocks in actual devices.[5,6]

Within the large number of possible combinations of materials with different characteristics, organic-inorganic interfaces have emerged as promising nano-hybrids materials:[7,8] semiconductive and metallic nanoparticles have been widely used as light sensitive components, while carbon based nanostructures have been shown to be ideal functional scaffolds as nanoscale electrodes to collect and transport charges.

Carbon based nanomaterials have been studied and researched for at least 50 years,[9] either as unwanted side products or as specifically synthetized materials. However only after the discovery of fullerene, carbon nanomaterials have developed as an autonomous research area, and only after the first reports of large scale production of the carbon materials [fullerene 1990, nanotubes 1992] the research in this field increased significantly.[10,11] Nanocarbon materials include carbon nanotubes (CNTs), graphene (G) and other fullerene analogues such as C60, which are dimensionally confined sp2 bonded carbonaceous materials of the nanocarbon family. Their unique and exceptional properties, like high surface area, thermal stability and conductivity, electron mobility, and Young's modulus, depend upon many factors such as nanocarbon size, number of walls/layers, concentration and type of defects and synthetic strategy of production. It is not surprising that uncoupled/pristine nanocarbon materials have been studied and employed for a huge number of applications including transistors,[12] shape recovery,[13] loud speakers,[14] and supercapacitors.[15] However, a further improvement in the performances of these devices can be achieved by functionalizing them with a second or third material with the further possibility to increase their range of applications from catalysis and sensors, to energy storage and conversion.[16] This thesis will focus on the

assembly and photo-physical characterization of carbon-based functional heterostructures. In particular, carbon nanotubes and graphene have been employed in the assembly of organic-inorganic interfaces where the nanocarbon moiety would act as a nanoscale electrode while the inorganic part, i.e. semiconductor quantum dots, would act as the active component in photo-electronic based systems (and potentially devices).

Although at the early stage of research, carbon based-inorganic nanostructures have shown remarkable performances exhibiting an enhanced ability to trap electrons and reduce the electron-hole recombination rate, compared to the bulk materials, for photovoltaic applications.[16,17] Moreover, they can also serve as additional photosensitizers in photocatalysts or intrinsic capacitors in supercapacitors and batteries,[16] hence this new class of materials offers great potential for use in a wide variety of applications due to their diversity and adaptability. Considering the outstanding results of previous studies, carbon nanostructures-inorganic hybrids will certainly play a role in the future development of advanced functional materials.

In this thesis are presented strategies for the assembly in solution of carbon nanomaterials-QD heterostructures at the single-molecule level, and their photo-physical characterization in order to investigate the light induced processes at the interface. Chapter 1 describes the principle behind the materials investigated in this thesis, i.e. carbon nanomaterials including carbon nanotubes, graphene and semiconductor quantum dots, focusing on their properties and features. Chapter 2 describes the experimental techniques. Chapter 3 focuses on the self-assembly and photo-physical characterization of carbon nanotubes-quantum dots hybrids where single nanoparticles are attached selectively at the terminal ends of single walled carbon nanotubes. The assembly is carried out in aqueous solution and the photo-physical characterizations are performed also with single particle resolution. Chapter 4 describes a series of investigations focused on how the nature of the linkers bridging the QD and CNTs in the hybrids affects the degree of the electronic coupling between the two moieties: alkynes and aromatic linkers were employed as well as DNA as a molecular ruler. Chapter 5 describes the assembly and photo-physical characterizations of QD-graphene nanoflakes in aqueous solution, and the application of such nanohybrids in solar cell devices. Chapter 6 describes the strategy for the tethering of QDs to pre-patterned graphene electrodes on surfaces, and how this procedure allows the investigation of the chemical groups present at the graphene nanoelectrodes edges. Finally, the work developed in this thesis is summarized in Chapter 7, where future challenges in the field are discussed.

1.1 Graphene

1.1.1 Properties of Graphene

Although graphene has been studied theoretically for over seventy years[18,19] and widely used to describe the properties of several carbon materials, its experimental discovery is quite recent.[20,21] Graphene is the basic building block for all the graphitic materials in all dimensionalities: it can be wrapped up to form fullerenes where carbon atoms are arranged spherically (0D), rolled along a given direction to form nanotubes (1D) or stacked of several layers that are weakly coupled by van der Waals forces to form graphite (3D).[22]

Graphene is a monolayer of carbon atoms tightly packed into a two-dimensional honeycomb lattice made out of hexagons and can be thought of as composed of benzene rings stripped out from their hydrogen atoms.[23] Graphene structure is shown in **Figure 1**, and it can be seen as a triangular lattice with a basis of two atoms per unit cell described by the two lattice vectors a_1 and a_2, with a carbon-carbon distance $a \approx 1.42$ Å, and with reciprocal lattice vectors b_1 and b_2 (**Figure 1**).

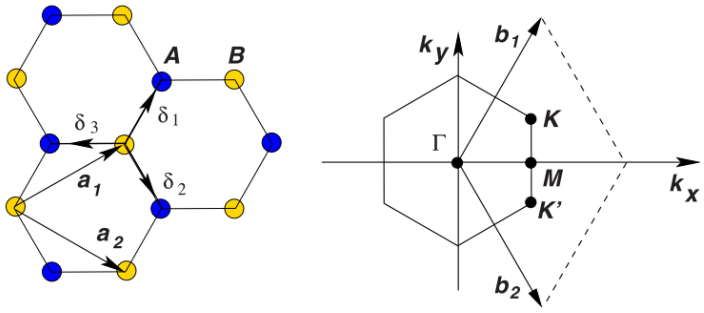

Figure 1*:Graphene honeycomb lattice (left) and its Brillouin zone (right).(taken from ref* 23*).*

Every carbon atom has four valence electrons, one 2s electron and three 2p electrons and the hexagonal lattice of graphene can be represented through a sp2 hybridazation between the s orbital and two p orbitals leading to a trigonal planar structure with the formation of a σ bond between carbon atoms which is responsible for the robustness of the lattice structure in all allotropes. The remaining p orbital is perpendicular to the planar structure

and form π bonds with neighbouring carbon atoms leading to the formation of a band where delocalized electrons allow the conduction of an electrical current. The full band structure of graphene is represented in **Figure 2** in function of the momentum k and it is characterized by a conduction and valence band that connect each other at certain points. These points lie at the Fermi energy and correspond to the K and K' point at the corners of the Brillouin zone, hence there is no gap, like for insulator, but no partially filled band either, like metals, therefore the semimetallic nature of graphene.[24]

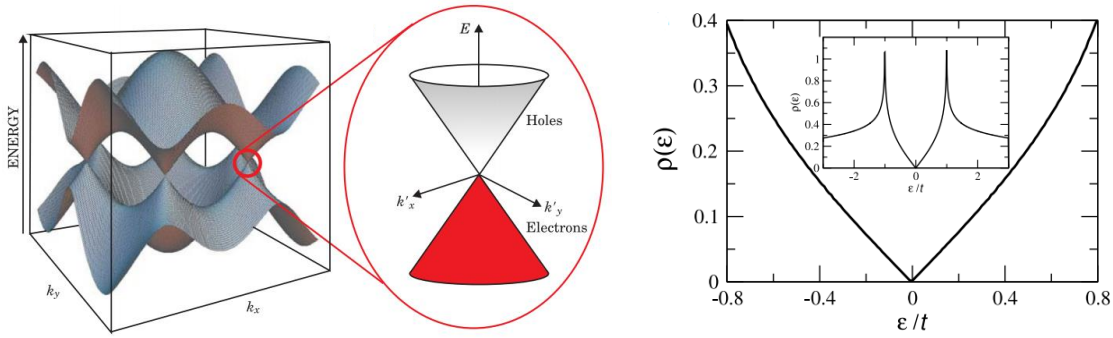

***Figure 2**:Graphene band structure and enlargement close to the K and K' points showing the Dirac cones (left). Density of states of graphene close to the Dirac point (right). The inset shows the density of states over the full electron bandwidth. (taken from ref* 24*).*

As mentioned earlier, graphene is a single layer of carbon atoms (2D material), but when several layers of graphene are stacked together to form graphite (3D material) the electronic properties change according to the number of layers: From a point of view of electronic structure graphene is a zero-gap semiconductor (or zero-overlap semimetal) but already when two layers are overlapped a semimetal behaviour emerges like in the case of graphite. It was shown that for three and more graphene layers the conduction and valence bands start overlapping with the overlapping increasing as the number of layers raises and from three graphene layers on, multilayer graphene systems are all semimetals and when more than 11 layers are stack together the difference in band overlap with graphite is smaller than 10%[25] therefore thicker structures should be considered, to all intents and purposes, as thin films of graphite.

1.1.2 Photoluminescence in Graphene derivatives

Single layer graphene is a zero-gap semiconductor, as described in the previous section so it is not expected to show any luminescence. Nevertheless, the introduction of defects allows the opening of a gap and fluorescence can be observed.

In graphene, carbon atoms are characterized by a sp2 hybridization with three σ bonds which give rise to the filled σ valence states and empty σ * conduction band states. The π states of the sp2 sites form weaker π bonds and they introduce π valence and π * conduction states which lie within the σ - σ * gap. The π and π * states form the band edges and therefore they control the optical gap[26,27] (**Figure 3**).

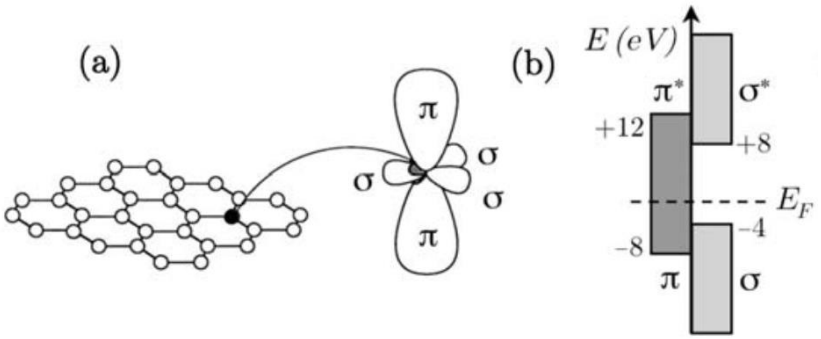

***Figure 3**:Illustration of the carbon valence orbitals (a) and energy (b) levels for the σ and π Bonds.(taken from ref* 27*).*

When graphene is oxidized, such as in the case of graphene oxide (GO) or reduced graphene oxide (rGO), the oxidation/reduction process causes the introduction of oxygen atoms on the carbon structure introducing carbon atoms hybridized sp3 (epoxy or hydroxyl groups) and carbon atoms bonded to carboxyl and carbonyl groups mainly at the edges. Sp3 carbon is characterized by four equivalent 2sp3 hybrid orbitals tetrahedrally oriented around the atom forming strong covalent σ bonds with the result of destabilizing the sp2 network and consequently causing the opening of a gap.[28,29] This induces the formation of sp2 clusters within a sp bonded matrix which act as luminescence centres where localized electron-hole (e-h) pairs can recombine and emit light; and since the bandgap depends on the size, shape, and fraction of the sp2 clusters, PL emission can be tuned by controlling the nature and dimension of these sites.[30,31]

1.1.3 Raman spectroscopy of Graphene

The peculiar structure of π electrons in graphene, characterized by a gapless electronic dispersion, implies resonances for any frequency, making Raman spectroscopy (see also Section 2.8) a powerful probe for the investigation of graphene-based carbon materials. The Raman spectrum of graphene based materials is characterized by several distinct bands[32,33] as shown in **Figure 4**, and depending on the number of graphene layers the Raman spectrum shows different features.

Single layer graphene in characterized by:

- The G peak which corresponds to the high-frequency E_{2g} phonon at Γ point of the brillouin zone, and is due to the relative motion of sp2 carbon atoms (**Figure 4**).
- The D peak is due to the breathing modes of six-atom rings (**Figure 4**), requires a defect for its activation[34] and it is dispersive with excitation energy.
- The D´ peak is due to the double resonance in an intravalley process, that is, connecting two points belonging to the same cone around k (or k´).
- The 2D peak is the d-peak overtone, and the 2D´ peak is the d´ overtone.

Multilayer graphene shows the aforementioned peaks as well the shear (C) modes, which is sensitive to interlayer coupling and the layer-breathing modes (LBMs), due to relative motions of the planes themselves, either perpendicular or parallel to their normal.

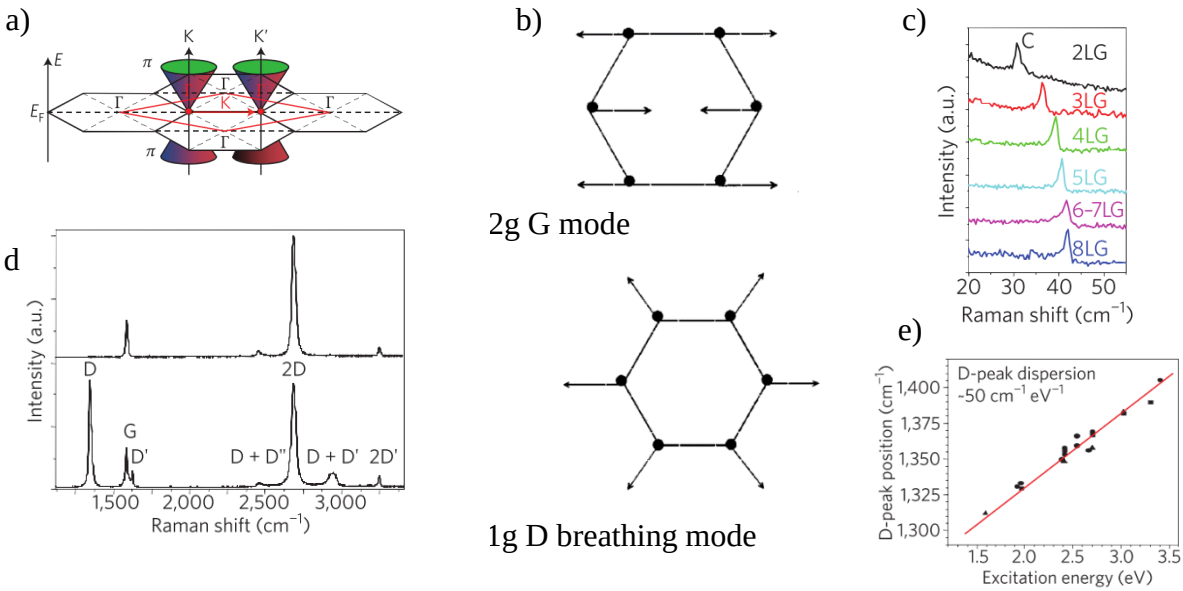

***Figure 4**:Electrons, phonons and Raman spectrum of graphene. (a) Electronic Brillouin zones of graphene (black hexagons), the first-phonon Brillouin zone (red rhombus) and schematic of electronic dispersion (Dirac cones). (b) atom displacements for two Raman mode E_{2g} G mode (upper) and A_{1g} D breathing mode. (c) C peak position as a function of the number of graphene layers (d) Raman spectra of pristine (top) and defected (bottom) graphene. (e) D-peak position as a function of excitation energy.(taken from ref* 35*).*

1.2 Carbon Nanotubes

1.2.1 Properties of Carbon nanotubes

Carbon nanotubes (CNTs) are one dimensional carbon materials which can be seen as a rolled up cylinder made up from a graphene sheet.[36] A tube made of a single graphitic layer cylinder is called single walled nanotube (SWCNT) while a tube made with several concentrically arranged cylinders is a multiwalled nanotube (MWCNT); only the first type will be considered in this thesis. These carbon tubes can reach lengths of centimetres, and each end is usually capped with half of a fullerene sphere.[37] The presence of the C-C graphitic bond provides SWCNT with excellent chemical and mechanical properties, while the presence of extended, delocalized π-electron systems makes these carbon materials very useful for charge transfer processes,[38] when combined, for example, with photoexcited electron donors.[39] Moreover, the electron-accepting ability of semiconducting SWCNTs offers an opportunity to facilitate electron transport and

increase the photo-conversion efficiency of nanostructure semiconductor based solar cells.[40]

Because the microscopic structure of carbon nanotubes is closely related to graphene, their extraordinary properties have their origin in the particular electronic structure of the graphene and CNTs are usually defined in terms of the graphene lattice vector (defined in **Figure 1** by the vectors a_1 and a_2). In carbon nanotubes, the graphene sheet is rolled up in such a way that a graphene lattice vector $C = n_1a_1 + n_2a_2$ becomes the circumference of the tube. This vector c, defined by two integers (n_1 and n_2), is called the chiral vector and it defines univocally a particular tube (**Figure 5**).

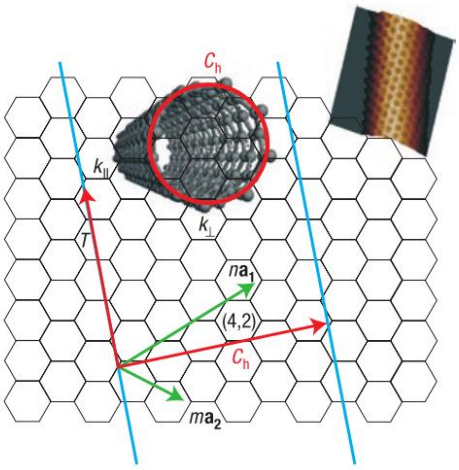

Figure 5*:The structure of graphene and carbon nanotubes. The carbon atoms in a single sheet of graphene are arranged in a honeycomb lattice.(taken from ref* 41*).*

Many properties of the nanotubes, like their electronic band structure, vary dramatically with the chiral vector even for tubes with similar dimeter and direction of the chiral vector[36]. The diameter of the tube is given by:

$$d_{CNT} = \frac{|c|}{\pi}$$

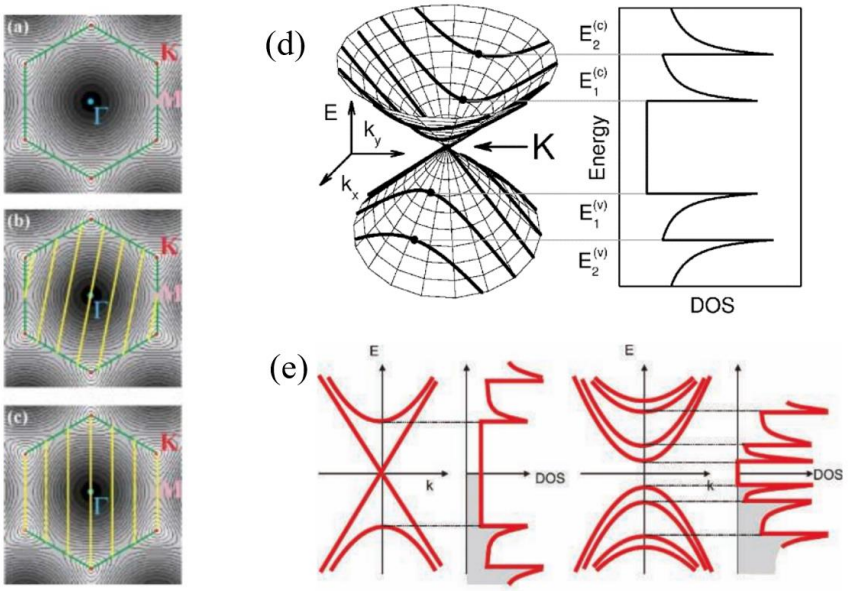

***Figure 6**:Band structures of: (a) graphene; (b) semiconducting single-wall carbon nanotubes (c) metallic single-wall carbon nanotubes. The yellow lines indicate the allowed wave vectors after roll-up of the graphene sheet. (d) The 1D density of states (DOS) for the conduction and valence bands corresponding to the E (k) dispersion relations for the subbands determined by the allowed wave vector along the tube circumference. (e) Schematic electronic energy-dispersion relations and densities of states of: a) metallic (left) and semiconducting (right) single-wall carbon nanotubes. (taken from ref* 42–44*).*

The electrical properties of CNTs can be studied starting from the honeycomb graphene structure (**Figure 5**). Whereas graphene is a zero-gap semiconductor, in the case of the tube the electrons are confined along the circumference, and while the wave vector *k* along the tube axis $k_{||}$ is continuous, as the tube is regarded as infinitely long, along the circumference periodic boundary conditions are imposed:

$$k_{\perp} \bullet\ c = 2\pi \mathrm{j}$$

Where *c* is again the chiral vector and *j* is an integer, so any wave vector $k_{\perp}$ is quantized and only certain set of the graphene *k* state are allowed.

As a result, each band of graphene is divided into a set of discrete energy sub-bands defined by *j* and the allowed energy states of a SWCNT are 1D sections of the graphene band structure (yellow lines in **Figure 6** b and c). The position of the allowed states is very important as they define the electronic properties of the tube: when the allowed states of a CNT pass through a Fermi point (K or K') the tube is metallic, while if no states pass through the Fermi point the tube is a semiconductor. Specifically, (n,n) nanotubes (armchair tubes) are always metallic, (n,m) nanotubes with n–m = 3j, where j = 1,2,3…, are nearly metallic: because of curvature effects, a tiny gap opens and when n–m ≠ 3j SWCNT are semiconductors. In the simple tight-binding model the bandgap of semiconducting nanotubes E_g is given by

$$E_g = \frac{4\hbar v_F}{3d_{CNT}}$$

where d_{CNT} is the tube's diameter and v_F the Fermi velocity.[45]

Figure 6 d shows the corresponding density of the energy states (right hand side): the density of states for graphene (**Figure 2**) is relatively dull except for the saddle point M, which gives rise to one spike on each band. On the other hand, in the case of carbon nanotubes (**Figure 6**), there are several minima of energy along the allowed sub bands and in correspondence of these points there are many states with similar energy and the density of states grows massively generating several spikes called van Hove singularities. Effectively, the HOMO and LUMO of semiconducting carbon nanotubes correspond to the first van Hove singularities in the valence and conduction bands, respectively, whereas the HOMO and LUMO of metallic nanotubes correspond to the Fermi level and have a zero HOMO-LUMO gap.[42]

The van Hove singularities are responsible for the characteristic absorption and photoluminescence spectra of carbon nanotubes which are different and unique for each carbon nanotube described by the chiral numbers (n,m). As illustrated in **Figure 7**a light is absorbed between the van Hove singularities of the valence and conduction band giving rise to E_{ii} abs transitions ($v_i \rightarrow c_i$) while in the case of photoluminescence, after the light induced excitation, electrons first relax to the lowest conduction van Hove singularity and finally relax to the highest valence van Hove singularity emitting light (E_{11}). In the case

of metallic tubes there is no energy gap so while absorbance peaks are present no photoluminescence can be observed.

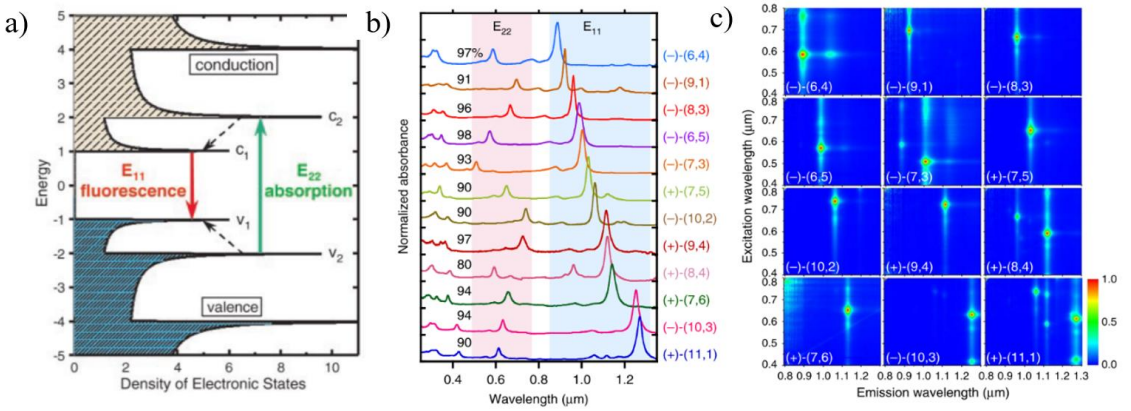

***Figure 7**:a) Schematic density of electronic states for a single nanotube structure. Solid arrows depict the optical excitation and emission transitions of interest; dashed arrows de- note nonradiative relaxation of the electron (in the conduction band) and hole (in the valence band) before emission (taken from ref* 46*). (b) Optical absorption spectra (the percentages refer to the sample purity) and (c) photoluminescence contour maps of the 12 sorted (n,m) semiconducting SWCNTs.(taken from ref* 47*).*

1.2.2 Carbon Nanotubes Fabrication Methods

Carbon nanotubes are produced with different techniques such as laser ablation,[48] where a high power laser is used to vaporize carbon target at high temperature under continuum flux of an inert gas and carbon nanotubes grow on the colder surface of the reactor as the vaporized carbon condenses. Both SWCNT and MWCNT can be synthetized with this technique and the quantity and quality of the tubes depends on the amount and type of catalyst, laser power as well as temperature, pressure and inert gas. Chemical vapor deposition[49] is another method involving the growth of CNT from a metal catalyst through the deposition of a carbon gaseous source. Carbon nanotubes can also be prepared through Arc-discharge[50] which involves applying a voltage between two graphitic electrodes in the presence of a metallic catalyst allowing the growth of the tubes. While these are all valid methods for the production of SWCNTs, it has so far proven to be challenging to control the chirality of the nanotubes; moreover, a solution-based approach is desirable

for the scalable and low-cost assembly and fabrication of CNT-based optoelectronic systems and devices.

1.2.3 Carbon Nanotubes Solubilization

A common problem related to carbon nanotubes, and in general carbon nanomaterials, is their poor solubility even in organic solvents which results in big issues in terms of their assembly and processability. In this regard, several methods have been developed to overcome this limitation comprising both chemical covalent functionalization strategies and non-covalent approaches. One of the first approaches developed was the oxidation of the tubes with acid treatment[51,52] which implies the braking down of the tubes into shorter segments and the introduction of oxygen containing groups as defects. These defects increase the tubes solubility but at the same time compromise the carbon structure affecting the tubes electrical and mechanical properties.

Other strategies involve the functionalization of acid treated tubes with other molecules both in covalent[53] or non-covalent manner[54] but still the acid treatment represent a serious drawback for the integrity of the carbon structure and the tube properties. For this reason non-covalent functionalization methods[55,56] have emerged as alternative methods for the CNT solubilization allowing to maintain the integrity of the carbon structure and hence retaining the tubes properties. These strategies involve the use of surfactant to improve the CNT solubility including polymer,[57] organic compounds,[58] cellulose,[59] polyaromatic compounds.[60]

Among all these dispersing agents DNA has emerged as one of the best molecules to solubilize CNTs as described by Zheng et al[61] who were the first to use single strand DNA (ssDNA) as a dispersing agent to solubilize SWCNT in water. The interaction between CNT and DNA is characterized by a helical wrapping of the DNA along the tube (**Figure 8**) where π-π staking interactions of the DNA bases of the nucleotides with the side of the tubes allows a stable complex formation while the phosphate groups arrange themselves externally providing a polar, water friendly environment allowing the tube solubilization.

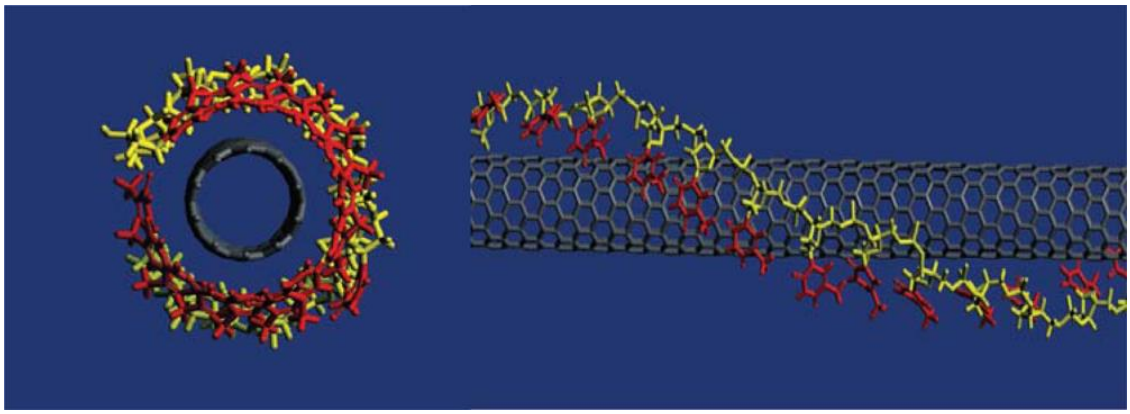

Figure 8*:Illustration of a SWNT wrapped by ss-DNA. Aromatic nucleotide bases in the ss-DNA are exposed to form π-stacking with the sidewall of the SWNT.(taken from ref* 61*).*

1.2.4 Carbon Nanotubes Separation

Regardless of the preparation method used for the synthesis of single walled carbon nanotubes, many major challenges in SWCNT based research arise from the diversity of tube diameter, length and chiralities present in all samples. Since the optical and electronic properties of the nanotubes deeply depend on the structure[46] these samples show characteristics which are a combination of all the different chiral tubes present in that sample.

Different approaches have been developed in order to sort CNTs by both length and chirality, including size exclusion chromatography,[62] centrifugation,[63] gel separation.[64,65] All these methods are generally based on specific interactions of polymers or supernatants with the tubes sidewalls.

In this regards DNA has been shown to be a powerful dispersing agent for separating tubes in term of length through size exclusion chromatography (SEC)[66] but also by chirality. The DNA-SWCNT interaction and the resulting hybrid structure are dependent on both DNA sequence and SWCNT structure, thus it has been found that specific DNA sequences can be selective for specific SWCNT structure recognition allowing chirality separation. Zheng et al[67] investigated a wide library of DNA sequences and were able to separate a synthetic mixture of tubes into individual single chirality components (**Figure 9**).

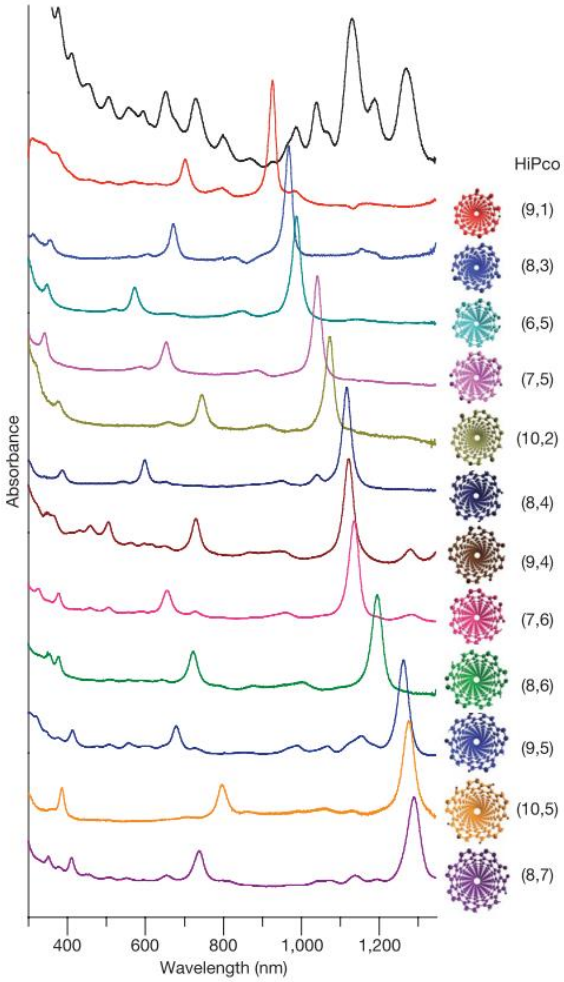

***Figure 9**:Ultraviolet–visible–near-infrared absorption spectra of 12 purified semiconducting SWNTs and the starting HiPco mixture. The structure of each purified SWNT species (viewed along the tube axis) and its (n,m) notation are given at the right side of the corresponding spectrum.(taken from ref* 67*).*

More recently Zheng's research group were able to separate left and right-handed chiral tubes each of which is characterized by an ordered DNA structure that binds to a nanotube of defined handedness and helicity.[68]

1.3 Carbon Materials Functionalization

A critical point in all synthetic approaches of carbon-based hybrids as well as composites is the type of nanocarbon involved and the degree of its functionalization. A common

strategy to overcome these problems is the oxidation of carbon materials through sonication,[69] acid treatment[70,71] or ozone exposure.[72]

***Figure 10**:Oxidizing strategies for the introduction of oxygen containing groups for further functionalization of carbon nanostructures. (taken from ref 16).*

All of these techniques allow the formation of defects on the carbon structure as oxygen containing functional groups, which increase the material solubility and at the same time provide anchoring groups for the subsequent attachment of other components. On the other hand, oxidation processes cause several drawbacks, including the unspecific functionalization, with defects that can be localized everywhere on the active surface and potential damage of the nanocarbon π -network thus compromising its mechanical, thermal and electronic properties.[73]

Oxygen containing groups, such as carboxylic acid functionalities of oxidized CNTs and GO are potential binding sites for a range of covalent interactions and this strategy has been used to successfully link, for example, nanoparticles(NPs),[74] quantum dots,[75] polymers,[76] proteins,[77] porphyrins[78] and biomolecules[79] to oxidized CNTs and GO. Non-covalent functionalization is based on weak interactions between the different components, such as van der Waals, electrostatic or π–π interactions. This kind of functionalization provides a way to maintain the original properties of the carbon nanomaterials through a non-destructive route but on the other hand it is characterized by weaker bonding forces.

A common procedure is the use of surfactants and polymers to facilitate CNTs[57] and graphene solubilization,[80] as previously described in Section 1.2.3, taking advantage of the π–π staking interactions between delocalized π electrons of the carbon structure and those of aromatic moieties of organic compounds, such as pyrene,[81] perylene,[82,83] and DNA.[61] These molecules can be potentially further modified with specific functional

groups such as amine, acid, thiol or charged chemical groups which can then be used for the further tethering of a second component.[84]

1.4 Quantum dots

1.4.1 Quantum Dots Properties

Quantum dots are nanometer-scale semiconductor crystallites.[85] Because of their nanoscale dimensions the electron and hole wave functions experience three-dimensional quantum confinement due to the dot boundaries resulting in strong changes in the optical properties of the material.[86] The change in size, especially for semiconductor materials, evolving from atoms or small molecules to bulk phase, results in modifications of fundamental properties: for example the band gap of CdS can be tuned between 4.5 and 2.5 eV as the size is varied from molecular regime to the bulk material, the radiative lifetime for the lowest allowed optical excitation ranges from picoseconds to several nanoseconds, the melting temperature increases from 400˚C to 1600 ˚C;[85] Notably this remarkable change in electronic, optical and physical properties takes place in a material with the same chemical composition, purely by increasing the size, and can be used for the development of optical and electrical devices.[87]

The most striking property of semiconductor quantum dots is the incredible change in optical properties as a function of size: the band gap can be modulated by selecting the particle size therefore the possibility of tuning their optical absorption in the UV and near infrared spectrum.[88] From a chemist's point of view, QDs can be seen as big molecules with atoms organize in a bulk crystal structure, on the other hand from a physicist's perspective, a nanocrystal (NC) can be thought of as a three-dimensional potential box that confines the motion of electrons and holes, which would be free in the corresponding balk material. This results in a discrete, size-dependent, energy-level pattern and thus NCs exhibit structured spectra arising from discrete optical excitations.[89] **Figure 11** shows the changes in the density of electronic states when we move from a bulk material, characterized by electronic bands, to 2D materials, like shown for CNTs in section 1.2.1, characterized by spikes or singularities, to 0D structure, characterized by discrete energy levels.

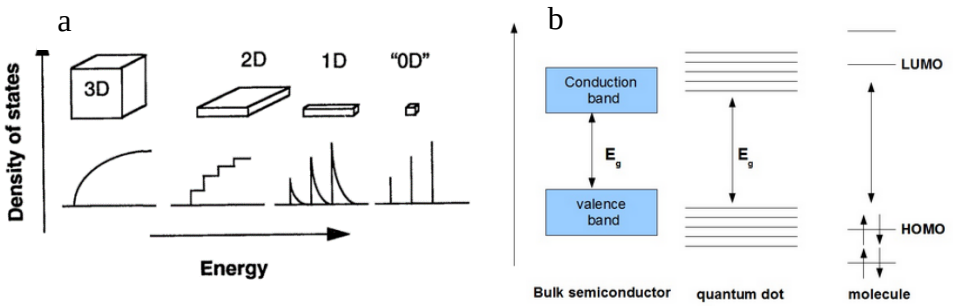

***Figure 11**:Density of states in one band of a semiconductor as a function of dimension (a) and schematic illustration of the density of states in semiconductor clusters (b).(taken from ref* 85*).*

The change in optical properties of quantum dots was described by Ekimov[90] and Efros[90] and in both cases it was found that the colour of the nanocrystals is correlated to the their size. The absorption and photo-luminescence properties is a consequence of the quantum sized effects, which affect the energy levels in three dimensionally confined particles. The simplest model to predict and calculate the energy of the electron and hole quantum-size levels is to approximate the quantum dot to a sphere surrounded by an infinite potential barrier.[91] The resulting values for the energy levels are:

$$E_n = \frac{\hbar^2 \pi^2 n^2}{2mR^2}$$

Where *m* is the effective mass, *R* is the sphere radius. The energy of the levels increases with decreasing nanocrystal size and hence increases the total energy of the band edge optical transitions. By changing the nanocrystal size it is possible to change the energy gap of the material passing through almost the whole optical spectrum.[92]

In this simplified model the Coulomb interaction between the optically created electron and hole has been ignored but it strongly affects the nanocrystal optical spectra. This interaction must always be taken into account because both particles are confined in the same crystal volume. The Coulomb energy of the electron and hole interaction is of the order of $e^2/\varepsilon R$, where ε is the dielectric constant of the semiconductor. Because the quantization energy increases with decreasing size as $1/R^2$, the Coulomb energy, which

grows only as 1/*R*, becomes a small correction to the quantization energies of electrons and holes in small crystals and reduces transition energies by only a relatively small amount. On the other hand, in large nanocrystals, the Coulomb interaction is more important than the quantization energies of the electrons and holes.[93] The optical properties of nanocrystals strongly depend on the ratio of the nanocrystal radius, R, to the Bohr radius of the bulk exciton, $R_B = \hbar^2\varepsilon/\mu e^2$, where μ is the exciton reduced mass.[93] In a weak regime $R \gg R_B$, the binding energy of an exciton is larger than the quantization energy of both the electrons and holes, and the optical spectra of these nanocrystals are determined by the quantum confinement of the exciton centre of mass. In a strong regime, like the case of small nanocrystals, where $R \ll R_B$ the optical spectra can be considered as spectra of transitions between electron and hole quantum-size levels since the electron-hole Coulomb interaction lowers the energy of these transitions only slightly.

Size dependent absorption spectra are shown in **Figure 12** together with the photoluminescence (PL) for a range of QDs with different diameters. PL peaks are slightly red-shifted from the absorption peak and thus corresponds closely to the NC bandgap. As a result, there is a size dependence not only on the absorption band edge but also on the PL frequencies, both tuneable over a broad range of wavelengths simply by changing the NC size.

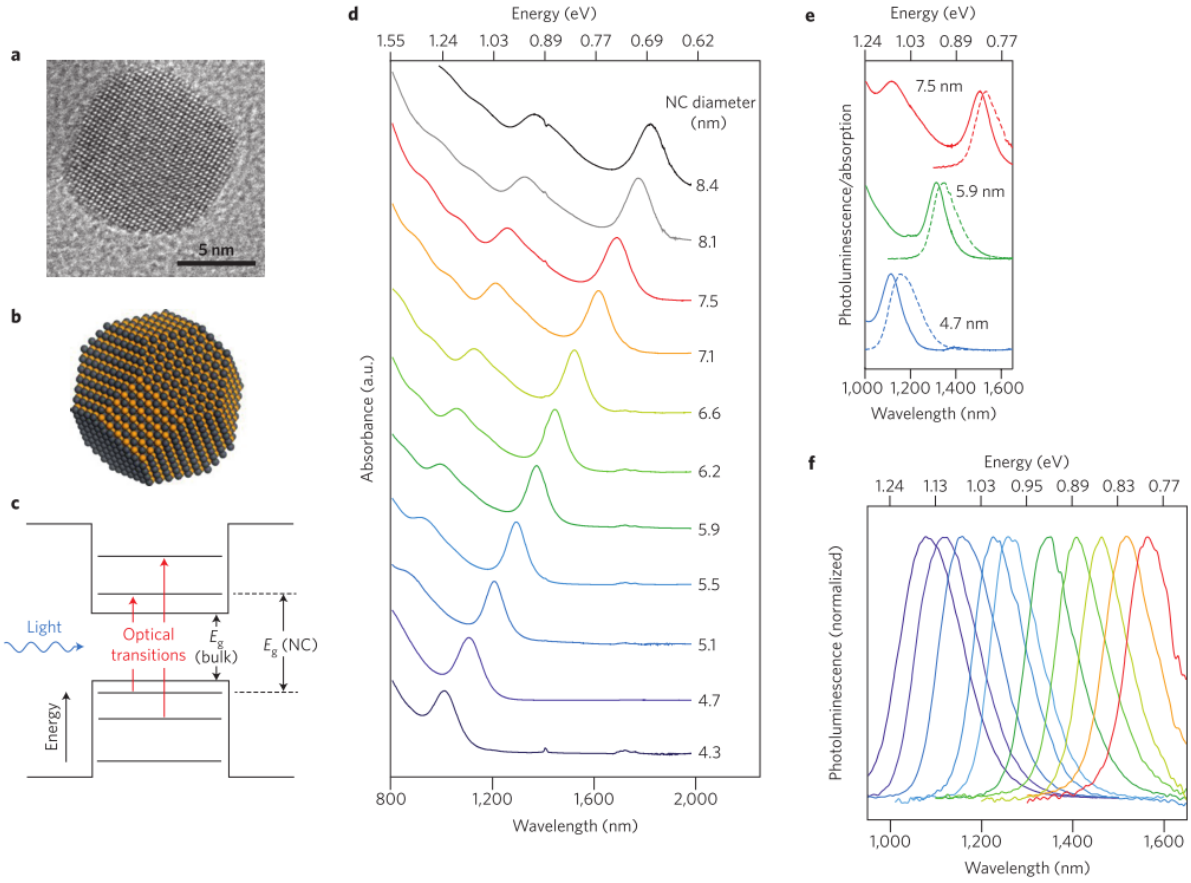

***Figure 12**:a, Transmission electron micrograph of an PbS NC. b, Three-dimensional atomic structure of a PbS NC, where Pb (S) atoms are shown as gold (black) balls. c, Schematic energy-level structure of electrons and holes confined in a spherical NC. d, the absorption spectra measured in PbS NCs with diameters varying from 4.3 to 8.4 nm. e, Comparison of absorption (solid lines) and PL (dashed lines) spectra in PbS NCs with average diameters of 4.7, 5.9 and 7.5 nm. f, The PL spectra measured in PbS NCs with diameters varying from 4.3 to 8.4 nm. Colours are the same as those in d.(taken from ref* 89*).*

As regards the materials involved in the QD synthesis, a wide range of semiconductor nanocrystals has been employed including III-V compounds (GaAs, GaP, InP), II-VI compounds (CdSe, CdS, ZnSe, CdTe, PbS) and I-VII compounds (CuCl, CuBr, AgBr). In this thesis, only core CdTe QDs were employed.

1.4.2 Core/Shell Quantum Dots

Monodispersed semiconductive nanocrystals are usually grown starting from metal organic precursors which are rapidly injected into a vigorously stirred flask containing a hot (~150-350 ˚C) coordinating solvent. Stabilizing agents must be present during the growth to prevent aggregation and precipitation of the NCs. These capping agents form a monolayer all around the surface regulating the growth in solution and passivating surface electronic states.[94]

A significant fraction of these organically passivated core NCs typically exhibit surface-related trap states as a result of the interaction between the surface atoms and the stabilizing ligands. These trap states act as fast non-radiative de-excitation channels for photogenerated charge carriers, thereby reducing the fluorescence quantum yield (QY). An important strategy to improve NCs' surface passivation is their overgrowth with a shell of a second semiconductor, resulting in core/shell (CS) systems.[95] In this thesis CdSe/ZnS core shell QDs were employed.

1.4.3 Single Crystal Photoluminescence (blinking)

Almost all colloidal nanocrystals, under illumination, exhibit an intermittency in their emission called PL blinking. Such Photoluminescence blinking is a random switching between states of high (ON) and low or no (OFF) emissivities. The photophysics of blinking could only be observed at the single NC level, as first noted by Nirmal et al.,[96] and it would be readily smoothed out and therefore undetectable in any finite ensemble.

Figure 13 shows typical PL intensity traces for single NC which exhibit a sequence of bright and dark periods in time. The interchange and the duration of ON and OFF periods depend on several factors including the material of which the NCs are made of and the structure, either if it is core or core/shell QDs and in general the duration of the ON periods is much longer than that for bare particles, which have a very low quantum efficiency and are 'dark' most of the time.[89,97]

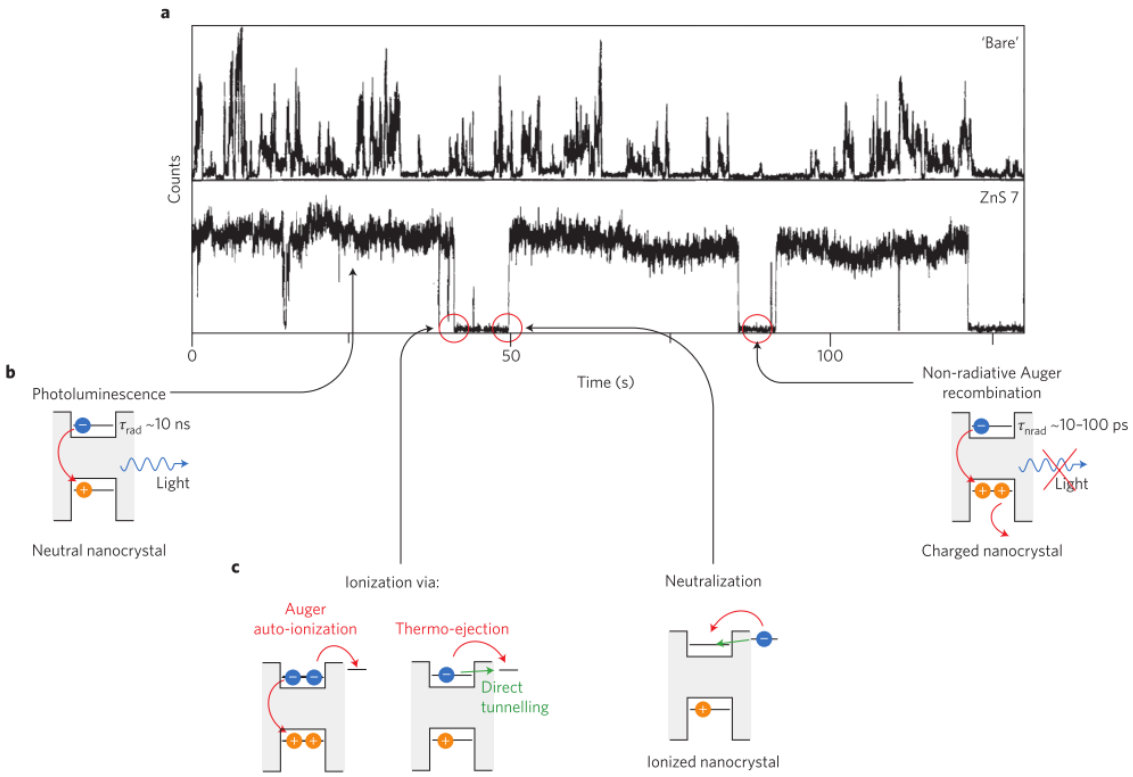

***Figure 13**:a, The time dependence of the PL intensity of a single CdSe NC under a continuous-wave excitation. The upper and lower panels show dependences measured in 'bare' NCs and NCs coated with a seven-monolayer-thick ZnS shell, correspondingly. b, Schematics of neutral and charged NCs. c, Processes leading to NC ionization and neutralization.(taken from ref* 89*).*

The most widely accepted model to explain the PL blinking is that the ON and OFF events arise due to illumination -induced charging (ON → OFF) followed by re-neutralization (OFF → ON) of the NCs. The interaction with the light shined on the uncharged NC, generates an electron–hole pair (exciton), which then recombines, emitting a photon and giving rise to the PL process known as radiative recombination (on period). The charge separation in a neutral NC, gives rise to an electric field which can trigger a process known as non-radiative Auger recombination, by which the additional exciton energy is efficiently transferred to the extra electron or hole. This can result in the ejection of charges from the core of the NC leaving it in a charged 'dark' state (OFF period). To complete the blinking cycle, this ejected charge needs to return at some later time to the NC, thereby achieving charge neutrality, blocking non-radiative Auger relaxation pathways, and therefore restoring the original high quantum yield (ON) for radiative

recombination of the exciton. How exactly this re-neutralization process occurs is not entirely clear and remains an active area of research.[89]

Another aspect which is not entirely elucidated is the mechanism through which the NC under illumination gains a net separation of charges. Different models have been proposed including thermal activation, or resonant ionization. The latter states that ionization occurs via resonant quantum-mechanical tunnelling of a photogenerated electron (or hole) through the NC to become localized in trap states on the surface of the NC or the surrounding substrate.[98] The efficiency of such ionization process will depend in general on the NC size, NC temperature, and band offset between the semiconductor NC and the surrounding matrix, as well as the laser excitation intensity. Furthermore, the position of this localized charge trapping states depends and can be controlled by the chemical nature of the passivating ligand and the surrounding environment.

1.5 Synthesis/assembly of nanocarbon-nanocrystal Heterostructures

Both carbon nanomaterials and semiconductor nanocrystals have been widely studied and a number of devices have been developed. A further step towards better and more efficient devices would be to combine these two materials into functional heterostructures either to merge and improve the properties of the single components and/or to take advantage of the possible phenomena that can be generated at the interface. Heterostructures can be synthesized in two different ways: 1) by dispersion in a matrix of the second material to form a nanocomposite or 2) through the close interaction between the two components to form a hybrid (**Figure 14**).

A distinction between nanocomposites and hybrids has been provided in a review by Eder.[17,16] Nanocomposites are materials that incorporate nanosized particles into a matrix in order to generate a single multiphase material resulting in a combination of the properties of the single components. The materials are usually synthetized separately and then combined so that one phase is dispersed into a second one. This procedure ultimately results in a heterogenous distribution of the filler and consequently in nonuniform properties. The objective of nanocomposites materials is to fuse the individual properties of the single components so that the resulting material would benefit of the peculiar

characteristic of each constituent. For example, combining a metallic component with a hard one could potentially generate and robust conductive material.

On the other hand nanohybrids are synthetized when a second component is in direct contact with the main support material, it plays an active rule in the resulting material increasing the number of applications compared to the composite: hybrid materials merge the properties of the components in a way that creates new properties distinct from those of either building blocks.[16] The key aspect in nanohybrids is the role of the interface between the two compounds: The nature of the interface is defined through size domain effects where similar size to volume ratio between the single components grants a close proximity and interconnection which give rise to a change of the properties at the interface which is the result of the combination of the two moieties.

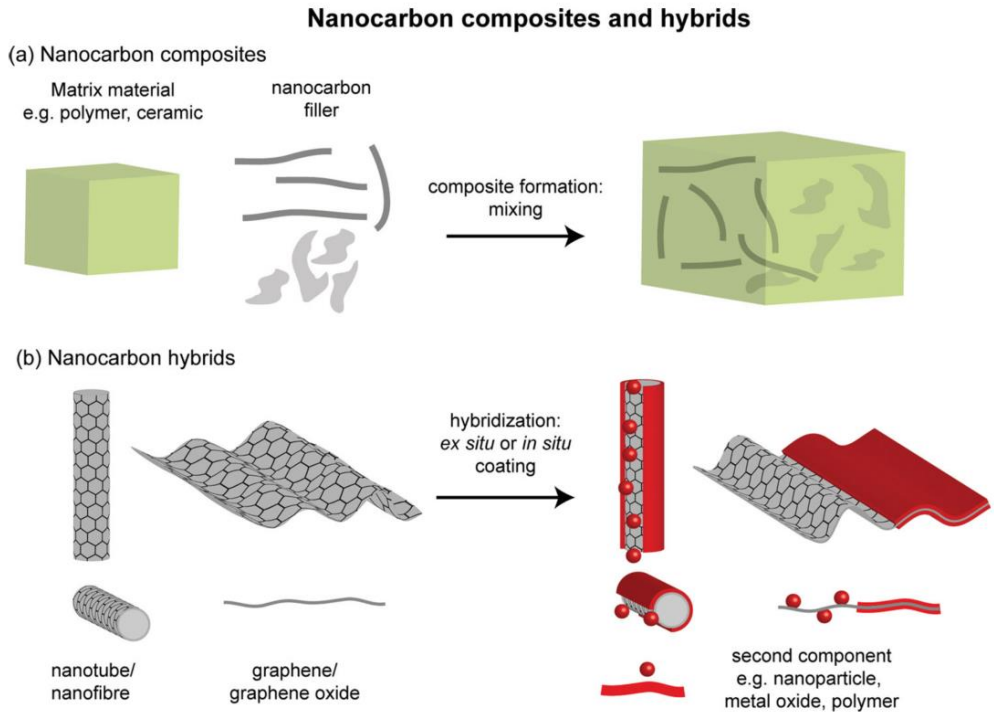

***Figure 14**:(a)Schematic of nanocarbon composites and hybrids showing difference between nanocarbon composites and (b) nanocarbon hybrids prepared by the coating of a second component onto the surface of the nanocarbon (and vice versa).(taken from ref 16).*

The synthetic strategies for the formation of nanocarbon-hybrids can be divided into ex situ and in situ approaches (**Figure 15**).[17] In the ex-situ strategies, the two components

are prepared separately and designed with specific properties in terms of morphology and dimensions and in a second instance, they are combined together to be chemical bonded through the chemical functional groups present on the respective surfaces. The nature of the chemical bonds between the components can be both[99] covalent as well as non-covalent or electrostatic interactions[39]. On the other hand, the in-situ approach involves the use of molecular precursors: one component is synthetized in the presence of the other, with the latter affecting the growth and hence the properties of the former. Another possibility is that both components are produced simultaneously, in this way the properties of the single component will influence the synthesis of the other in terms of morphology and structure.[100,101] This strategy allows the anchoring of inorganic compounds on the carbon nanostructures with possibility to attach nanoparticles,[102] nanowires[103,104] or deposit thin films.[105]

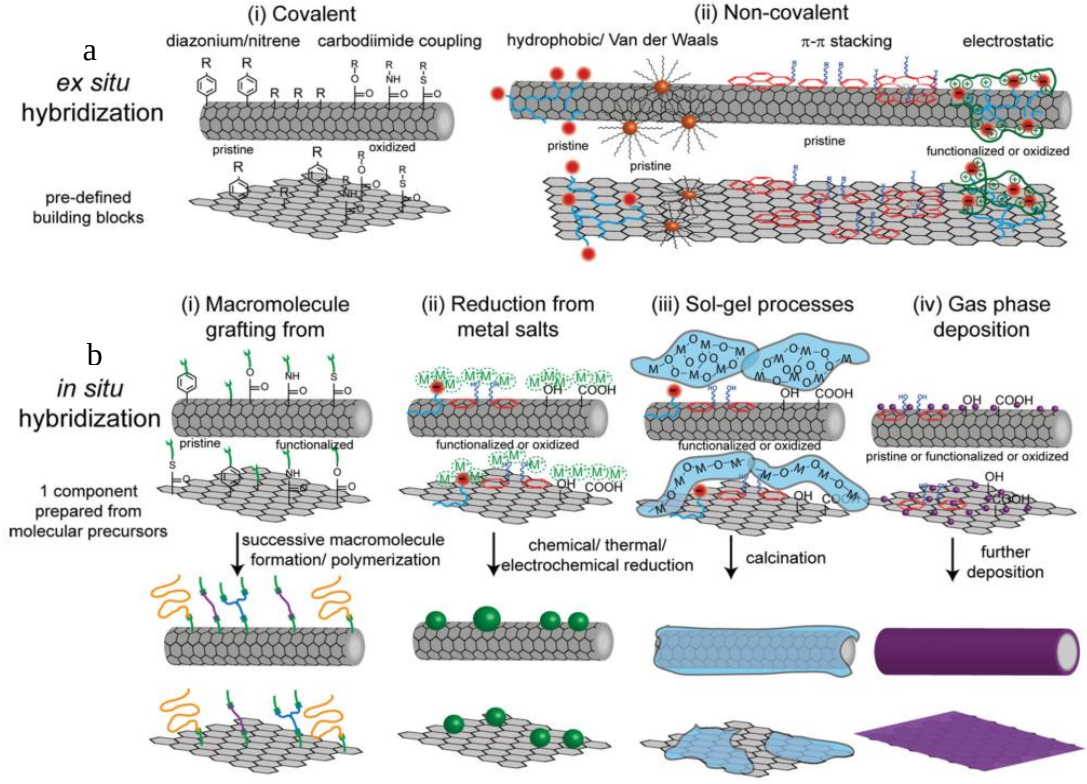

***Figure 15**:Ex situ (a) and in situ (b) synthetic strategies of nanocarbon hybrids. from predefined building blocks can be completed via a range of (i) covalent and (ii) non-covalent techniques. Ex situ synthesis of nanocarbon hybrids from predefined building block can be completed via covalent (i) and non-covalent (ii) techniques. In situ synthesis of the hybrid component in presence of the nanocarbon can be achieved following various strategies including: (i) grafting from for polymers and macromolecules, (ii) chemical*

reduction for metallic or semiconducting nanoparticles, (iii) sol-gel processes for semiconducting thin films or nanoparticles and (iv) gas phase deposition for thin metallic or semiconducting films.(taken from ref 16).

In this case the functionalization of the nanocarbon is not a specific requirement, differently from the ex-situ approach where the introduction of defects is a necessary step to anchor the second component. Nevertheless, the presence of functional groups can potentially provide a reaction centre for the growing of the second component, facilitating the initial stages of the hybrid formation.

Both these two strategies show advantages: the ex-situ approach is relatively simple considering that already prepared nanoparticles can be employed, already tailored with the desired characteristics and consequently with a higher control over morphology, structure, shape, and size; on the other hand, the in-situ strategy requires in general less nanocarbon modification which could be detrimental for the intrinsic properties of the carbon nanostructure. Therefore, the choice of hybridization technique depends on a compromise based on the choice of nanocarbon, the functional groups, the functionalization method, hence the resulting physical properties in order to find the best systems for the chosen application.[16]

According to Eder[17] hybrid materials can be further classified into Class I and II materials. This distinction is based on the strength of the interaction between the two components, which also affects the hybrids' properties.

• In Class I materials the two phases are connected through weak interactions, such as van der Waals, hydrogen bonding, or electrostatic interactions. Examples are materials based on organic and inorganic materials that form a network where the two components interpenetrate each other without strong chemical bonds.

• Class II hybrids are formed via strong chemical interactions between the components, for example, when the discrete building blocks are covalently connected to each other by capping or linking agents.

1.6 Electronic coupling in Carbon nanostructures-QD hybrids

One of the key requirements for an actual device implementation of QD-carbon based hybrid materials is the electronic coupling between the two components. The QD-carbon based hybrids can be regarded as a donor-acceptor system where the interaction between the light and the QDs causes a charge separation in the semiconductor nanoparticles (eq. a). Possible pathways for the deactivation of excited QDs are the emission of a radiation (eq. b), an electron transfer to the SWCNTs (eq. c) or an energy transfer process (eq d):

a) QD + hν → QD (h + e)

b) QD (h + e) → QD+ hν′

c) QD (h) + SWCNT → QD + SWCNT (e)

d) QD*+ SWCNT → QD + SWCNT*

In the process of energy transfer from an excited donor to an acceptor (also known as fluorescence resonance energy transfer, FRET),[106] a donor fluorophore absorbs the energy due to the excitation of incident light and transfer the excitation energy to a nearby chromophore, the acceptor.

$$D + h\upsilon \rightarrow D^*$$

$$D^* + A \rightarrow D + A^*$$

$$A^* \rightarrow A + h\upsilon'$$

Energy transfer is characterized by quenching of the donor fluorescence and a reduction of excited state lifetime accompanied also by an increase in acceptor fluorescence intensity. Forster obtained a FRET rate which is inversely proportional to the sixth order of magnitude of distance (*R*), assuming a dipole moment approximation where the fluorophore size is smaller than the separation between donor and acceptor.

$$k = \frac{1}{\tau_0}\left(\frac{R_0}{R}\right)^6$$

Where τ_0 is the lifetime of the donor in absence of the acceptor and R_0 is the Forster radius (the distance at which half of the excitation energy of donor is transferred to the acceptor chromophore). When the donor or the acceptor or both involve systems with extended electronic densities in one, two, or three dimensions, the point dipole approximation does not hold and one obtains other distance dependences depending on the dimensionality of the donor and/or the acceptor.[107]

On the other hand, a charge transfer (CT) event involves the absorption of light by the donor with a subsequent charge injection into the acceptor obtaining a charge separated state. In the case of electron transfer the CT process can be summarized by the following reactions, in the case of donor-acceptor electron injection:

$$D + h\upsilon \rightarrow D^*$$

$$D^* + A \rightarrow D^+ + A^-$$

The rate of CT between donor and acceptor can be estimated based on the free energy change of the reaction, the reorganization energy, and the electronic coupling strength. Importantly, the electronic coupling strength decays exponentially with distance. Therefore, the rate of charge transfer is expected to decrease much more rapidly with distance than that of energy transfer and can be expressed, according to Marcus theory,[108] as

$$k_{ET} = k_0 e^{-\beta r}$$

where k_0 is the rate at the contact distance for the donor and acceptor, r is the separation between donor and acceptor or the length of the bridge, and β is a structure-dependent attenuation factor, which correlates the rate of electron transfer with the chemical structure of the bridge.

Energy and charge transfer are both mechanisms involved in the electronic coupling in QD-carbon based nanohybrids and the occurrence of one process over the other is strongly dependent on the nature of the interface between the two components. The competition between these two processes are highly dependent on the system involved and in particular on the physical separation between donor and acceptor as well as spectral overlap and energy level alignment of the two components.

2 EXPERIMENTAL TECHNIQUES

2.1 Atomic Force Microscopy (AFM)

Atomic Force Microscopy (AFM) was developed in 1986 by Binnig et al.[109] as a way to investigate surfaces of insulators on an atomic scale. This technique is based on the principle that when a tip, attached to the end of a cantilever, scans a surface, "atomic" forces interact between the tip and the surface so that the cantilever is deflected up and down according to the contours of the surface itself. A position sensitive photo detector receives a laser beam reflected by a mirror on top of the cantilever and provide a deflection feedback, therefore by monitoring the deflections of the cantilever, the topographic features of the surface can be mapped out (**Figure 16** b).

The overall interactions between the tip and the surface can be represented with a Lennard-Jones potential of the form:

$$V(r) = \varepsilon \left[\left(\frac{\sigma}{r}\right)^{12} - \left(\frac{\sigma}{r}\right)^{6} \right]$$

Where ε is the depth of the potential well, σ is the distance at $V(r) = 0$ and r is the distance between the tip and the surface. The r^{-12} term is the repulsion term that describes the Pauli repulsion at short range of the electronic clouds distances (van der Waals) and the r^{-6} term is the attractive term, describing attractions at long range (induced dipole, dipole-dipole and permanent-induced dipole interactions).

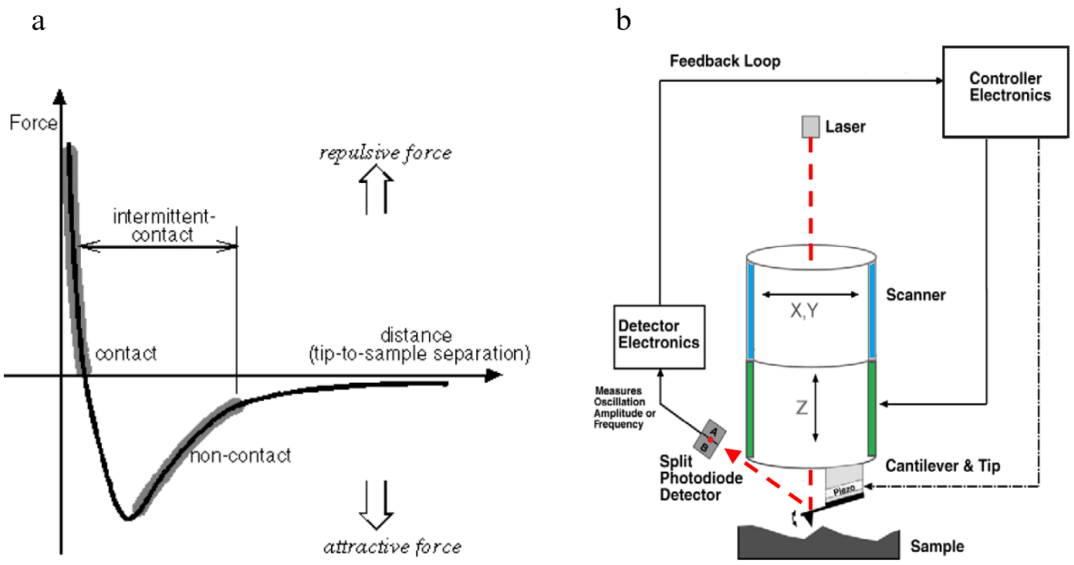

***Figure 16**:(a) Tip-force curve and (b) schematic of atomic force microscope Image from Bruker.*

The force is represented in **Figure 16**, where two regimes are highlighted: i) the contact regime, ii) the non-contact regime. In the contact regime the interatomic force between the cantilever and the surface are predominantly repulsive while in the non-contact regime the attractive force prevails. Typically, three different AFM modes exist: contact, non-contact and tapping mode:

- In contact mode the tip is in direct contact with the surface, a feedback loop maintains a constant deflection between the cantilever and the sample by moving vertically the scanner for each point in the x,y plane and by keeping a constant cantilever deflection, the force between the tip and the sample remains constant. The force is calculated from the hooke's law $f = -kx$, where k is the spring constant of the cantilever and x is the cantilever deflection: the scanner moves vertically at each x,y point and the distance is stored and elaborated by the computer to form the topographical image.

- In non-contact mode the tip does not contact the sample surface, but oscillates at a frequency which is slightly above the cantilever's resonance frequency. The decrease in resonant frequency caused by the forces between the tip and the surface, affects the amplitude of the oscillation, a feedback system maintains the amplitude constant by moving the scanner and generating the sample topography.

- Tapping mode is a combination of both contact and non-contact mode, where the cantilever oscillates below or at its resonance frequency while the tip is scanning the surface. **Figure 17** shows the force vs time diagram for a tapping mode: in point a the tip is far from the surface and no forces affect the tip, as the tip approaches the surface the cantilever is deflected towards the surface (point b), the tip then stays on the surface and the force increases until the z position of the modulation reaches its bottom position at point c, the probe then starts to withdraw and the force decreases until it reaches a minimum (d).once the tip is far enough from the surface only weak long-range forces are involved, up to the maximum tip-sample separation point (e) where again no forces are involved. While the tip is contacting the surface at the bottom of its swing (point c) a feedback loop maintains a constant oscillation amplitude. When the tip passes over an asperity in the surface, its vibration amplitude decreases due to availability of less vibrating space. On the other hand, when it passes over a depression, its vibration amplitude increases. This change in oscillation amplitude is detected by the optical system and fed back to the controller which gives back the topographical image. With this technique lower forces are applied on the sample and there are less damages especially on soft samples.

AFM measurements were carried out on a Bruker Dimension Icon system. Silicon nitride ScanAsyst probes with a spring constant of 0.4 N/m from Bruker were employed. Typically, images were scanned at 1-2 Hz/line with a setpoint of 0.02 V.

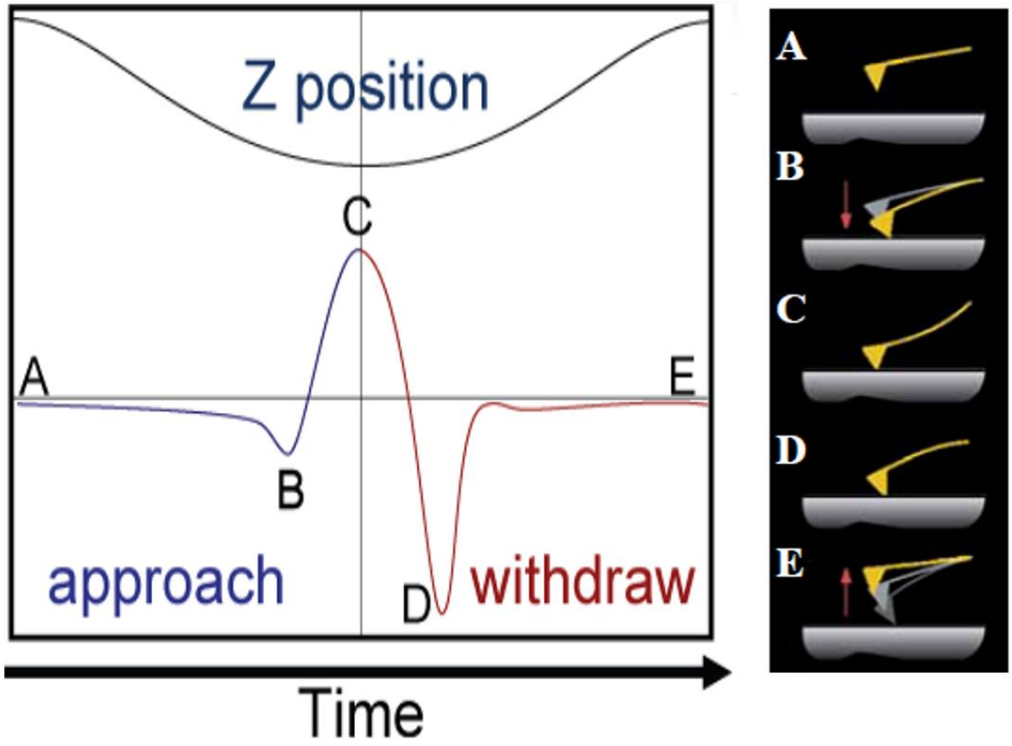

***Figure 17**:Force diagram of AFM tip deflections in tapping mode. Image from Bruker.*

Samples were imaged under ambient conditions with a Bruker Dimension Icon microscope, with a NanoScope IV control unit. Tapping mode AFM imaging was performed with SCANASYSTAIR tips (Bruker, spring constant 0.4 N/m). Images were analyzed with NanoScope Analysis (version 1.5, Bruker) software.

2.2 Ultraviolet-Visible spectroscopy (UV-vis)

UV-Vis spectroscopy was carried out on a Perkin Elmer Lambda 35 spectrometer.

2.3 Fourier Transform Infrared Spectroscopy (FTIR)

FTIR spectra were collected with a Perkin Elmer Spectrum 65 FT-IR spectrometer. Spectra were acquired from liquid samples using water as background.

2.4 Photoluminescence Techniques

Photoluminescence (PL) is the emission of light from a substance after that a certain amount of light has been absorbed. Samples are generally excited using a laser which promotes electrons to higher energy levels. Excited states can relax via both radiation-less processes or also through radiative ones giving rise to emitted light which can be collected and measured.

PL measurements are generally classified into stationary (or steady states) measurements and time resolved measurement. In steady states measurements a continuous excitation laser beam is used and the PL intensity is measured in function of the wavelength, while in time resolved measurements a pulse laser is used to excite the sample and the PL is measured in function of time.

2.4.1 Steady state Photoluminescence

Steady-state fluorescence spectroscopy was performed on an Agilent Cary Eclipse Fluorescence Spectrometer. Samples were placed in a Hellma quartz cuvette with a light path of 3 x 3 mm and a total volume of 45 µl. The stationary PL for carbon nanotubes was recorded using a set-up similar to the one represented in **Figure 18**. A StradusTM diode laser modulated with a square wave using a function generator is used to excite the samples. The sample photoluminescence is then collected and collimated onto the spectrometer, the photomultiplier tube is used to detect and multiply the signal collected from the spectrometer. A lock-in amplifier, which is connected to a computer, is used to collect the emission intensity and record the spectra.

Stationary photoluminescence data in Chapter 3 were obtained at 20 °C under continuous stirring. Samples were excited at 400 nm, slits width 5 nm, and spectra where acquired between 570 and 750 nm. The spectra shown (**Figure 35**) are an average of 11 multiple scans which were acquired and automatically plotted through Cary Eclipse WinFLR software. PL measurements were processed in the same way: QDs alone and SWCNTQD heterostructures, were prepared using the same buffers and the same concentrations of QDs. As a control experiments QDs and CNT were physically mixed using the same buffers and the same concentrations of QDs and SWCNTs used in the samples with QDs alone and SWCNT-QD heterostructures without of course the presence of the activating agents EDC/S-NHS. In all cases the same amount of QDs has been exposed to the light

and the quenching can only be ascribed to the coupling of QDs covalently attached to the CNTs. The laser power on samples was stabilized to within few %.

DNA based hybrids (Chapter 4) were excited at 405 nm, while diamine linkers-based hybrids were excited at 460 nm. The SWCNTs emission spectra were recorded using the following experimental setup: two different excitation wavelengths were used: a 405 nm laser in the case of CNT-DNA-QD hybrids and a 655 nm excitation laser for the CNT-diamine linkers-QD hybrids with the set up described in **Figure 18**.

Samples in Chapter 5 were excited at 420 nm, slits width 5 nm, and spectra where acquired between 400 and 800 nm. The samples for the PL measurements were processed in the same way: QDs alone and GNF-QD hybrids, were prepared using the same buffers and the same concentrations of QDs. In all cases the same amount of QDs has been exposed to the light and the quenching can only be ascribed to the coupling of QDs covalently attached to the GNF.

2.4.2 Time Resolved Photoluminescence

Time resolved measurements are used to study the photoluminescence decay as a function of time of emitting molecules and nanomaterials. **Figure 18** shows the experimental set-up for the TRPL measurements: Laser light is generated by the Continuum Surelite (SLI-10) laser, the beam then passes through an optical parametric oscillator (OPO: Continuum Panther). Tuning the laser output at a specific wavelength is done using a computer controlled program. The beam passes through a series of lenses and it is focused onto the sample. The photoluminescence is then collected and collimated onto a Jobin Yvon Horiba Triax 550 spectrometer. A nitrogen cooled photomultiplier tube (PMT) (Photocool PC176TSCE005) is used to detect and multiply the signal collected from the spectrometer. The response from the PMT is then sent to an oscilloscope (LeCroy waverunner LT372). The photoluminescence spectra and lifetime data is recorded by a connected computer.

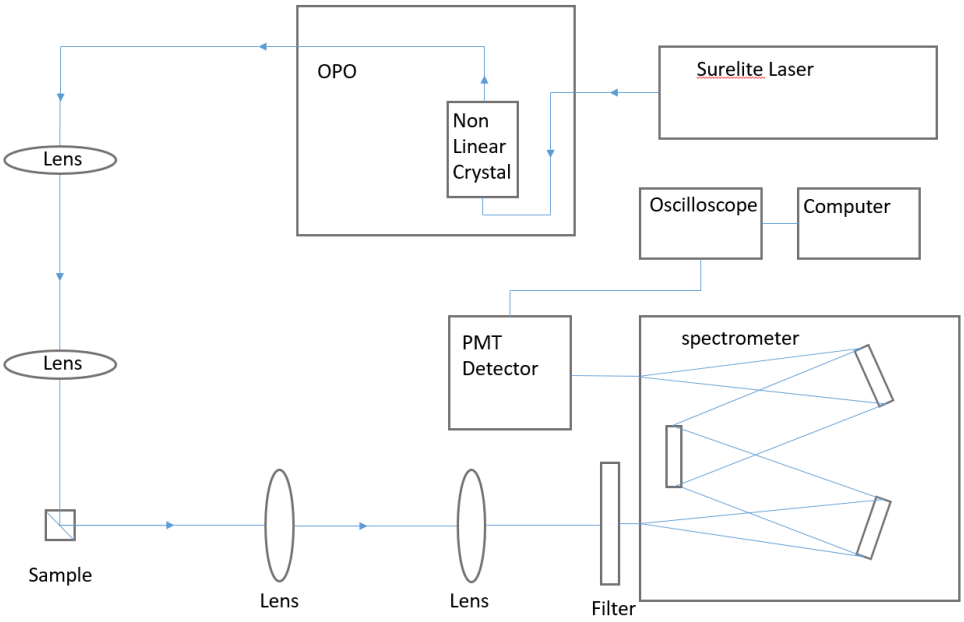

***Figure 18**:Schematic of the set-up used for time resolved photoluminescence measurements.*

Time resolved measurement in Chapter 3 were carried out on solutions of QDs alone and SWCNT-QD heterostructures prepared as described previously for stationary PL. Samples were exited at 430 nm and the emission intensity versus time was monitored at 670 nm. The software DecayFit (Fluortools) has been used to isolate the QD exponential decay from the instrument response function (IRF) in the overall recorded signal.

All samples in Chapter 4 were excited at 460 nm, while the emission was monitored respectively at 585 nm for the DNA based nanostructures and 690 nm for the diamine linkers-based nanostructures.

Samples in Chapter 5 were excited at 420 nm and the decay emission was monitored at 594 nm and 520 nm which correspond to the maximum emission of QD and GNF respectively.

2.5 Quantum Yield (QY)

The quantum yield was calculated using a relative optical method[110] which consists of the following steps: (i) measurements of the absorption and emission spectrum of the sample, (ii) choice of a suitable fluorescence quantum yield standard, (iii) choice of the measurements conditions: the excitation wavelength λ_{ex} and absorbance at λ_{ex}, same

operational settings for samples and standard, measurements of the absorption and emission spectra of the corresponding solvents which were subtracted from the samples spectra in order to remove any background signal, (iv) data calculation of the relative fluorescence quantum yield according to the following equation:

$$\Phi_{f,X} = \Phi_{f,st} \cdot \frac{F_X}{F_{st}} \cdot \frac{f_{st}(\lambda_{ex})}{f_X(\lambda_{ex})} \cdot \frac{n_X^2}{n_{st}^2}$$

The subscripts "*X*" and "*st*" denote the sample and the standard, *F* is the spectrally integrated photon flux, i.e. the area under the emission spectra, the terms n_i^2 are the refractive indexes for the solvents used for the sample and the standard.

$f(\lambda_{ex})$ is the absorption factor which provides the fraction of the excitation light absorbed by the chromophore:

$$f(\lambda_{ex}) = 1 - T(\lambda_{ex}) = 1 - 10^{-A(\lambda_{ex})}$$

Where $T(\lambda_{ex})$ and $A(\lambda_{ex})$ are respectively the transmittance and the absorbance at the excitation wavelength. In order to calculate the quantum yield, the ratio $F_i / f_i(\lambda_{ex})$ was estimated by calculating the gradients of the linear plots of the integrated fluorescence intensity (F_i) vs the absorbance at the excitation wavelength ($f_i(\lambda_{ex})$) for both samples and the standard:

$$\Phi_{f,X} = \Phi_{f,st} \cdot \frac{grad_X}{grad_{st}} \cdot \frac{n_X^2}{n_{st}^2}$$

The plots were constructed with five different solutions, with absorbance values between 0.01 and 0.1, including the origin (0,0) hence giving a straight line with gradient m and intercept =0. An excitation wavelength of 422 nm was used in all cases, which corresponds to the maximum absorbance of the chosen standard, coumarin 153, with a reported QY of 0.544 ± 0.028.[111] The absorption and emission spectra for QDs are shown

in **Figure 19**a together with the spectra of coumarin 153 (**Figure 19**b), the chosen standard. **Figure 20** shows the plots for the determination of the gradients for standard and QD alone and QD-CNT hybrids solutions with the respective gradients value.

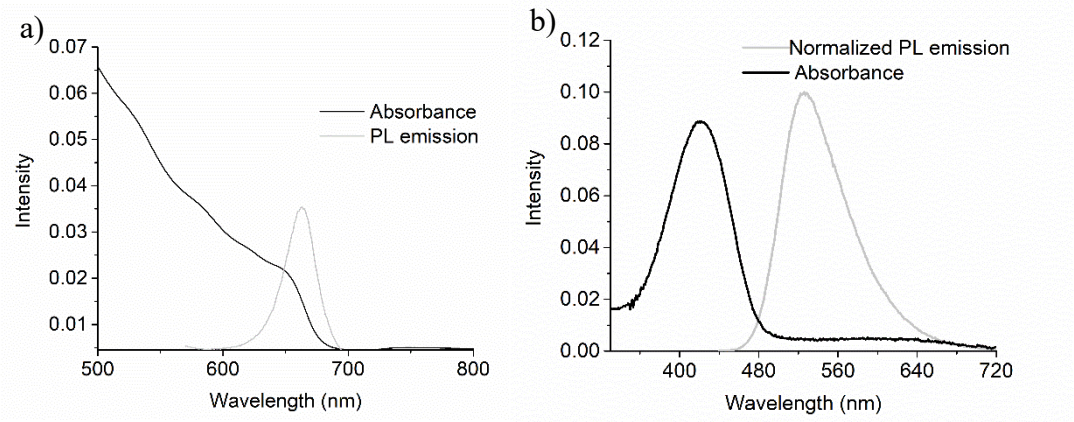

***Figure 19**: Absorbance and normalized PL emission of pristine QD (left) and coumarin 153 (right).*

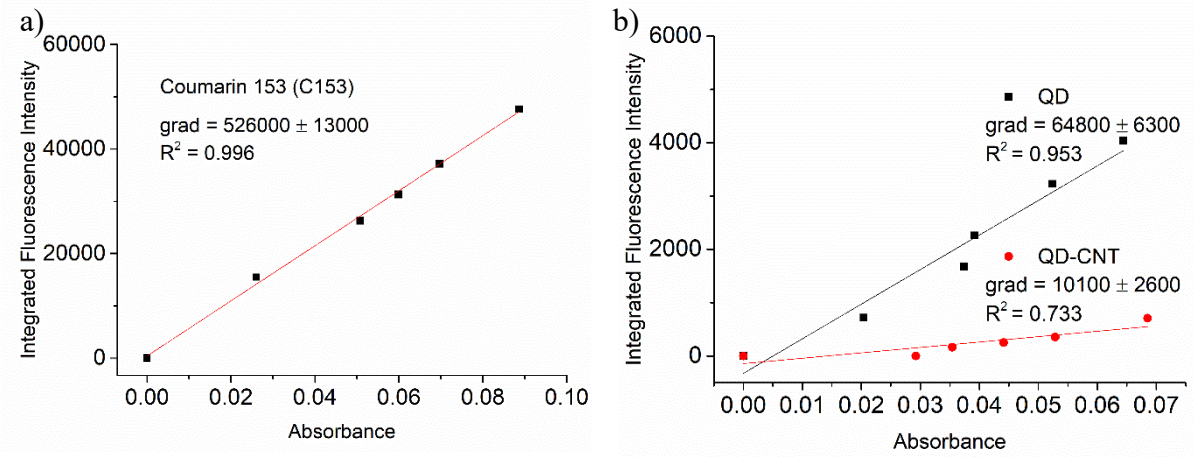

***Figure 20**: Plots of the Integrated fluorescence intensities vs absorbance of coumarin 153 (a) and pristine QD and SWCNT-QD hybrids (b) used for the calculation of the quantum yields.*

The quantum yields for pristine QDs and GNF-QD hybrids (Chapter 5) were calculated using coumarin 153 as the reference standard. The integrated fluorescence intensity for

the GNF-QD samples at different concentrations were calculated by fitting two gaussian curves to the fluorescence spectrum centred at the maxima od the PL of the flakes and of the QD, as shown in **Figure 21**. Only the area of the peak associated with the QD emission was taken into consideration for the QY calculation so that only the contribution of the QD to the total PL was considered.

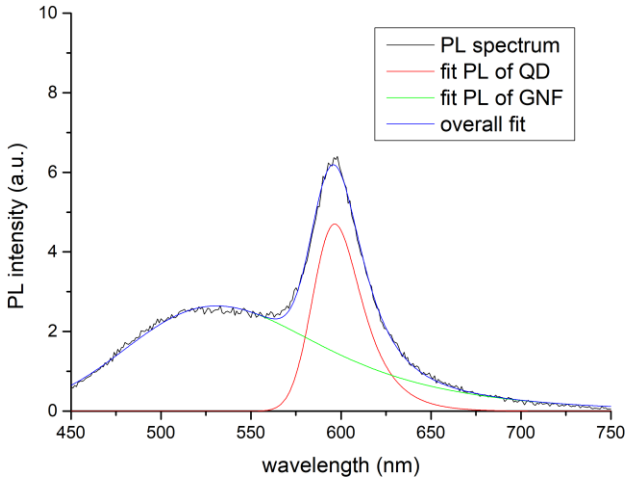

***Figure 21**: Photoluminescence spectra of GNF-QD hybrids solution with the fitting curves used to calculate the quantum yield.*

Figure 22 shows the plots for the determination of the gradients for QD alone and GNF-QD hybrids solutions with the respective gradient values.

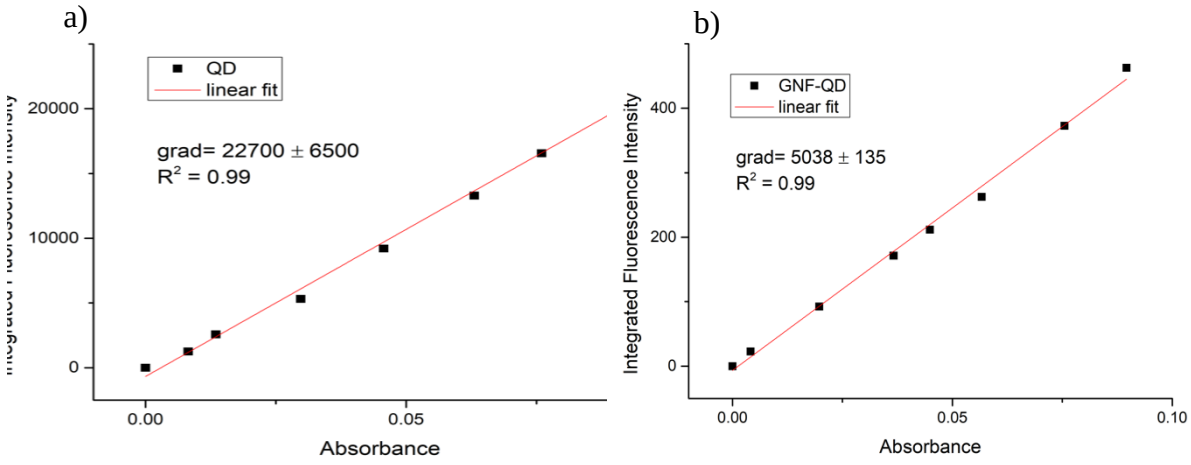

***Figure 22**: Integrated fluorescence intensity vs absorbance plots for pristine QD (a) and GNF-QD hybrids (b) used to calculate the quantum yields.*

2.6 Epifluorescence Microscopy

Epifluorescence microscopy is a form of standard fluorescence microscopy that uses particular optical components to generate high resolution images of materials. **Figure 23** shows the general working components of the light path in an epifluorescence microscope. Laser light is used to excite the sample and is directed by a dichroic mirror towards a pair of mirrors that scan the light in x and y. The light then passes through the microscope objective and excites the fluorescent sample. The emitted light from the sample passes back through the objective and is de-scanned by the same mirrors used to scan the sample. The light then passes through the dichroic mirror and is finally measured by a detector such as a photomultiplier tube, a computer reconstructs the 2D image plane one pixel at a time.

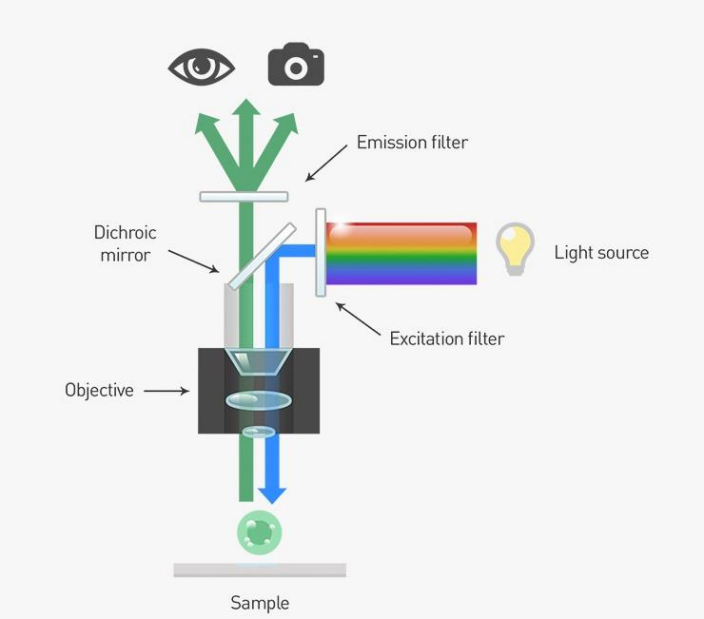

***Figure 23**:Schematic diagram of a conventional epifluorescence microscope. Image from Thermo Fisher.*

With this technique it is possible to focus on very small area on the range of um, hence it is possible to measure the photoluminescence of single fluorophores or nanoparticles such as the blinking of individual quantum dots. In the case of QD-CNT hybrids (Chapter 3) the following experimental set-up was used: the microscope includes a 442 nm He-Cd laser (Kimmon, Japan) as the excitation source. The laser is delivered and light emission is collected by the Nikon APO TIRF 100 × 1.49NA oil objective. Excitation and emission

light were separated with the aid of an appropriate dichroic mirror. Photoluminescence intensity traces were obtained from image sequences collected by the Andor Clara E 1392 × 1040 pixel cooled CCD camera. Epifluorescence microscopy measurements in Chapter 4 and 5 were carried out using Zeiss LSM710 ELYRA PS.1 system, imaging with a Plan-Apocromat 100x/1.46 oil DIC M27 objective. Typical integration times for the characterization of the blinking statistics of QDs were 100 ms (shorter integration times did not yield adequate signal to noise response). Epifluorescence microscopy measurements in Chapter 6 were carried out on an LSM 710 ELYRA PS.1 and the QDs were excited using a 488 nm laser. Time series of the nanohybrids were taken for 30 s with an exposure time of 10 ms.

2.7 Single Molecule Photoluminescence Investigations (blinking)

For real-time study and characterization of the blinking statistics, QDs were drop cast onto glass slides (VWR microscope cover glasses) previously cleaned with a plasma cleaner for 5 min (PDC- 32G-2 (230V) Plasma Cleaner, Harrick Plasma), and allowed to dry in air. Once completely dry the samples were rinsed with water and then ethanol followed by blow drying with nitrogen.

Data were first analysed with ImageJ to extract luminescence intensity data as a function of time and then processed with OriginLab9 and Matlab to generate the probability distributions. More than 40 QDs blinking traces were analysed per each sample. To extract and identify the off periods from the data the threshold was set by sampling the background and determining the average value of the background distribution and then adding 3x the standard deviation. In this way the off periods are automatically identified for all the experiments. The off periods for an experiment are binned into a histogram with 100 ms bin width. The cumulative data from all QDs blinking in a given experiment are treated as ensemble. The probability densities for the off period bins is determined by the following equation, where $P^{off}(t_i)$ is the normalized probability of off states for duration time of t_i, as defined by $N(t_i)$ which is the number of OFF events within the time bin t_i, divided by the total number of events observed (as represented by the sum of all off events for the histogram in denominator of the following equation:

$$P^{off}(t_i) = \frac{N(t_i)}{\sum_{i=1}^{n} N(t_i)}$$

The data is then plotted in log-log space as seen in **Figure 41** and **Figure 45**. The data is fit with a power law model, the slope of the linear fit being equivalent to the exponent, *m*:

$$P^{off}(t_i) = bt^{-m}$$

This procedure was used to analyse the blinking data in Chapters 3 and 4.

Samples in Chapter 5 were excited using a 488 nm laser. Time series of the graphene nanoflakes-QD nanohybrids were taken for 300s with an exposure time of 100 ms. The probability distributions (**Figure 83**) were calculated in a slightly different way compared to the methods used for the SWCNT-QD hybrids (Chapter 3 and 4). The probability densities for the off periods $P^{off}(t_i)$ is determined by the following equation:

$$P^{off}(t_i) = \frac{N(t_i)}{N_{tot}} \times \frac{1}{\Delta t_{avg}}$$

where $N(t_i)$ is the number of OFF events within the time bin t_i , N_{tot} is total number of OFF events and Δt_{avg} is the average time between neighbour events. This procedure was adopted because it provided better fit of the data compared to the method adopted in Chapter 3 and 4. The data were then plotted in log-log space as seen in **Figure 83** and fitted with a truncated power law model (Equation in **Figure 83**).

2.8 Raman Spectroscopy

Raman spectroscopic is a spectroscopic technique based on the inelastic scattering of photons by phonons.[35] The interaction of a material with incident photons of energy $\hbar\omega_L$ introduces a perturbation of the irradiated sample increasing its total energy to $E_{GS} + \hbar\omega_L$,

where E_{GS} is the ground state energy. In general, $E_{GS}+ \hbar\omega_L$ is not a stationary state and the system is said to be in a virtual state. Since the new state of energy $E_{GS}+ \hbar\omega_L$ is not a stationary state the photon leaves this unstable situation and is emitted by the perturbated system returning to the original stationary state (**Figure 24**).

The emission process can follow different pathways: If the frequency of the emitted photon is the same as the incident one a Rayleigh scattering takes place. This is also called elastic scattering when only the propagation direction of the photon changes. On the other hand, with a much smaller probability then the Rayleigh scattering, during the interaction process the photon can lose or gain energy, and the Raman scattering takes place. If the photon loses part of its energy, thus exciting the sample with a lower energy $\hbar\omega_{Sc}$. This process corresponds to the Stokes process. Since the sample has to return to a stationary state, there is a loss of energy of $\hbar\omega_L - \hbar\omega_{Sc} = \hbar\Omega$. If the incoming photon finds the sample in an exited vibrational level, and after the interaction the system returns to the ground state, the emitted photon has gained energy $\hbar\omega_{Sc} = \hbar\omega_L + \hbar\Omega$. This corresponds to the Anti-Stokes process. Since the Stoke process is the most probable, the majority of Raman spectra are Stokes measurements where the intensity of the scattered light is plotted as a function of the difference between the incident and scattered photon energy, hence called "Raman shift".

For most of the cases the excited state $E_{GS}+ \hbar\omega_L$ does not correspond to a stationary state but if the excitation is selected to match a specific energy level, the process is resonant and as a result of the greater perturbation the intensities of the Raman signal are strongly enhanced. Using Infrared to ultraviolet light, the main scattering mechanism involves electronic excitations as intermediate states thus the use of Raman spectroscopy to study the electronic properties of a given material.

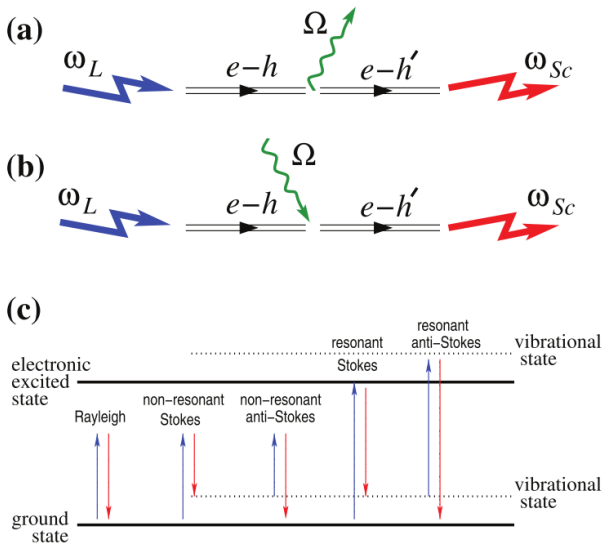

***Figure 24**:Schematic of Raman Scattering. (a) Stokes. An incoming photon ω_L excites an electron-hole pair e-h. The pair decays into a phonon Ω and another electron-hole pair e-h'. The latter recombines, emitting a photon ω_{Sc}. (b) Anti-Stokes. The phonon is absorbed by the e-h pair. (c) Rayleigh and Raman scattering in resonant and non-resonant conditions.(taken from ref* 112*).*

The Raman measurements were carried out on a Renishaw Ramascope using a 514.5 nm wavelength laser using a 50-fold magnification objective. Each spectrum was scanned for 20 seconds and collected 8 times. The acquired spectra were then calibrated against silicon wafer.

Samples for Raman spectra measurements were prepared by drop casting the solutions of QD and GNF-QD onto glass slides (VWR microscope cover glasses) previously cleaned with a plasma cleaner for 5 min (PDC- 32G-2 (230V) Plasma Cleaner, Harrick Plasma) and let dry in air. In order to access the down shift of the D and G peaks in the presence of QDs a baseline correction was subtracted to the raw data as shown in **Figure 25**. The broad peak at around 2500 cm-1 corresponds to the QD PL emission.

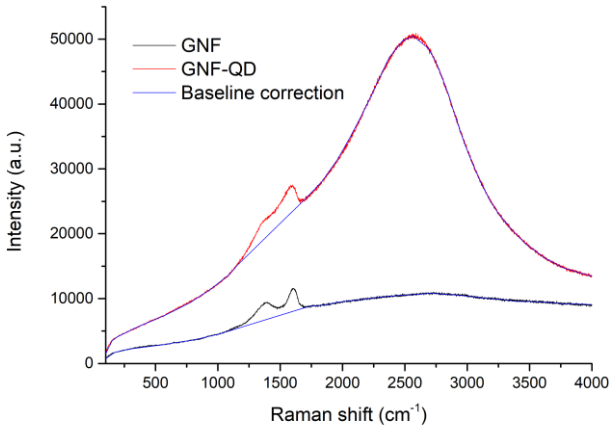

***Figure 25**: Raman spectra of pristine GNF (black) and GNF-QD hybrids (red). The blue lines were used as a baseline correction to evaluate the G and D peaks down-shift. The broad peak at around 2500 cm^{-1} corresponds to the QD emission.*

2.9 Solar Cell Fabrication

Solar cells were assembled using a premade kit from Greatcell solar consisting of TiO_2 coated transparent glass electrodes and platinum coated counter electrodes. Pristine QD and GN-QD hybrids (0.2 mg/ml of GNF and 2 uM of QD) were drop casted on the TiO_2 coated electrodes on a hot plate at 40 C for 30 min and then under vacuum at 40 C for 3 hours. The same amount of QD was used for all the devices tasted. Solar cells were assembled in a sandwich configuration were parafilm was used to create a chamber between the two electrodes in order to accommodate the electrolyte solution (0.1 M Na_2S).

2.10 Photo-current Measurements

Photocurrent measurements have been carried out under ABET Sun Simulator AAA with AM1.5 filter. The solar cells were irradiated at 1 sun (100 mW/cm^2). The irradiation was calibrated with a reference Silicon solar cell. The photo-response of solar cells has been measured using an oscilloscope GW Instek GDS-2062.

2.11 Sample Deposition

Adopting drop cast techniques, solutions of SWCNT-QD (Chapter 3) were cast onto Sigmacote® treated SiO_2 surfaces and allowed to dry in air. Once fully dry, the samples were washed with ethanol and ultra-pure water followed by blow drying with nitrogen.

Experiments were performed on 500-550 μm thick silicon wafers (Silicon Quest International) covered on both sides with 295nm of thermal silicon oxide (SiO2), cut into 1cm^2 sections with a diamond tip scriber. Once cut, all SiO_2 substrates were exposed to piranha solution for 5 minutes before being washed with ultra-pure H2O and ethanol (VWR), and dried under nitrogen flow. Piranha solution is a strong oxidising agent and was made up of sulfuric acid (H_2SO_4, VWR) and hydrogen peroxide (H_2O_2, Sigma Aldrich) in a 3:1 ratio respectively. Once cleaned, surfaces were treated with Sigmacote® (Sigma Aldrich) self-assembled monolayer (SAM) solution via overnight incubation. Sigmacote® SAM solution consisted of: toluene (200mL, VWR), acetic acid (3mL, Sigma Aldrich) and Sigmacote® (10mL). Once overnight incubation was complete, surfaces were washed with acetone (VWR), ethanol and ultra-pure H_2O and dried under nitrogen flow.

Solutions of SWCNT-QD, where diamine linkers or DNA, were employed as molecular rulers (Chapter 4) were drop casted for 30 minutes on pretreated mica surfaces with a 0.5 $MgCl_2$ solution and then rinsed with water and ethanol.

Adopting drop cast techniques, solutions of graphene nanoflakes (GNF) and GNF-QD hybrids (Chapter 5) were cast onto freshly cleaned highly oriented pyrolytic graphite (HOPG) surfaces for few minutes and then washed with ethanol and ultra-pure H_2O followed by blow drying with nitrogen.

2.12 Chemical Techniques

2.12.1 Carbon nanotubes preparation

Oxidized SWCNTs (Chapter 4) were prepared by chemical oxidation to cut SWNTs into open-ended tubes. For the experiment, 8 mg HiPco nanotubes (Carbon Nanotechnologies Inc.) were suspended in 10 mL of a 3:1 mixture of concentrated H_2SO_4 (95-98 wt %; Sigma-Aldrich)/HNO_3 (69 wt %; VWR) and sonicated in a water bath for 15 min at 30 °C. Then, the SWCNTs suspension was collected on a 0.1 μm centrifugal filters (Merck

Millipore Ltd.), washed with DI water and allowed to dry. The acidic cutting step opens the ends of the SWNTs and introduces carboxyl groups at the open-ends and at defect-sites of the SWNTs, which represent useful sites for further functionalization. The oxidized SWCNTs were dispersed in DI water according to published procedures[61] Briefly, 1 mg of oxidized SWCNTs was suspended in an aqueous solution, containing NaCl (0.1 M; Fisher Scientific) and d$(GT)_{20}$-ssDNA (Integrated DNA Technologies). The suspension was kept in an ice-water bath and sonicated (Ultrasonic Cleaner, VWR) for 90 minutes. After sonication, the dispersion was divided into 0.1 ml aliquots, centrifuged for 90 minutes at 13000 RPM to remove insoluble materials, and the supernatant collected. The dispersion process not only allows the dispersion of SWCNTs in water, but also protects the side-wall of nanotubes leaving the open-ends available for a direct functionalization. The supernatant, containing DNA dispersed CNT was collected sand purified by means of Size-Exclusion Chromatography (SEC)[113] giving carbon nanotubes sorted by length (100-400 nm) at a concentration of 40ug/ml.

2.12.2 SWCNT-QD Hybrids Formation (Chapter 3)

DNA wrapped SWCNTs were dispersed in DI water according to published procedures:[61] typically, 1 mg of HiPco nanotubes was suspended in 1 ml aqueous DNA (integrated DNS technologies) solution (1 mg/ml DNA; 0.1 M NaCl), and was sonicated in an ice bath for 90 minutes at a power level of 3 W (Sonics, VC130). After sonication, the samples were divided into 0.1 ml aliquots, and centrifuged (Eppendorf 5415C) for 90 minutes at 16000 g to remove insoluble material, leaving DNA-dispersed nanotube solutions at a mass concentration in the range of 0.2 to 0.4 mg ml^{-1}. Segments of defined length where obtained by size exclusion chromatography,[113] at a final nanotube concentration of 40 µg/ml.[114] CdSe/ZnS core/shell QDs functionlized with cysteamine were purchased from Crystalplex. The QD-SWCNT heterostructures were formed via an amidation reaction between terminal DNA-wrapped SWCNT carboxylic defects and amino terminated quantum dots. Amide bond formation in aqueous conditions was performed with coupling reagents 1-ethyl-3-[3- dimethylaminopropyl]carbodiimide hydrochloride (EDC, Sigma Aldrich) and N-hydroxysulfosuccinimide sodium salt (sulfo-NHS, Sigma Aldrich). Pristine DNA wrapped SWCNTs solutions in DI water (6.25 µg mL−1) were mixed in a 1:1 volume ratio with a solution of 4×10^{-3} M EDC and 10 × 10−3 M sulfo-NHS in 0.2 M MES buffer (pH 4.7, 0.2 M, ThermoScientific). The solution

so prepared was left activating for 30 min and then diluted 1:1 (by volume) with a ThermoScientific BupH Phosphate Buffered Saline (pH 7.2, TPBS, ThermoScientific) solution and left activating for 1 h. The QDs at an initial concentration of 25 mg mL^{-1} were diluted in water and then added to the SWCNT solution in a 1 to 1 volume ratio and left incubating overnight.

2.12.3 Assembly of SWCNT-QD using diamine linkers and DNA (Chapter 4)

The functionalization of the SWCNTs with amine linkers (DNA amine modified linkers and diamine linkers) was carried out according to the following procedure: SWCNTs (6.25 ug/mL) were mixed in a 1:1 ratio with MES buffer (0.2M; pH 4.7; ThermoScientific) containing 1-ethyl-3-[3-dimethylaminopropyl]carbodiimide hydrochloride (EDC; 4 mM; Sigma-Aldrich) and N-hydroxysulfosuccinimide (sulfo-NHS; 10 mM; Sigma-Aldrich). The solution was shaken at room temperature for 30 min, and then Dulbecco's phosphate buffered saline (DPBS), purchased from Thermo Scientific, was added in a 1:1 ratio.

Linkers were added to the activated tubes according to the following procedures:

-Diamine linkers: diamine linkers, (p-Phenylenediamine, Benzidine, 4,4"-diamino-p-terpheny, Hexamethylenediamine, 1-8 diaminootane, 1-10 diaminodecane, 1-12 diaminododecano) were added in a tenth of the total reaction volume of activated CNT giving a final linker concentration of 10 uM. The solution was shaken at room temperature overnight. Excess linker was removed by dialysis against a 30 mM NaCl water solution using Slide-A-Lyzer MINI Dialysis Devices with a 20 kDa cutoff purchased from Thermo Scientific, for two hours twice and the overnight replacing the dialysis solution for each cycle. Carboxylated cadmium telluride quantum dots at a concentration of 0.2 mg/ml were activated for 10 minutes in 2 mM EDC and 3 mM S-NHS in DPBS buffer. To conjugate QDs to SWCNTs, the solution of activated QDs was mixed with the SWCNT functionalized with the diamine linkers in a 1:10 volume ration and allowed for reaction for 1 hour. The solutions containing the hybrid were further dialyzed vs a 30 mM NaCl solution for 1.5 hours twice in order to remove the excess of unreacted EDC and S-NHS. This second dialysis was required because the excess of coupling reagents might react with the carboxyl groups on the QD surface affecting their photoluminescence and stability in solution.

-DNA linkers: The dsDNA (see Table 5 for oligonucleotide sequences) was hybridized in DPBS at a concentration of 2.5 μM. The dsDNA was added in a tenth of the solution of activated tubes giving a final dsDNA concentration of 250 nM. The solution was shaken at room temperature overnight. Excess linker was removed by dialysis against TAE buffer (1x) with NaCl (100 mM) using Slide-A-Lyzer MINI Dialysis Devices with a 20 kDa cutoff purchased from Thermo Scientific. To conjugate QDs to SWCNTs, a solution of Qdot 585 Streptavidin Conjugate (100 nM) was added to freshly dialyzed SWCNT−DNA solution to give a final QD concentration of 5 nM. The reaction was shaken for 40 hours at room temperature in the absence of light. This concentration of QD was found to be optimum for maximizing the functionalization of SWCNTs while minimizing the number of free QDs.

2.12.4 Assembly of Graphene nanoflakes-QD hybrids (Chapter 5)

Graphene nanoflakes were dispersed in water by simple mixing at a concentration of 0.1-1 mg/ml. CdSe/ZnS quantum dots functionalized with amino groups were purchased from Ocean Nanotech. QD-GNF nanohybrids were formed in aqueous solution by mixing equal volumes of water solutions of nanoflakes (0.4 mg/ml) and QDs (3uM) and allowed for reaction overnight under continuous stirring.

To study the effect of pH on the coupling reaction formation, equal volumes of GNF and QD dispersed in the appropriate buffer (MES 0.1M pH 4.7; PIPES 10 mM pH 6.1, ThermoScientific BupH Phosphate Buffered Saline pH 7; HEPES buffer 10mM pH 8; sodium carbonate 30mM-sodium bicarbonate 70 mM buffer pH 9.5) were mixed and allowed for reaction overnight under continuous stirring. To study the effect of solvent polarity on the coupling reaction formation, equal volumes of GNF and QD dispersed in different ethanol/water volume ratio (0/10,1/10,3/10,5/10,7/10,9/10 and 10/10) were mixed and allowed to react overnight under continuous stirring.

2.12.5 Reactions for the Graphene Electrodes Functionalization (Chapter 6)

2.12.5.1 EDC/S-NHS Coupling

The following protocol has been used for EDC/S-NHS mediate amidation reaction of graphene electrodes with amino functionalized QDs: QDs were dispersed in a DPBS

buffer (pH 7) solution of EDC (2mM) and Sulfo NHS (5mM) at a concentration of 4nM. The silicon chip with the patterned graphene electrodes was immersed in this solution and left for reaction 2 hours. After that the chip was rinsed subsequently with DPBS, ultrapure water and ethanol and finally blow dry with compressed air. The substrates were then imaged with AFM using tapping mode.

2.12.5.2 Reductive Amidation Reaction

The following protocol has been used for the reductive amidation reaction of graphene electrodes with amino functionalized QDs: The silicon chip with the patterned graphene electrodes was immersed in QDs solution of carbonate buffer pH 9.5 0.1 M at a concentration of 4nM and left for reaction 3 hours. After that the chip was immersed in a 10 mM $NaCNBH_3$ in DPBS solution and left for reaction 30 minutes. The chip was then extensively rinsed with DPBS, ultrapure water and ethanol and finally blow dried with compressed air. The substrates were then imaged with AFM using tapping mode.

2.12.5.3 DSC Coupling

The following protocol has been used for the DSC mediated coupling of graphene electrodes with amino functionalized QDs: Before reaction the silicon chip was left in a dissicator overnight to remove traces of water on the chip surface. A 50 mg/ml solution of DSC in anhydrous DMF was dropped cast on the silicon chip and left incubating for 2 hours in a glove box to prevent any water contaminations. The chip was then rinsed three times with DMF. The chip was then immersed is 40 nM solution of amino QDs in DPBS buffer under constant stirring and left for reaction for 2 hours. The chip was then extensively washed with DPBS, water and ethanol and finally blow dried with compressed air. The substrates were then imaged with AFM using tapping mode.

2.12.5.4 Mannich Type Reaction

The following protocol has been used for the reductive amidation reaction of graphene electrodes with amino functionalized QDs: The chip was immersed in a 1:4 volume ratio of 37 % formaldehyde solution and a 150 mM NaCl, MES 0.1 M, pH 4.7 buffer solution of QD (4nM) solution for 5h at 45 C under constant stirring. The chip was then

extensively washed with MES buffer, ultrapure water and ethanol and finally blow dried with compressed air. The substrates were then imaged with AFM using tapping mode.

3 CARBON NANOTUBES-QD HYBRIDS

3.1 Introduction

The possibility of integrating nanomaterials with different properties into functional heterostructures is key to the development of future nanoelectronic devices, and can lead to new functionalities and emergent behaviour at interfaces.[16] In this regard, whereas semiconductor quantum dots (QDs) are tunable emitters and efficient broadband light harvesting systems for new generation photovoltaic devices and light-emitting diodes,[115–117] single-walled carbon nanotubes (SWCNTs) are ideal 1D scaffolds to collect and transport charges for device implementation.[118–124] Therefore, the combination of SWCNTs and QDs into novel nanohybrid structures has drawn interdisciplinary attention for a wide range of applications including photovoltaics,[125] photocatalysis,[126] sensing,[127] bioimaging,[128] and quantum information processing.[129]

Numerous Quantum dot–carbon nanotube derivatives have been fabricated and characterized. In this regard, different approaches have been used to functionalise carbon nanotubes with nanoparticles, including through the formation of nanoparticles directly on the tubes or via a building block approach where pre-synthesized nanoparticles are connected to functionalized CNTs.[130,131] The most common strategy to covalently link carbon nanotubes with nanoparticles and quantum dots is the oxidation of the tubes in acidic conditions in order to introduce carboxyl (and hydroxyl) groups as defects on the nanotubes surface. The presence of these functionalities increases the CNTs' solubility and provides active sites for their subsequent functionalization.[71,132,133] This strategy presents two main disadvantages: the carboxyl groups, even if present prevalently at the nanotubes tips, are also present along the side of the tubes; this leads to a lack of control over the tethering location for the nanoparticles attachment that can therefore be linked both on the side wall and at the terminal ends. Moreover, the acidic treatment breaks the nanocarbon π –network, and therefore can have a detrimental effect on the mechanical, thermal and electronic properties of the tubes.[134,135]

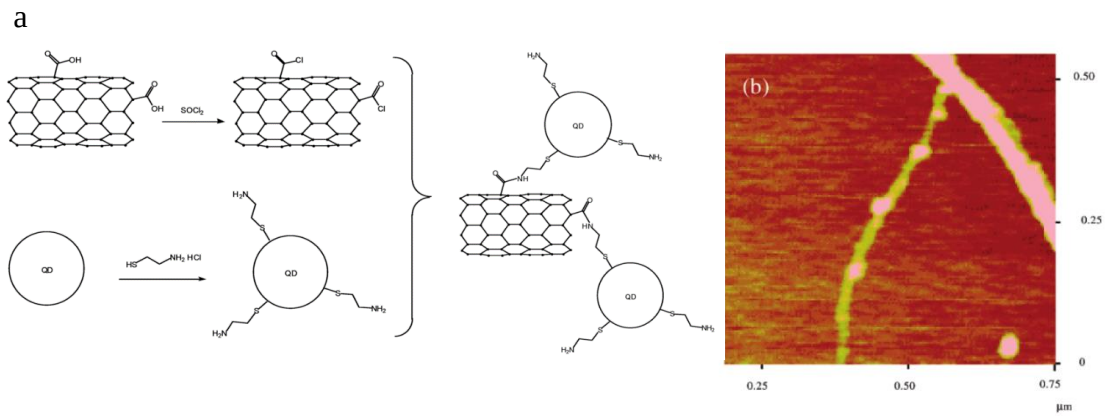

***Figure 26**:Formation of QD-SWNT Complexes via a Chemical Coupling Procedure (a) and AFM image of a nanotube with attached QDs along its sidewall (b). (taken from ref* 136*).*

A covalent attachment of as prepared QDs to SWCNT has been carried out through $SOCl_2$/amide coupling by Haremza et al,[136] see **Figure 26**, or with a similar strategy to multiwalled CNT.[137] Other strategies have been proposed and implemented, including the in-situ growth of QDs as reported by Banerjee et al[101] or the in solution QDs attachment to functional groups of DNA in DNA wrapped CNT.[138,139] Nevertheless, in all these approaches it has proven challenging to control the spatial localization and the number of nanoparticles per tube, resulting in the tethering of QDs on both the terminal ends of the tubes as well as on their side walls.

Since the properties of any material are strongly dependent on their atomic structures and interactions at the interfaces, specially at the nanoscale level where the material properties are drastically changed, the control over the morphology of the synthetized hybrids is a most desired feature. Consequently, it is important to develop structurally homogeneous samples and microscopic assemblies with well controlled nanoscale interfaces, ideally with single-particle resolution, an aspect that in turn is crucial for future device integration.

Here it is presented a simple and general controlled assembly strategy for the formation of carbon nanotube-quantum dot nanohybrids, where the terminal ends of individual single-walled carbon nanotubes (SWCNT) are selectively functionalised with single quantum dots (QDs), via the formation of covalent bonds. Evidence of electronic coupling

suggesting an increased photoinduced charging of the nanocrystals is provided with single particle control.

3.2 CNT-QD Heterostructures

A water-based coupling strategy was carried out where single QDs are attached to individual single walled carbon nanotubes. An ex situ approach is employed, where amino-functionalized semiconductor QDs are covalently bond univocally at the terminal ends of DNA wrapped CNTs via selective amidation reactions. This strategy allows to carry out the coupling in water without the use of organic solvent or acidic treatments of the nanocarbon material. Moreover, the immobilization of the nanoparticles to the CNT terminal ends through covalent bonds grants close proximity between the two moieties and a precise control over the position of the QDs on the tubes. This can allow for optimized electronic coupling at the organic-inorganic interface, with energy and charge transfer processes occurring over these short length scales.

3.2.1 Assembly

SWCNTs were sonicated and dispersed in water via side-wall interactions with single-stranded DNA as described by Palma et al[69,140] to form molecular junctions. In this strategy different molecular linkers were used to bridge SWCNT in aqueous solution, via self-assembly. With this approach it has been possible not only to solubilize the SWCNT in water, with the DNA acting as a dispersing agent, but also use the DNA wrapped around the tubes as a protecting agent towards the tube functionalization along the side walls leaving only the terminal ends available for functionalization. This allowed to bridge single carbon nanotubes by end to end junctions.

A similar side-wall protection procedure has been used to covalently link amino terminated CdSe/ZnS core/shell nanocrystals univocally at the terminal ends of individual SWCNTs via an EDC/S-NHS mediated amidation reaction in aqueous solution as shown in **Figure 27**. This strategy allowed to carry out the covalent coupling in environmentally friendly and biocompatible solutions without the use of potentially detrimental acid treatments of the CNTs.

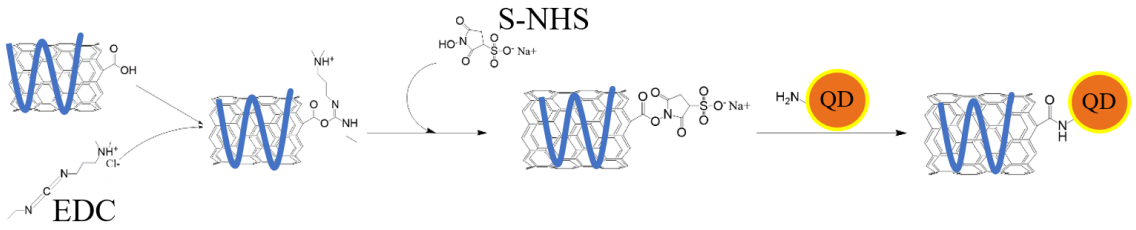

***Figure 27**:Schematic of the EDC/S-NHS mediated coupling reaction scheme for the tethering of amino functionalized QD to the terminal end of SWCNT.*

EDC (1-ethyl-3-(3-dimethylaminopropyl) carbodiimide hydrochloride) is one of the most popular carbodiimide used for particle and surface conjugation of biological substances[141] and it is often used along with NHS or sulfo-NHS esthers (N -hydroxysulfosuccinimide). N-substituted carbodiimides can react with carboxylic acids to form highly reactive, o-acylisourea intermediates (see ***Figure 28***). This active species then can react with a nucleophile such as a primary amine to form an amide bond[142]. In aqueous solutions, hydrolysis by water is the major competing reaction, cleaving off the activated ester intermediate, forming an isourea, and regenerating the carboxylate group.

The yield and effectiveness of the reaction is influenced by the pH, in particular it has been reported that carboxylate activation occurs most effectively with EDC at pH 3.5–4.5, while amide bond formation occurs with highest yield in the range of pH 4–6. However, EDC hydrolysis occurs maximally at acidic pH values with increasing stability of the carbodiimide in solution at or above pH 6.5.[143] In this regard, the EDC coupling reactions is usually performed between pH 4.5 and 7.5.

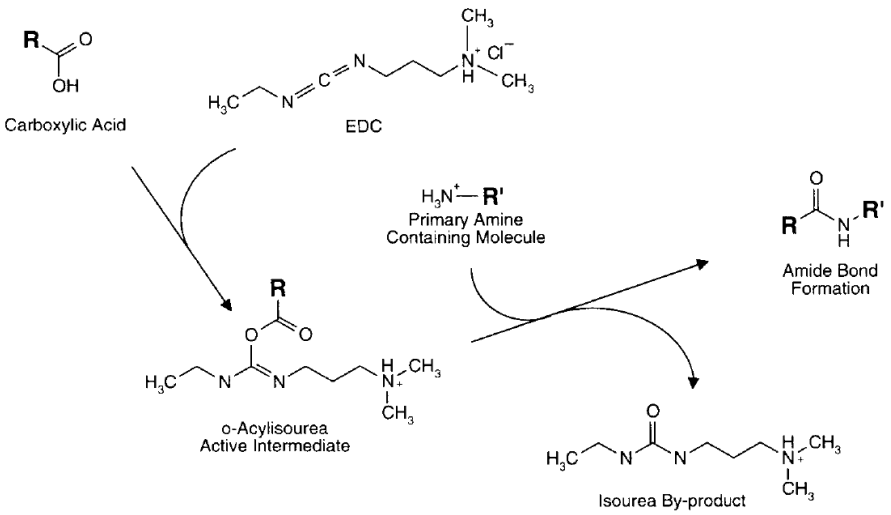

Figure 28*: Schematic of the EDC/S-NHS coupling mechanism. (taken from ref* 144***).***

Sulfo NHS is usually used together with EDC because it increases the solubility and stability of the active intermediate which ultimately reacts with the attacking amine containing moiety.[143] EDC reacts with a carboxylate group to form an active ester (o-acylisourea) leaving group (***Figure 28***) but unfortunately this reactive complex is slow to react with amines and can hydrolyze in aqueous solutions. If the target amine does not find the active carboxylate before it hydrolyzes, the desired coupling cannot occur.

The formation of a sulfo-NHS ester intermediate from the reaction of the hydroxyl group on sulfo-NHS with the EDC active-ester complex results in a more stable intermediate and hence the yield of the reaction increases significantly over that obtained with EDC only.[145] Since the concentration of added sulfo-NHS usually is much greater than the concentration of the target molecule, the reaction preferentially proceeds through the more efficient sulfo-NHS ester intermediate. The final product of this two-steps reaction is the same one obtained using EDC alone: the activated carboxylate reacts with an amine to give a stable amide linkage.[144]

3.2.2 Atomic Force Microscopy

The formation of QD-SWCNT heterostructures was monitored by casting the aforementioned solutions on silicon wafer substrates and imaging them with atomic force microscopy (AFM) to study the assembly and the relative position of the dots on the tubes.

Figure 29 and **Figure 30** show the AFM images of the pristine materials with the respective average length for the SWCNT and average height for the QDs. **Figure 31** shows a representative image of the nanohybrids obtained in this study and it can be noticed how the coupling occurred uniquely at the terminal ends of the CNTs as indicated by the arrows where the QDs can be easily identified as the round sphere at the terminal ends of the tubes through the height profile across the hybrids.

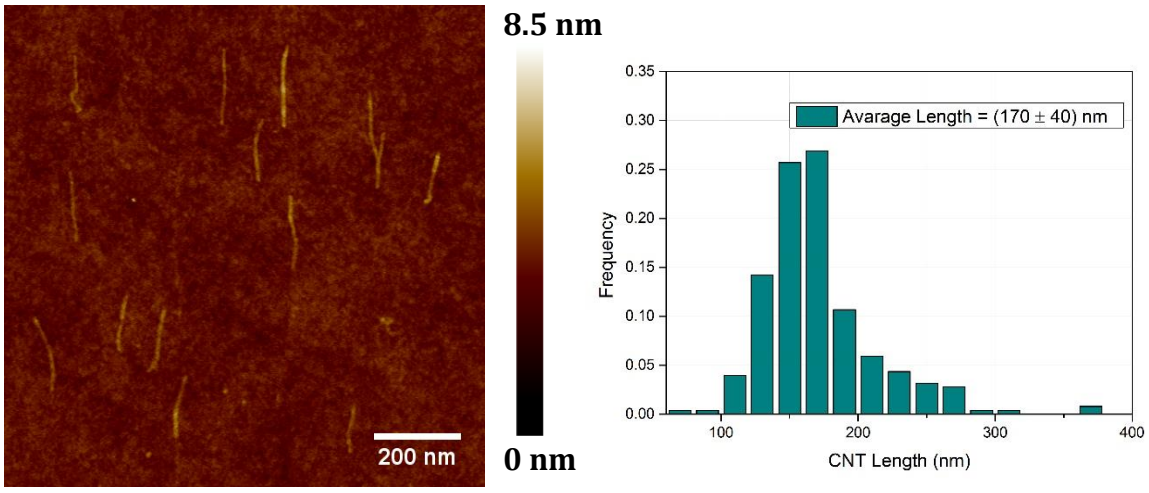

***Figure 29**:AFM topographical image of pristine DNA-wrapped SWCNTs (left) and histogram of the CNT topographical length (right) measured from AFM images. Average length: 170 ± 40 nm.*

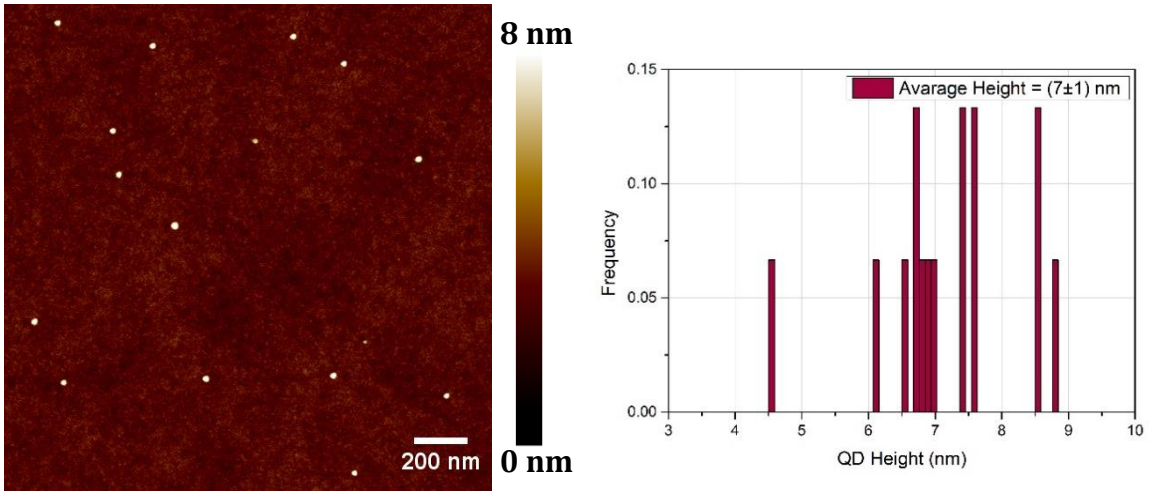

***Figure 30**: AFM topographical image of pristine amino terminated CdSe/ZnS core/shell QDs (left) and histogram of the QDs topographical profile measure from AFM images. Average Height: 7 ± 1 nm.*

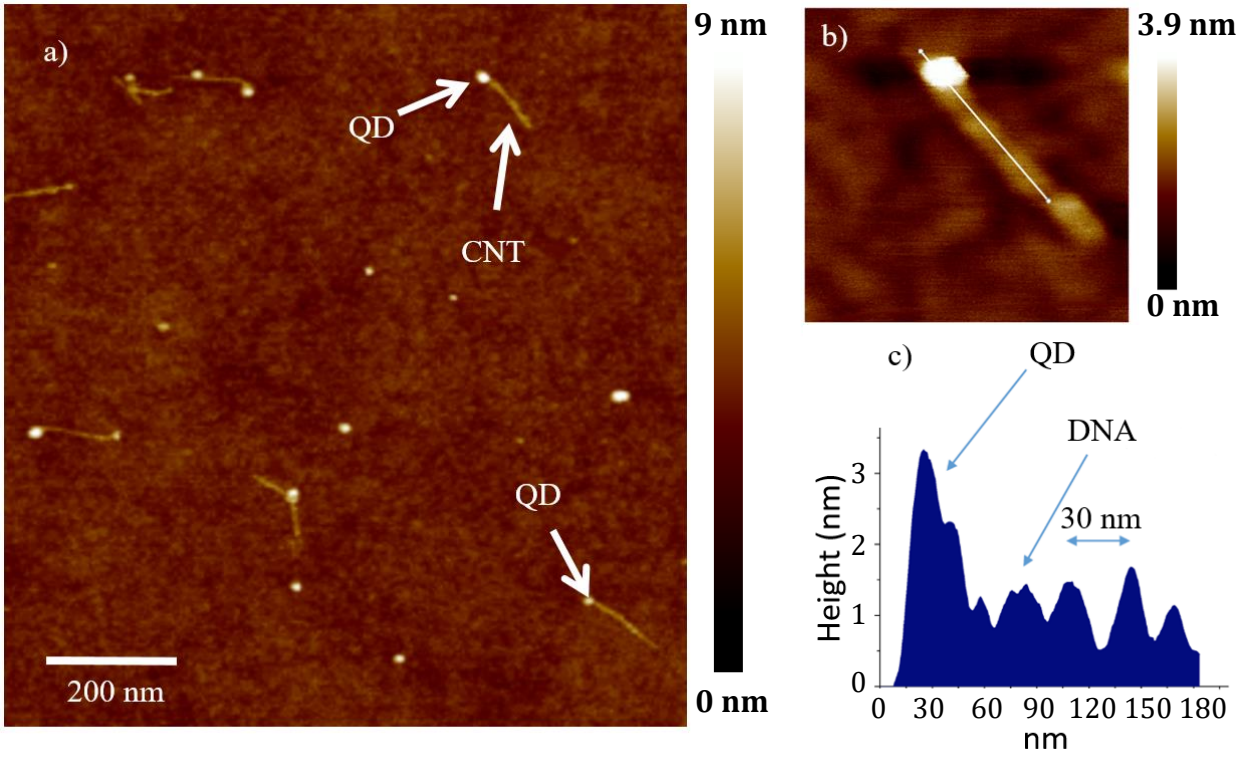

***Figure 31**: a) Representative AFM topographical image of SWCNT-QD heterostructures. b) AFM topographical image of monofunctionalized SWCNT-QD structures. c) height profile along the line drawn in figure b) which shows also the bumps of the DNA wrapped along the tubes with a pitch of ≈ 30 nm.*

It has been typically observed the formation of monofunctionalized hybrids (1:1), where a QD was attached at only one end of the SWCNT (***Figure 32***a) or bi-functionalized hybrids (2:1), where both ends of the SWCNT are functionalized with QDs (***Figure 32***b). Only in very few cases (less than 5%) one quantum dot was found bridging two nanotubes (see ***Figure 32***c). The lack of significant presence of CNT/QD/CNT heterostructures was mainly attributed to steric hindrance effects and partial electrostatic repulsion between the DNA-wrapped CNTs and the amino-terminated QDs.

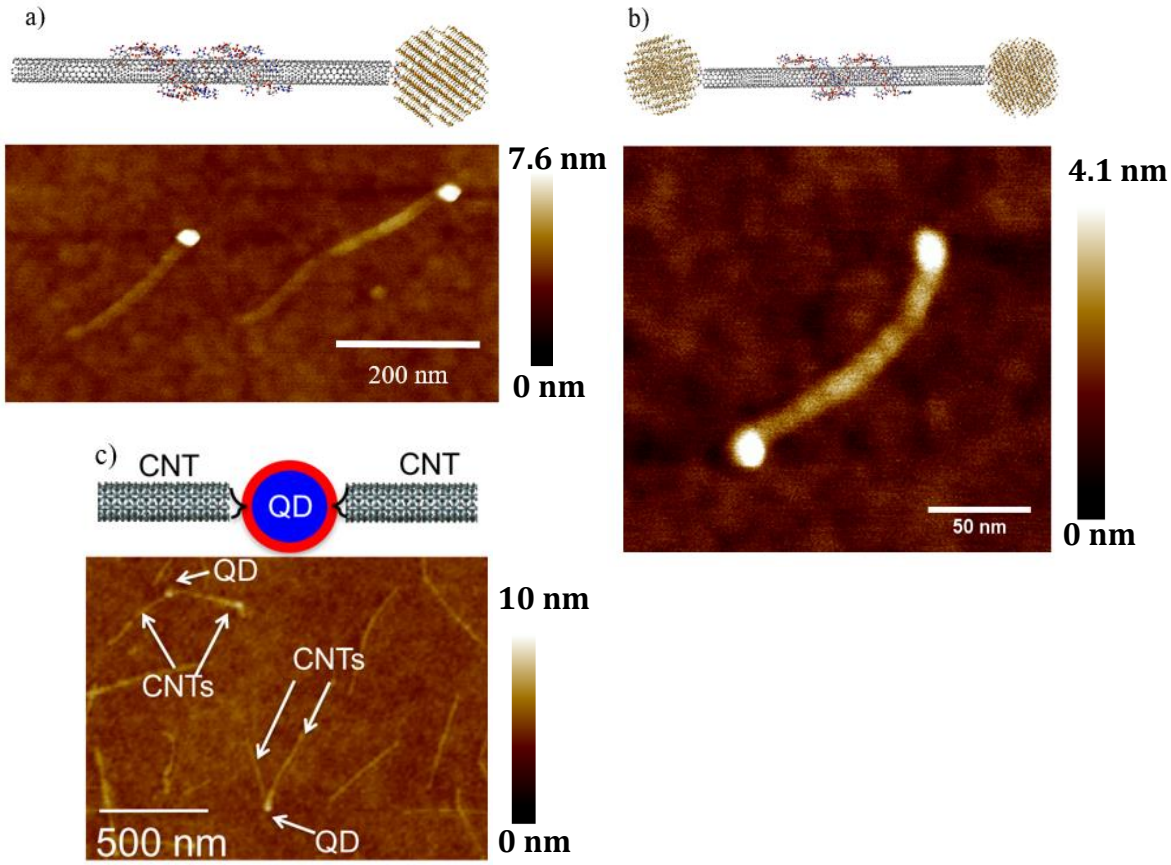

Figure 32:*a) Schematic and AFM topographical image of monofunctionalized SWCNT-QD structures. b) Schematic and AFM topographical image of bis-functionalized SWCNT-QD structures. c) Schematic and AFM topographical image of one QD bridging two carbon nanotubes.*

The formation of monofunctionalized SWCNT-QD nanohybrids was maximized while minimizing the assembly of bis-functionalized heterostructures by changing the QD/CNT mass ratio. The yield of hybrids formation, defined as the number of hybrids divided by the total number of tubes, was estimated by AFM obtaining, in the best cases, 35 % for the mono-functionalized hybrids and ≈5% for the bis-functionalized hybrids. The yield of conjugation was investigated as a function of the quantum dot/nanotube mass ratio (**Figure 33**), and obtained solutions where 92% of the nanohybrids assembled were composed by monofunctionalized SWCNT-QD structures. Conversely, the formation of 2:1 QD-SWCNT heterostructures was limited to only ≈8%.

The yield of attachment of QDs to CNT has been carried out by counting the number of QDs at the terminal ends of the nanotubes of over 100 nanotubes per each sample. The QDs can been identified through their shape and height section profile from the AFM images collected.

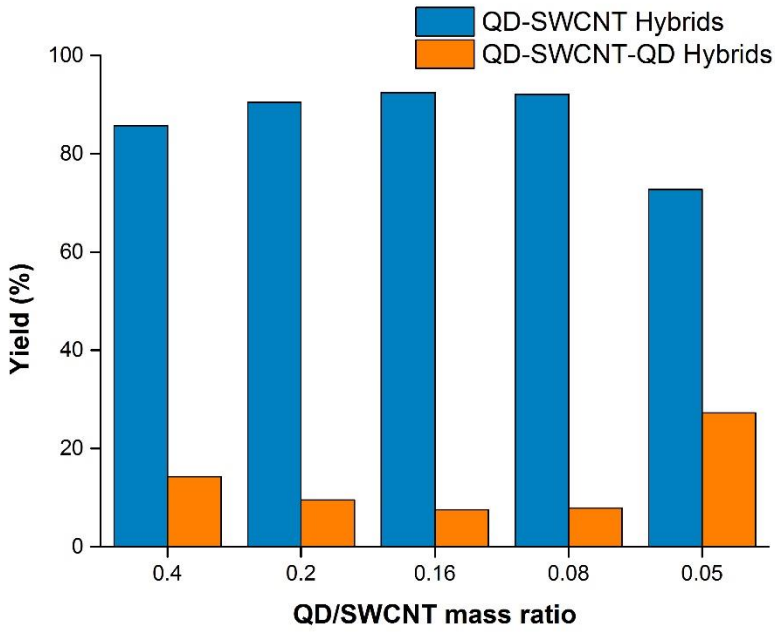

***Figure 33**:Yield of conjugation of the QDs at the terminal ends of SWCNT among the nanohybrids assembled. The number of QDs per nanotubes has been controlled obtaining in the best case 92% of monofunctionalized SWCNT-QD and less than 8% of 2:1 QD-SWCNT heterostructures among the total number of hybrids.*

As a control experiment QD were mixed with the SWCNT without any coupling reagents, and, as it is shown in **Figure 34**, no QDs are attached on the tubes indicating that there is not a nonspecific attachment of the nanoparticles at the terminal ends.

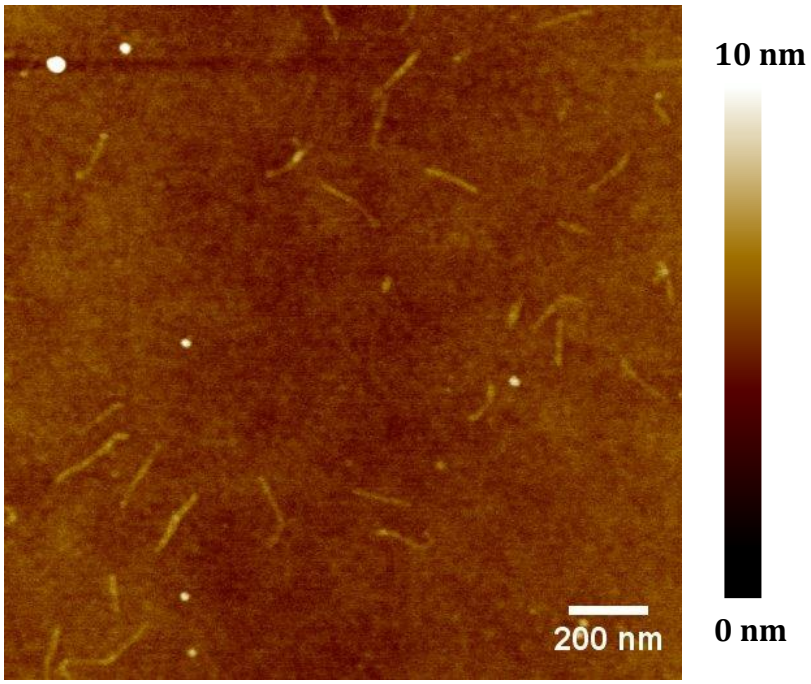

***Figure 34**:Control experiment: AFM topographical image of QD and SWCNT physically mixed with no activating agents: no QDs are present at the terminal ends of the tubes.*

3.2.3 Electronic Coupling in QD-CNT Hybrids

One of the key requirements for an actual device implementation of QD-CNT based hybrid material is the electronic coupling between the two components. The QD-SWCNT hybrid can be regarded as a donor-acceptor system where the interaction between the light and the QDs causes a charge separation in the semiconductor nanoparticles. Energy and charge transfer are both mechanisms involved in the electronic coupling in QD-CNT nanohybrids and the occurrence of one process over the other is strongly dependent on the nature of the interface between the two components in particular on the physical separation between donor and acceptor as well as spectral overlap and energy level alignment of the two components.

Peng et al[146] formed hybrids where QD are covalently attached to carbon nanotubes and demonstrate the prevalence of charge transfer mechanism as the predominant pathway for the deactivation of excited states in QDs. Guldi et al[39] formed hybrids where QDs are attached to carbon nanotubes through electrostatic interactions, providing evidence of partial transfer of charges. In this system the carbon nanotubes provide a quick transportation route of charge carriers to the electrode in a photoelectrochemical cell where QD and CNT serve as excited state electron donor and electron acceptor

respectively. On the other hand, Biju et al[147] observed a reduction of the PL intensity and lifetime of QD conjugated to carbon nanotubes via biotin streptavidin interactions which origin is attributed to Forster resonant energy transfer. Elsewhere, Shafran et al[148] reported an energy transfer process mechanism between a single carbon nanotube attached to an AFM probe which is brought into close proximity to an isolated QD under illumination.

In order to investigate the communication/coupling between the two nanostructures, fluorescence investigations were carried out in solution, monitoring how the stationary and time resolved luminescence of QD is affected when the nanoparticles are attached to the tubes but also on surface with single particle resolution analysing how the QD blinking is affected.

3.2.4 Stationary Photoluminescence

The steady state photoluminescence (PL) emission in isolated QDs and in the hybrid systems was monitored under identical processing conditions see **Figure 35**. We observed a decreased PL intensity for the nanocrystals in the SWCNT-QD hybrid solution, with the PL intensity of the QDs reduced by 48.5% in the nanohybrids compared to the PL of QDs alone, i.e., before conjugation to the nanotubes.

As a control experiment, QDs and CNTs were mixed in the absence of coupling agents, under identical processing conditions and in this case the emission quenching (≈16%) was not as significant as when the QDs and CNTs were combined in the presence of the coupling agents (**Figure 35**). This result implies that the employed coupling strategy gives rise to enhanced emission quenching beyond the quenching caused by physisorption of QDs and CNTs (and/or due to diffusional interactions).

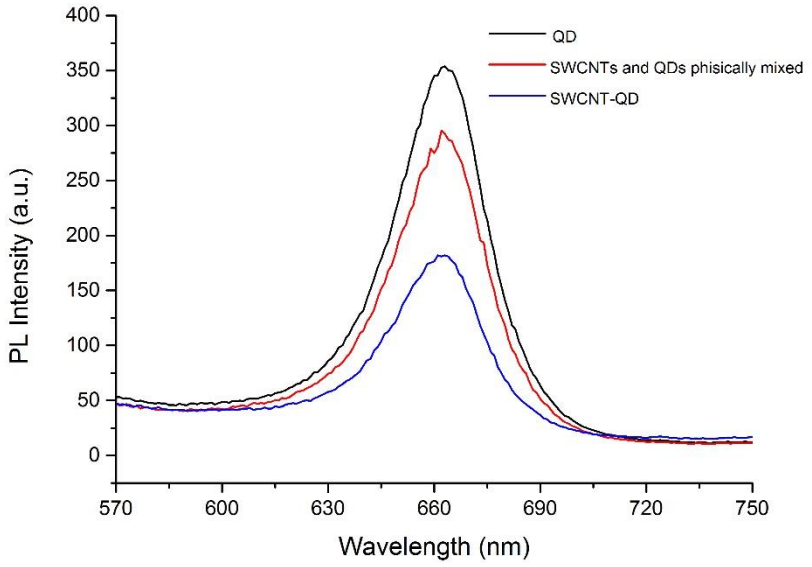

***Figure 35**:Photoluminescence spectra of QDs and SWCNT-QD heterostructure. As a control experiment, QD and CNT were physically mixed with no activating agents at the same concentrations used for hybrids' formation.*

These observations indicate electronic coupling between the two nanostructures forming the hybrids, as previously observed in different SWCNT-QD heterostructures[39,148,146]. As mentioned previously (Chapter 1 Section 1.6), there are two possible external non-radiative relaxation routes for photo-generated excitons in a donor acceptor system, namely resonance energy transfer and charge transfer which can be responsible for the reduction of the overall emission intensity. The decrease in the PL intensity would suggest that efficient charge transfer can be achieved in these nanohybrids as reported by Peng et al[146]. Nevertheless, resonant energy transfer is another possible relaxation pathway that can reduce the overall emission intensity as reported by Pan et al.[149]

3.2.5 Quantum Yield (QY)

Figure 36a shows the Uv-vis spectra of the pristine SWCNT characterized by several peaks which correspond to the different electronic transitions (E_{11}, E_{22} and E_{33}) of tubes of different chiralities (see section 1.2.1), while **Figure 36**b shows the absorbance spectra for pristine QDs and the SWCNT-QD hybrids where it can be noticed that the overall absorbance of the hybrids is higher compared to the pristine QDs as the absorbances of

QD and CNT sum up together in the hybrids sample. When measuring the photoluminescence of the hybrids and estimating the PL quenching part of the incident light can be competitively absorbed by the nanotubes therefore the intensity of the QD photo-luminescence can be reduced with the effect of overestimate the PL quenching. In order to rule out that possibility quantum yield measurements were carried out.

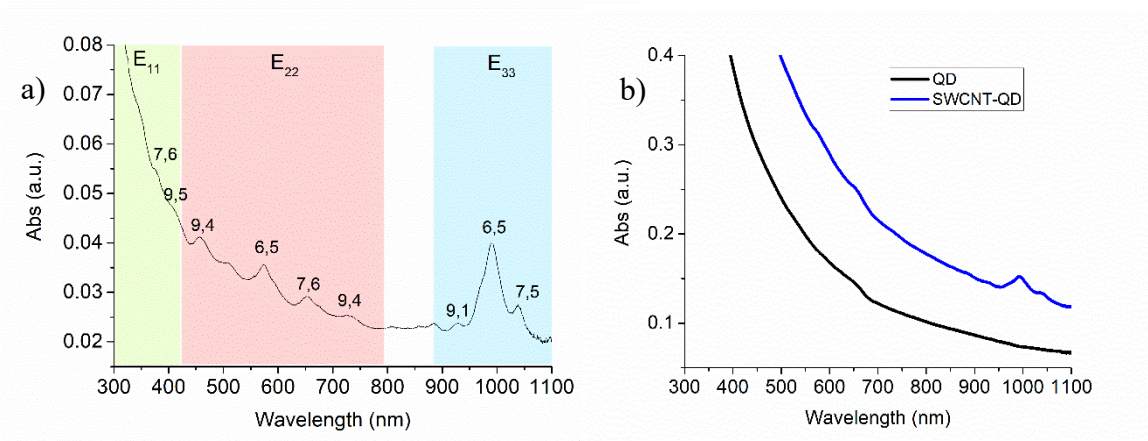

***Figure 36**:a) Uv-vis spectrum of pristine SWCNT, different peaks correspond to the E11, E22 and E33 absorbance peaks of the different tubes chirality present in the sample.*[150] *b) Uv-vis spectra of pristine QD and SWCNT-QD hybrids solutions processed in exactly the same conditions showing the general increased absorbance when QD are mixed with CNT which can potentially lead to overestimate the QD photoluminescence quenching.*

The fluorescence quantum yield (Φ_f) is defined as the ratio between the number of emitted photons ($N_{em}\ (\lambda_{ex})$) and the number of absorbed photons ($N_{abs}\ (\lambda_{ex})$):

$$\Phi_f = \frac{\#\ of\ photons\ emitted}{\#\ of\ photons\ absorbed} = \frac{N_{em}(\lambda_{ex})}{N_{abs}(\lambda_{ex})}$$

And it gives information on the efficiency of a given fluorescence process. Since the physicochemical properties of fluorophores and QDs depend, to a considerable degree, on particle synthesis and surface modification, as well as on the QD environment[110], by comparing the Φ_f values of pristine QDs and the QD-CNT hybrids the emission process of the QD can be further investigated when QDs are tethered to the SWCNT taking into

consideration both absorbance and emission processes at the same time. The calculated quantum yield values resulted: 0.064 ± 0.006 for QDs and 0.010 ± 0.001 for the QD-CNT hybrids, indicating that with the same amount of absorbed photons when the QDs are attached to CNT the number of emitted photons is about six times less than the pristine QDs. This demonstrates that a considerable fraction of excitons in photo-excited QDs attached to the tubes does not recombine within the QD emitting light, but follow different deactivation pathways created by the presence of the CNT (i.e. energy or charge transfer).

3.2.6 Time Resolved Photoluminescence

Since the quenching of stationary photoluminescence and the reduced quantum yields can be ascribed both to energy transfer as well as charge transfer between the excited state of QDs and the electronic states of carbon nanotubes, the decay dynamics of the electronic excitations in our systems was investigated by means of time-resolved photoluminescence (TRPL). PL decays of both core and core/shell quantum dots usually have a biexponential form:[151,152]

$$PL(t) = a_1 e^{-\frac{t}{\tau_1}} + a_2 e^{-\frac{t}{\tau_2}}$$

Where τ_i and a_i represent respectively the lifetime and the amplitude for the two different decays. The shorter lifetime is generally attributed to the intrinsic recombination of initially populated core states while the longer lifetime is commonly attributed to the recombination of electrons and holes on the surface which implies the involvement of surface states.[151] The contributions of the two components to the overall decay are largely influenced by the QD surface properties and in particular by the presence of defects which affect the surface related emission: more and more quenching defects are generated on the surface bigger will be the ratio between the amplitude of the shorter lifetime component to the longer one hence less and less would be the contribution of the longer lifetime to the total PL as demonstrated by photooxidation processes[151] and negative charging of QD surface[153] which have been indeed shown an increase in the proportion of the faster component.

In isolated QDs an emission which follows a biexponential lifetime decay was observed, in good agreement with observations made on similar CdSe nanocrystals[146]. The shorter lifetime (t_1) resulted 1.2 ns, while the longer one (t_2) resulted to be 6.5 ns. In QDs samples, it was found that the surface related emission contributes only 15% of the total PL, while 85% is concentrated in the short lifetime, indicating a prevalence of core emission[146] (**Figure 37**).

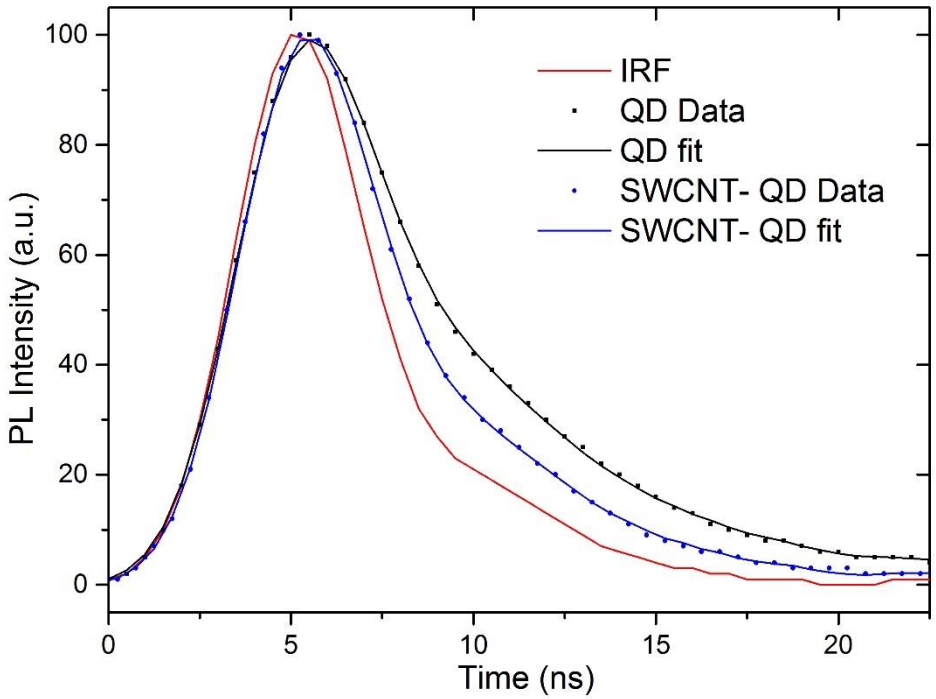

***Figure 37**: Representative normalized time-resolved photoluminescence measurements of QDs (black) and SWCNT-QD nanohybrids (blue).*

In the monofunctionalized SWCNT-QD solutions both the short and the long lifetimes were reduced to t_1 = 0.7 ns and t_2 = 5 ns, respectively, as the presence of the carbon nanotubes is expected to provide additional deactivation channels for the QD excited state with the result of shortening the overall PL lifetime; moreover, the PL followed a near monoexponential decay with more than 95% of emission concentrated on the shorter lifetime. The nearly monoexponential decay is an indication that while the core emission decay is only slightly affected by the presence of the CNT, the surface mediated radiative recombination process is significantly changed. In the presence of charge transfer, considering that the process occurs at short range, the surface states are expected to be

primarily involved. Therefore, the lifetime related to the recombination of surface states should disappear or somehow its amplitude is expected to be reduced, hence the decay changes from a biexponential to a mono or nearly-mono exponential decay. Energy transfer, on the other hand, is a long-range process and is expected to equally affect both core and surface states.

The presence of a near-monoexponential decay with the reduction in the amplitude of the emission kinetics indicates the electronic interaction between the QD and SWCNT is dominated by a surface-mediated charge transfer process rather than a resonance energy transfer deactivation route, as previously demonstrated on similar systems.[146] These findings further validate the occurrence of electronic coupling, with charge transfer being more likely than energy transfer to be the dominating process, also in view of the relatively short linker (2 carbon atoms chain) employed to bridge the CNTs and the nanocrystals in the monofunctionalised nanohybrids.

3.2.7 Single Molecule Photoluminescence (Blinking)

To further monitor the electronic coupling, but with single-particle resolution, low-coverage films were cast on glass substrates to obtain physisorbed structures spaced at least 1 μm apart, hence optically resolvable which allowed us to perform PL studies of individual heterostructures on surfaces (**Figure 38**).

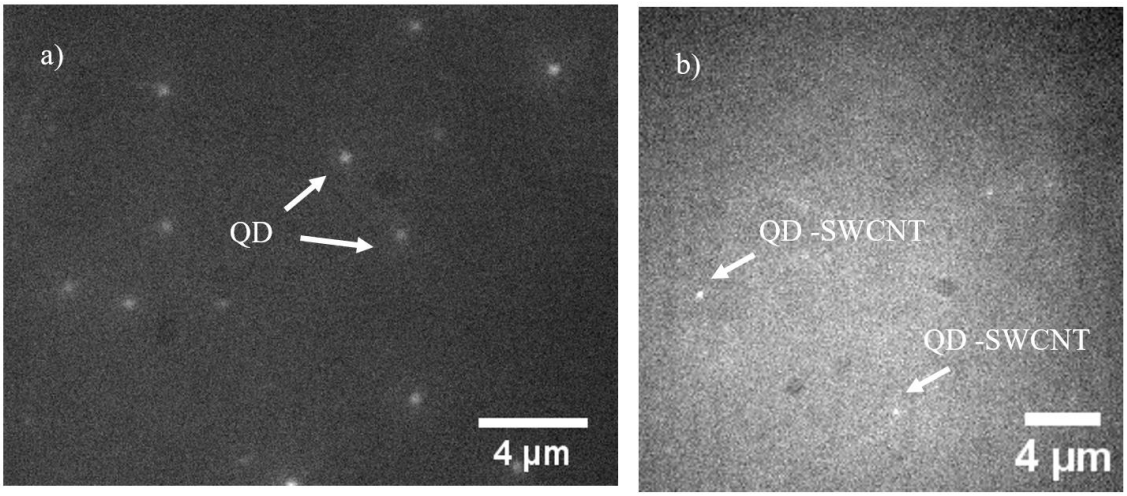

***Figure 38**: Representative image frames taken from the movies used to study the PL blinking of QDs (a) and SWCNT-QD heterostructures (b).*

QDs have been shown to be characterized by quantized and intermittent emission—random switching between states of high (ON) and low (OFF) emissivities (blinking) which is generally indicative of single emitter. **Figure 39** shows representative blinking traces for single pristine QD and hybrids providing evidence of how the QD blinking is affected in the hybrids: pristine single QDs exhibit a fast switching between ON and OFF states (**Figure 39**a), while the QD-SWCNT hybrids show longer OFF periods (**Figure 39**b). This is also confirmed by the plots of the occurrence of the PL intensity of the single traces where in the case of the pristine QD the intensities are distributed equally between low or no intensity (OFF) and high intensity (ON) (**Figure 39**c) while in the case of the hybrids the bimodal distribution shows a prevalence of intensities centred at a low value corresponding to the OFF states (**Figure 39**d). The reduction of the blinking indicates that in the hybrids the rate of the deactivation processes of the excited state is comparable to the intrinsic decay of the excited state of pristine QDs: the CNTs hamper the exciton recombination leaving the QDs in a charged state for longer periods.[148,97,96]

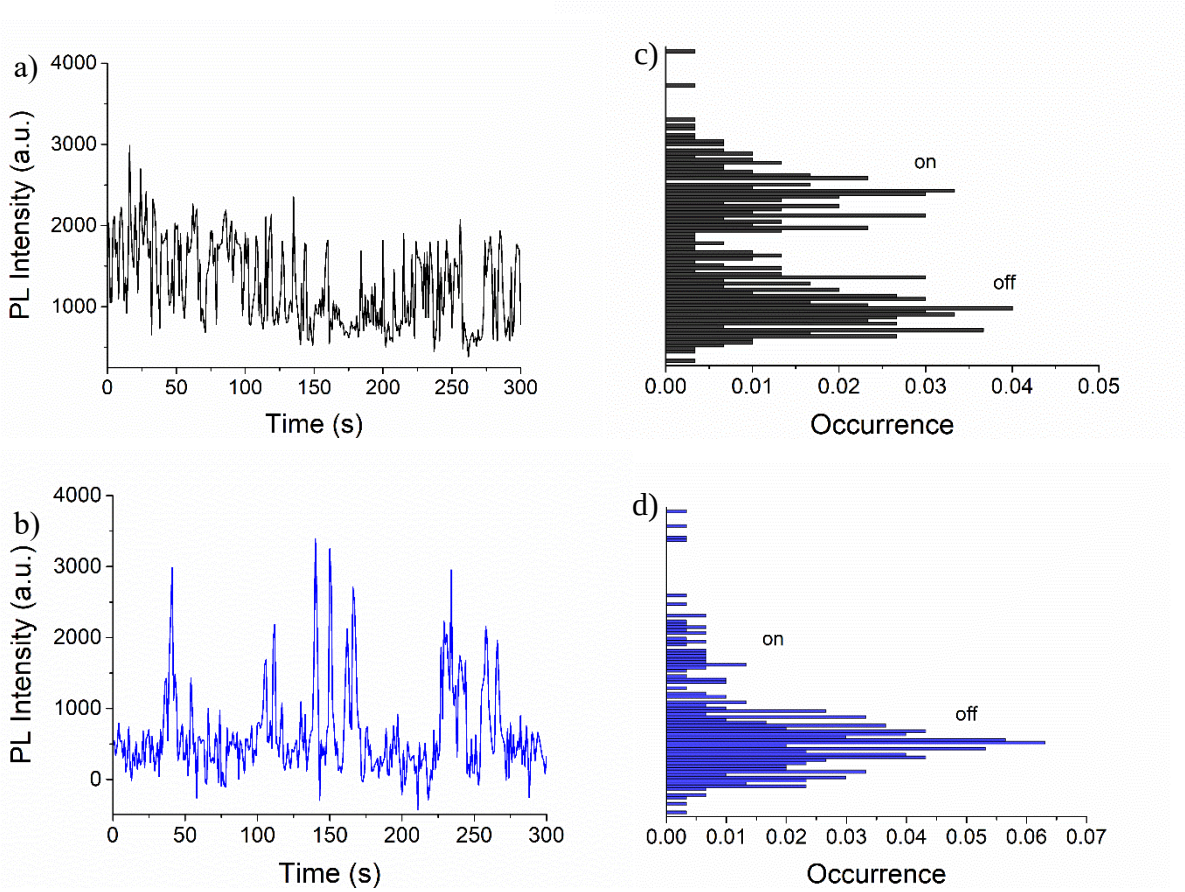

***Figure 39**: Representative single particles luminescence traces and intensity histograms of a), c) single quantum dots and b), d) individual monofunctionalized SWCNT-QD structures.*

An intensity threshold was set to distinguish between ON and OFF states (**Figure 40**) and this allowed to generate a probability distribution of the off states P_{off} (see methods for more details) which have been previously shown to exhibit a power law distribution with a typical exponent between ≈1.5 to ≈1.7 at room temperature.[154,155] The OFF times were chosen to characterise the hybrids at the single-molecule level and not the ON times, because OFF times have been found to be less affected by changing the exposure time on the microscope.[156]

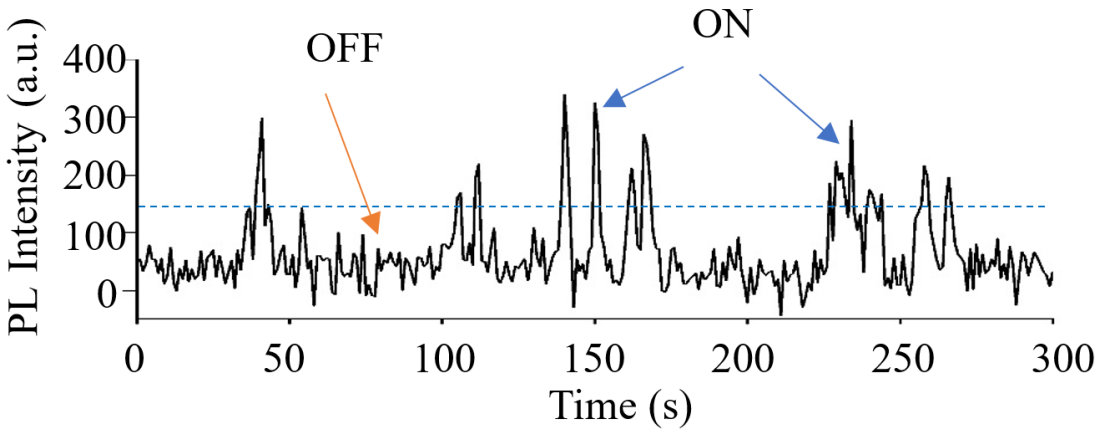

***Figure 40**: A threshold (red dashed line) is chosen to discriminate between OFF and ON states.*

By accumulating data for over 40 individual QD and CNT-QD a probability distribution for each sample was generated, as shown in **Figure 41**, obtaining a power-law dependence amongst two decades in both probability and OFF-period for isolated QDs and single QD-SWCNT heterostructures with an average exponent of ≈−1.77 and ≈−1.35, respectively.

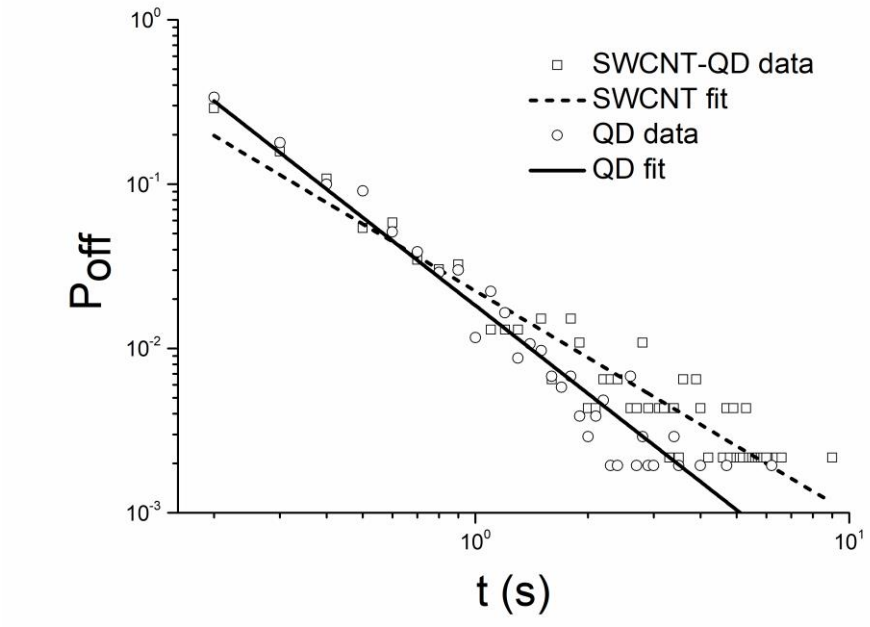

Figure 41*: Normalized probability distributions of the PL off periods, and accompanying fits, for QD-SWCNT nanohybrids and QDs.*

The exponent obtained for single QDs is in good agreement with literature values,[154,155] while the smaller exponent observed in the case of QDs coupled to CNTs (in the hybrids) is evidence for the increased probability densities of the OFF events (**Figure 41**) indicating that in the hybrids the quantum dots have a higher probability to stay in the OFF, charged states for longer periods. These findings are consistent with similar behaviour previously observed in heterostructures of multiple QDs conjugated to electron acceptor systems such as TiO_2 nanoparticles or fullerenes, attributed to a charge transfer process.[157–159]

3.2.8 Surface Modification of QDs

The reaction between the amino groups on the QD with the carboxyl groups at the end of nanotubes generate amide groups on the QD surface changing the chemical nature of the surface itself. This could potentially be responsible for the different blinking observed in the hybrids compared to the pristine QDs as the optical properties of QDs are strongly influenced by the surface characteristic and chemical nature. In order to rule out this possibility, as a control experiment, the amino terminated QDs were reacted with butyric

acid via amidation reaction generating amide groups on the surface hence obtaining the same chemical groups as in the hybrids (**Figure 42**).

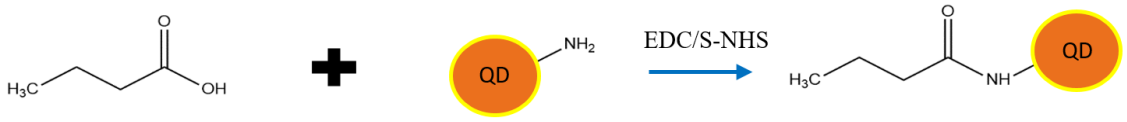

***Figure 42**: Reaction scheme for the functionalization of amino terminated QD with butyric acid through EDC/S-NHS coupling reaction.*

The successful covalent functionalization was monitored via FTIR spectroscopy, as shown in **Figure 43**: the butyric acid (trace a **Figure 43**) exhibits peaks at 1212 cm^{-1} attributed to C-O stretch, 1711 cm^{-1} attributed to C=O stretch, and 2975, 2940 cm^{-1} attributed to C-H stretching bands while the amino terminated QD (trace b **Figure 43**) exhibits peak at 1603 cm^{-1} attributed to NH_2 bending mode. QDs functionalized with butyric acid (trace c **Figure 43**) exhibits two peaks at 2918 and 2850 cm^{-1} (C-H stretching bands) which provide clear indication that butyric acid was incorporated onto the surface of the QDs and a broad peak at 1624 cm^{-1} which can be attributed to vibrational modes characteristic of amides groups.

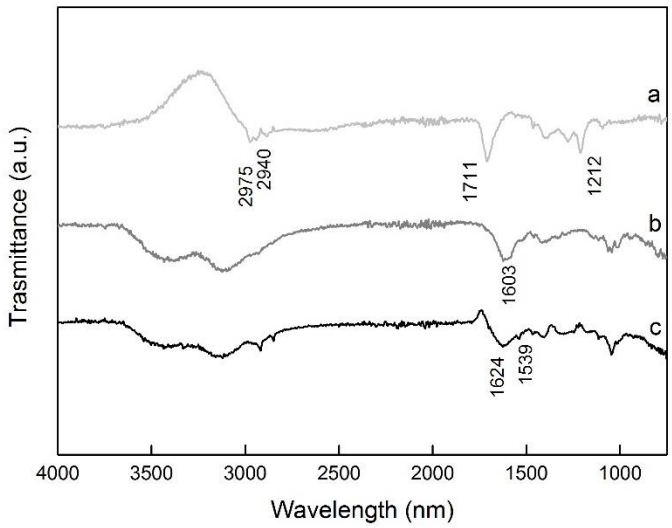

***Figure 43**: Infrared spectra of the butyric acid (trace a), the amino terminated QD (trace b) exhibits peak at 1603 cm^{-1} (NH_2 bending mode) and QDs functionalized with butyric acid (trace c).*

The same blinking analysis was carried out for the QDs functionalized with butyric acid, shown in **Figure 44**, and the blinking behaviour was found in line with the pristine QD as can been noticed from both the PL traces (**Figure 44**a), the occurrence of the intensities (**Figure 44**b) for single traces, as well as, for the accumulated probability distribution of the OFF states (**Figure 45**) with a slope of 1.66 for QD functionalized with butyric acid. This provides further evidence that it is actually the presence of CNT to affect the blinking behaviour of the QD and not the different chemical groups on QD surface resulted from the amidation reaction.

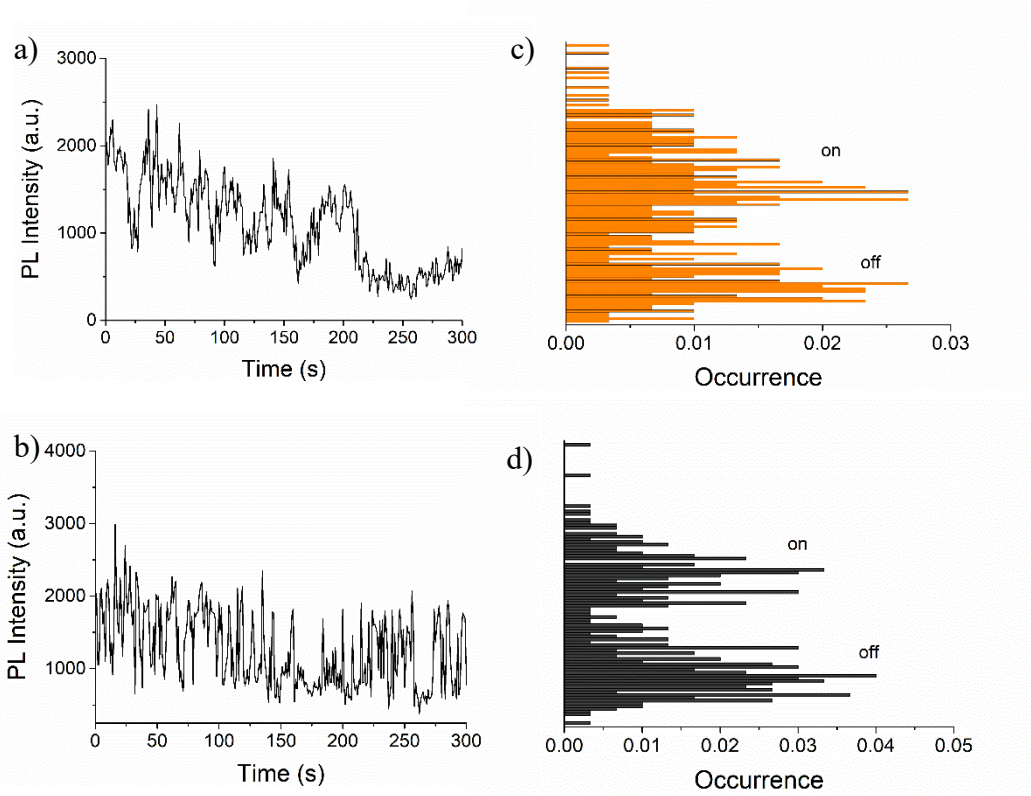

***Figure 44**: Representative luminescence trace of QDs functionalized with butyric acid (a) and pristine QDs (b), and corresponding intensity histogram (c)and (d).*

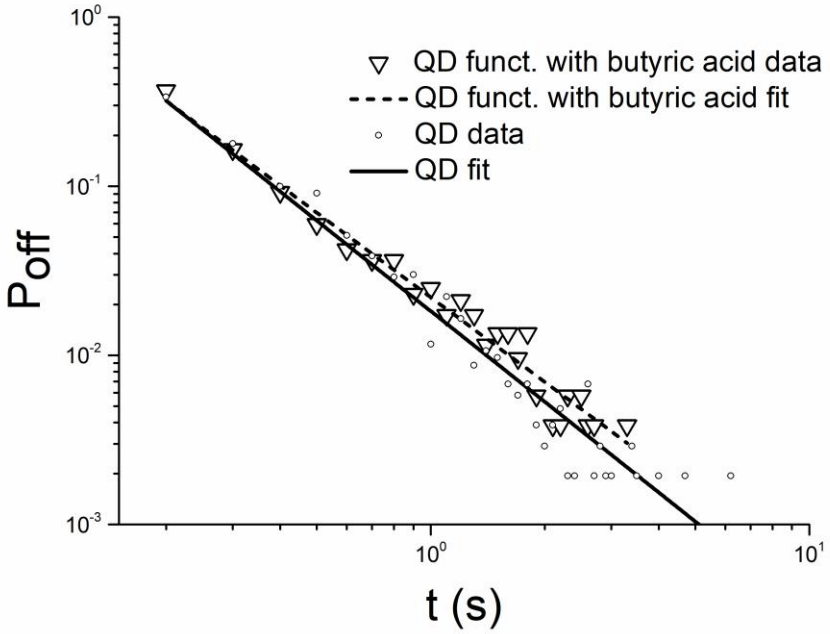

Figure 45*: Plots of the probability distributions of the off periods for QDs functionalized with butyric acid (orange) and pristine amino terminated QDs (black).*

3.3 Conclusions

In conclusion, a facile and green assembly strategy was presented for the formation of SWCNT-QD heterostructures with single-particle control, in aqueous solution. QDs were selectively and covalently linked to the terminal ends of DNA-wrapped SWCNTs, maximizing the formation of monofunctionalized SWCNT-QD structures. Photoluminescence studies were performed both in solution (stationary and time-resolved) and on surfaces at the single nanohybrid level, showing evidence of electronic coupling between the two nanomoieties. This is the first example of controlled in-solution assembly—with evidence of coupling at the single particle level—of nanohybrids consisting of single QDs linked to individual SWCNTs. The knowledge developed makes a significant contribution to the fabrication of nanohybrid materials with single-particle control, an important feature in the design of novel QD-based optoelectronic and light-energy conversion devices.

Future challenges will involve understanding, in more details, the electronic coupling in the hybrids and optimize the structure in order to favour electron transfer over energy transfer process, as only the former results in possible applications of the hybrids in

energy store/conversion devices. In order to achieve that, taking advantage of the level of control demonstrated here, in the following chapter the tunability of the electronic coupling at the organic–inorganic interface is further investigated, e.g., via the use of ligands of different length and chemical nature, bridging the QDs and the CNTs in the hybrids. This would allow to highlight the importance of the mechanisms involved at the interface, such us distant depend effects, showing how the linkers employed play a key role in the QD-CNT electronic coupling.

4 CNT-QD HYBRIDS USING DIFFERENT BRIDGING LINKERS

4.1 Introduction

As discussed in the previous chapter, it was possible to control the position of single QDs in QD-CNT nanohybrids, where the nanoparticles are selectively attached to the terminal ends of the SWCNTs. This single-molecule control over the formation of nanohybrids is of uttermost importance in terms of both the exact position of the QD onto the nanoelectrode, and the nanoparticle-electrode separation, as small changes in the organization of the individual nanomoieties forming such hybrids can have a major impact on the coupling between the different components.[160–162]

A further step towards the understanding of these nanostructures with nanoscale accuracy is the optimization of the electronic coupling taking place between the QD and the carbon nanotube; this would allow the control over the energy and charge transfer processes which are the competing mechanisms involved in the deactivation of the excited states of QDs in the aforementioned heterostructures. This goal can be achieved by employing selected linkers to bridge QDs and CNTs, allowing the tuning of the length as well as the chemical nature of the bridging component, to ultimately control the electronic coupling.

Different nanomoieties, from metal and semiconducting nanoparticles/nanorods[163–171] to biological (macro)molecules as protein and nucleic acids,[172–176] have been coupled to functional carbon nanostructures. Many of the strategies pursued are non-specific in terms of attachment sites and lack single-molecule control over the number of nanocrystals per hybrid and distance between the nanomoiety and the carbon nanostructure, resulting in an uncontrolled electronic coupling between the nanohybrid components. In particular, even if dimensionality effects have been investigated at the nanoscale[177–179] and with single-molecule resolution,[180–182] challenges remain in precisely controlling the nanoscale distance between the two components hampering their potential implementation into actual devices.

In this chapter it is present the controlled formation of single-molecule QD-CNT heterostructures, assembled employing a similar chemical strategy presented in Chapter 3, but the spacing between single quantum dots attached to the terminal ends of individual carbon nanotubes is controlled and tuned through different molecules (aromatic molecules, alkyl chains, and dsDNA) employed as molecular rulers. This strategy allowed us to tune the length as well as the chemical nature of the bridging molecule resulting in a greater control over the electronic coupling (energy and/or charge transfer) between QDs and SWCNTs in monofunctionalised heterostructures.

4.2 Conjugated Linkers

In order to study how the nature of the linker can affect the electronic coupling in the QD-CNT nanohybrids, three different conjugated molecules were employed containing 1,2 and 3 phenyl rings to bridge the two moieties. The linkers employed and a schematic of the QD-SWCNT nanohybrids with conjugated linkers, which in all cases are diamine linkers, are shown in **Figure 46**.

4.2.1 Assembly

The SWCNTs used underwent a mild acid treatment, followed by dispersion in aqueous solution via DNA wrapping; the SWCNTs were subsequently separated by size exclusion chromatography. As previously described in Chapter 3 the DNA further protects the side wall of the nanotubes leaving only the terminal ends available for functionalization. The strategy developed to assemble these hybrids is very similar to the one described in Chapter 3 for the tethering of amino functionalized QD to the terminal ends of SWCNT (**Figure 27**). Figure 46 describes the schematic of assembly strategy: It involves the formation of an amide bond, through EDC/S-NHS coupling, between the COOH groups on the SWCNT and one of the terminal amine groups of each linker. In order to avoid crosslinking between CNTs, a great excess of linkers was used for each reaction, and the excess was later removed through dialysis. Once the CNT were functionalized with the amine linkers they were allowed to react with EDC/S-NHS activated COOH functionalized quantum dots. In summary this procedure allows the formation of two amide bonds: one between the diamine linker and the COOH group on the CNT, and the other one between the COOH on the quantum dot and the diamine linker. After reaction

with the activated QDs, the hybrids solutions were further dialyzed in order to remove the excess of unreacted EDC and S-NHS. This step was found to be essential as the reaming COOH groups on the QD surface may be still exposed to the EDC and S-NHS which deeply influence the QD surface and hence the QD optical properties compromising any photo-physical characterization.

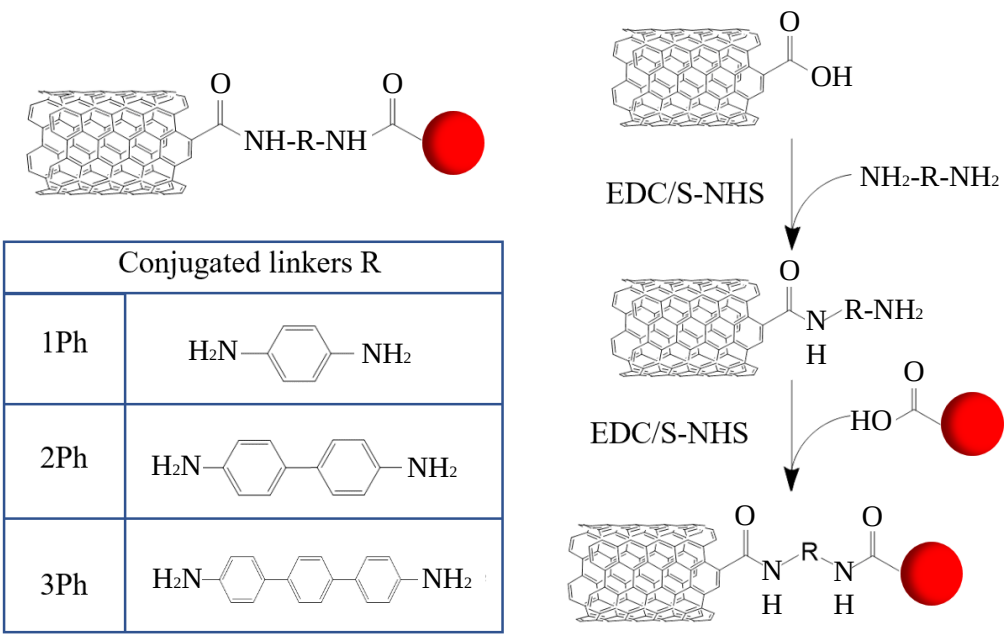

Conjugated linkers R	
1Ph	H_2N—⟨⟩—NH_2
2Ph	H_2N—⟨⟩—⟨⟩—NH_2
3Ph	H_2N—⟨⟩—⟨⟩—⟨⟩—NH_2

***Figure 46**: a) schematic of the CNT-linkers-hybrids. b) schematic of the EDC/S-NHS mediated coupling for the formation of the CNT-linkers-hybrids. The table shows the chemical structures of the linkers employed.*

The formation of the hybrids was monitored by casting diluted solutions on mica and imaging them through atomic force microscopy (AFM). **Figure 47** shows topography AFM images of the CNT-QD hybrids where QDs are selectively linked to the terminal ends of SWCTNs. The yields of formation of the SWCNT-QD nanohybrids, as measured by AFM, were found to be very low (less than 5%); this is most likely due to the fact that two coupling reactions are involved thus lowering the total yield of attachment.

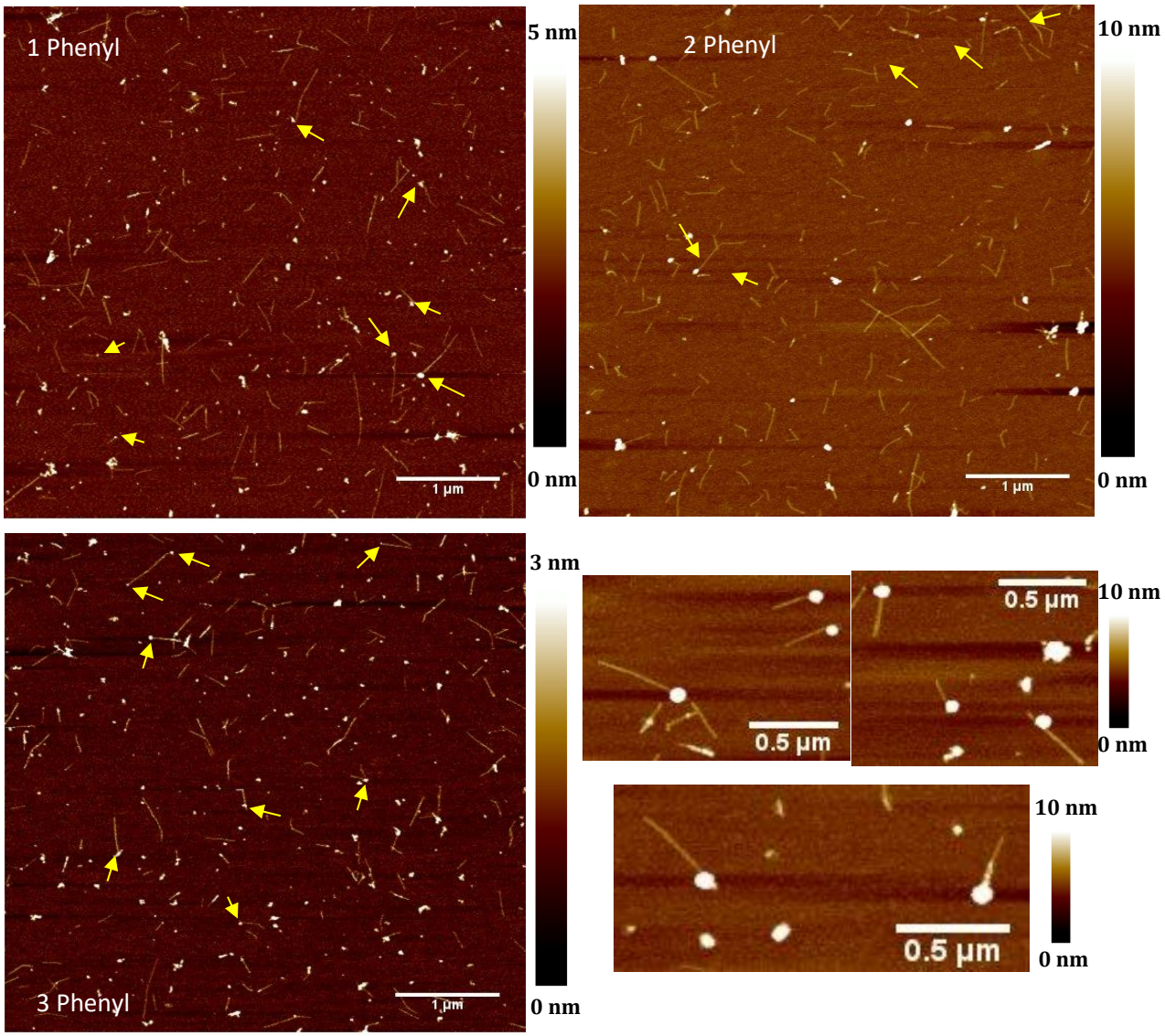

***Figure 47**: Typical topography AFM images of the nanohybrids assembled using 1Ph, 2Ph and 3Ph linkers.*

Figure 48 shows a topography AFM image of pristine carboxylated quantum dots employed in the hybrids formation with the corresponding profile section for four different dots. In this case carboxylated CdTe core QDs were employed with sizes ranging between 3 and 6 nm.

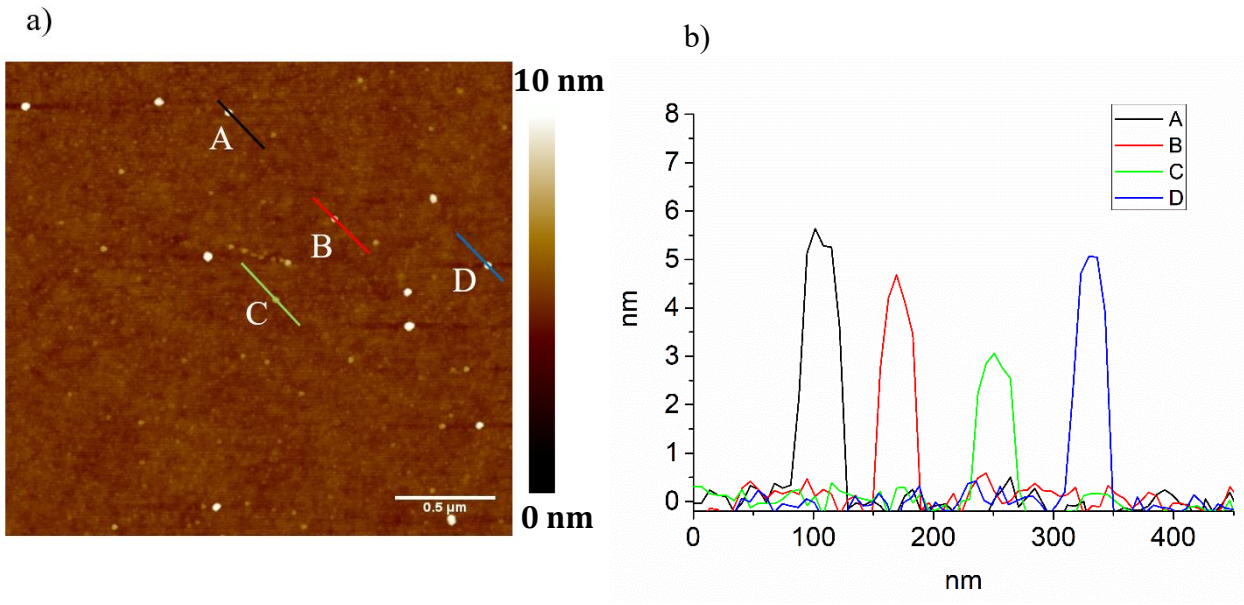

Figure 48*: a) AFM topographical image of pristine carboxyl terminated CdTe core QDs. b) height profiles of the lines drawn in figure a) for four different QDs.*

4.2.2 Stationary Photoluminescence

In the case of the CNT-conjugated linker-QD hybrids no significant variations in PL intensities could be observed compared to the pristine QDs and among the hybrids. This is because after the assembly of the hybrids a final dialysis step is required to eliminate the free unreacted EDC and S-NHS with consequent difficulties in keeping constant volumes and hence equal QD concentrations in all samples. This did not allow to carry out comparative quantitative analysis of the PL intensities. Moreover, lower (5%) yields of hybrids formation were obtained and this resulted in small and not fully reliable interpretation of the PL changes observed among all the samples investigated.

4.2.3 Time Resolved Photoluminescence

Differently from stationary PL measurements, a qualitative analysis of the shape of the QDs emission decay through Time-resolved photoluminescence (TRPL) investigations allowed to study the decay dynamics of the exited states of QDs in our heterostructures. **Figure 49** shows the decay traces of the pristine QDs as well as those for the hybrids with 1, 2 and 3 phenyl rings. The fitting parameters are shown in **Table 1**.

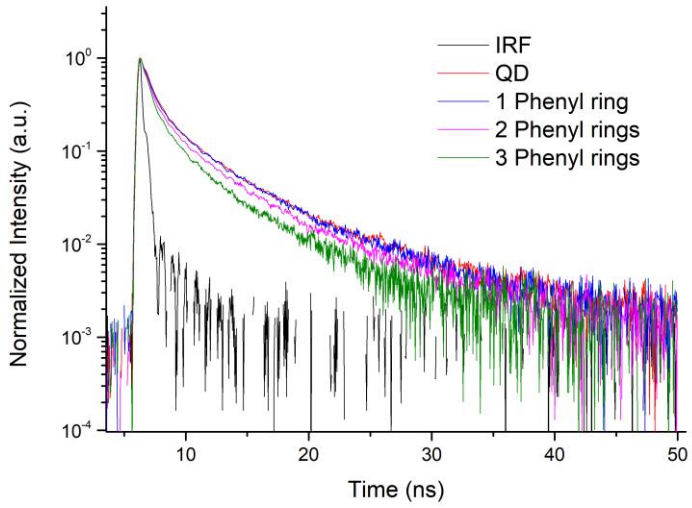

***Figure 49**: Normalized time-resolved photoluminescence measurements of pristine QD and CNT-QD hybrids using 1Ph, 2Ph and 3Ph linkers. Experimental kinetics have been fitted with a biexponential decay law, taking into account the effect of the measured instrumental response function (IRF, in black) through a deconvolution. The fitting parameters are shown in the table on right.*

Sample	a_1	t_1	t_2
QD	0.763 ±0.006	0.809 ±0.008	4.97 ±0.05
1 phenyl ring	0.763 ±0.003	0.604 ±0.008	4.35 ±0.04
2 phenyl rings	0.776 ±0.002	0.557 ±0.007	4.01 ±0.04
3 phenyl rings	0.804 ±0.003	0.481 ±0.007	3.37 ±0.04

***Table 1**: Fitting parameters for the Time resolved photoluminescence data using a biexponential decay for the 1, 2, 3 phenyl rings hybrids.*

A gradual shortening of both the shorter and longer lifetimes was observed with increasing number of phenyl rings, but regardless of the linker used, the PL traces followed a similar biexponential decay with 76 % concentrated in the shorter lifetime. These findings would suggest that, on the one hand, the nature of the linker affects the electronic coupling, since a progressive reduction of lifetimes is observed when the number of phenyl rings increases and hence with the increasing degree of conjugation and length of the linker; however, on the other hand, it is not possible to draw any

definitive conclusions on the nature of this coupling: charge transfer does not seem to be the mechanism responsible for the progressive shortening of the lifetimes as in this case it would have been expected a behaviour similar to the one described in Chapter 3, where the PL followed a near monoexponential decay. Moreover, energy transfer process is expected to be more effective at shorter distances, hence it would have been expected the opposite trend to the one observed.

As a control experiment, QDs were mixed with carbon nanotubes without any linkers; the PL decay in this case was found to be very similar to the one for pristine QDs (**Figure 50** and **Table 2**), confirming that it is the presence of the linkers bridging the two components responsible for the different PL decays in the hybrids. In all cases the PL decay was found to be affected by the linker compared to the pristine QDs and the solution where QD and CNT were physically mixed. Nevertheless, no fully reliable comparisons were possible among the linkers. An explanation for the impossibility to investigate the effects of the nature of the linker on the CNT-QD electronic coupling can be the low yield of the reaction and the presence of free, unreacted QD in solution which smoothed out any possible differences.

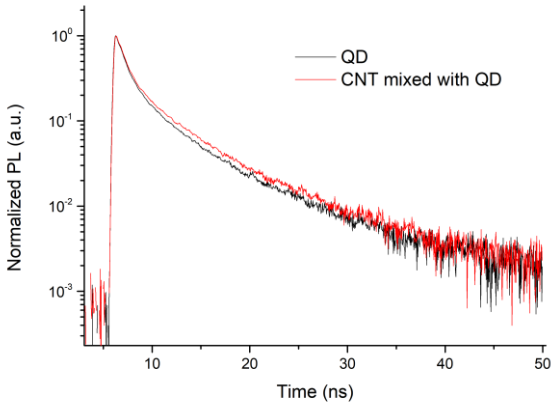

***Figure 50**: Normalized time-resolved photoluminescence measurements of pristine QD and CNT and QD physically mixed. Experimental kinetics have been fitted with a biexponential decay law, taking into account the effect of the measured instrumental response function (not shown) through a deconvolution. The fitting parameters are shown in the table on right.*

Sample	a_1	t_1	t_2
QD	0.763 ± 0.004	0.707 ± 0.001	4.93 ± 0.07
QD mixed with CNT	0.751 ± 0.002	0.729 ± 0.008	5.06 ± 0.04

***Table 2**: Fitting parameters for the Time resolved photoluminescence data using a biexponential decay for pristine QD (black) and QD phisically mixed with CNT (red).*

4.2.4 Single Molecule Photoluminescence Investigations (blinking)

To further monitor the electronic coupling with single-particle resolution, single-molecule measurements were performed as previously described in Section 3.2.7. PL blinking analysis was carried out for the 1 phenyl, 2 phenyl, 3 phenyl rings linkers hybrids as shown in ***Figure 51*** but no relevant differences were found in the distribution of the OFF states (see table in ***Figure 51***).

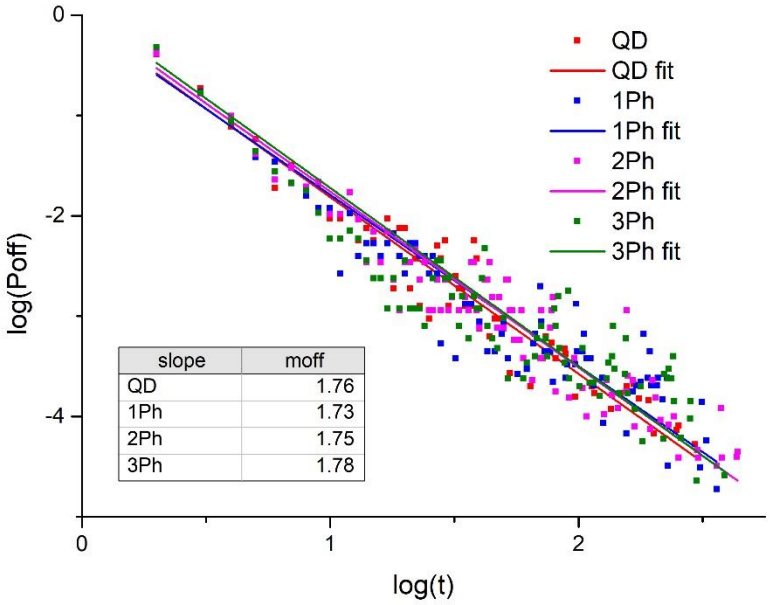

Figure 51*: Normalized probability distributions of the PL off periods, and accompanying fits, for QD-SWCNT nanohybrids with the different linkers employed.*

As stated earlier for the TRPL data, an explanation for the lack of significant differences can be ascribed to the low reaction yield which made impossible to discriminate the effect of the different linkers on the electronic coupling.

4.2.5 Alkyl chains Linkers

As control experiments, using the same assembly strategy described in Section 4.2.1, different alkyl chains linkers (**Table 3**) were used for the hybrids formation. These linkers are characterized by essentially the same electronic properties and the only difference among the series is the number of carbon atoms that constitutes the carbon chain. The formation of the hybrids was monitored via AFM, as shown in **Figure 52**, and also in this case low yield of hybrids formation was observed (less than 5 %).

	Alkyl chain linkers
6C	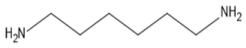
8C	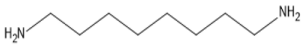
10C	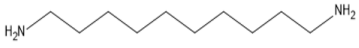
12C	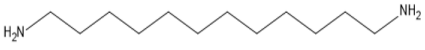

***Table 3**: Chemical structures of the alkyl chains linkers.*

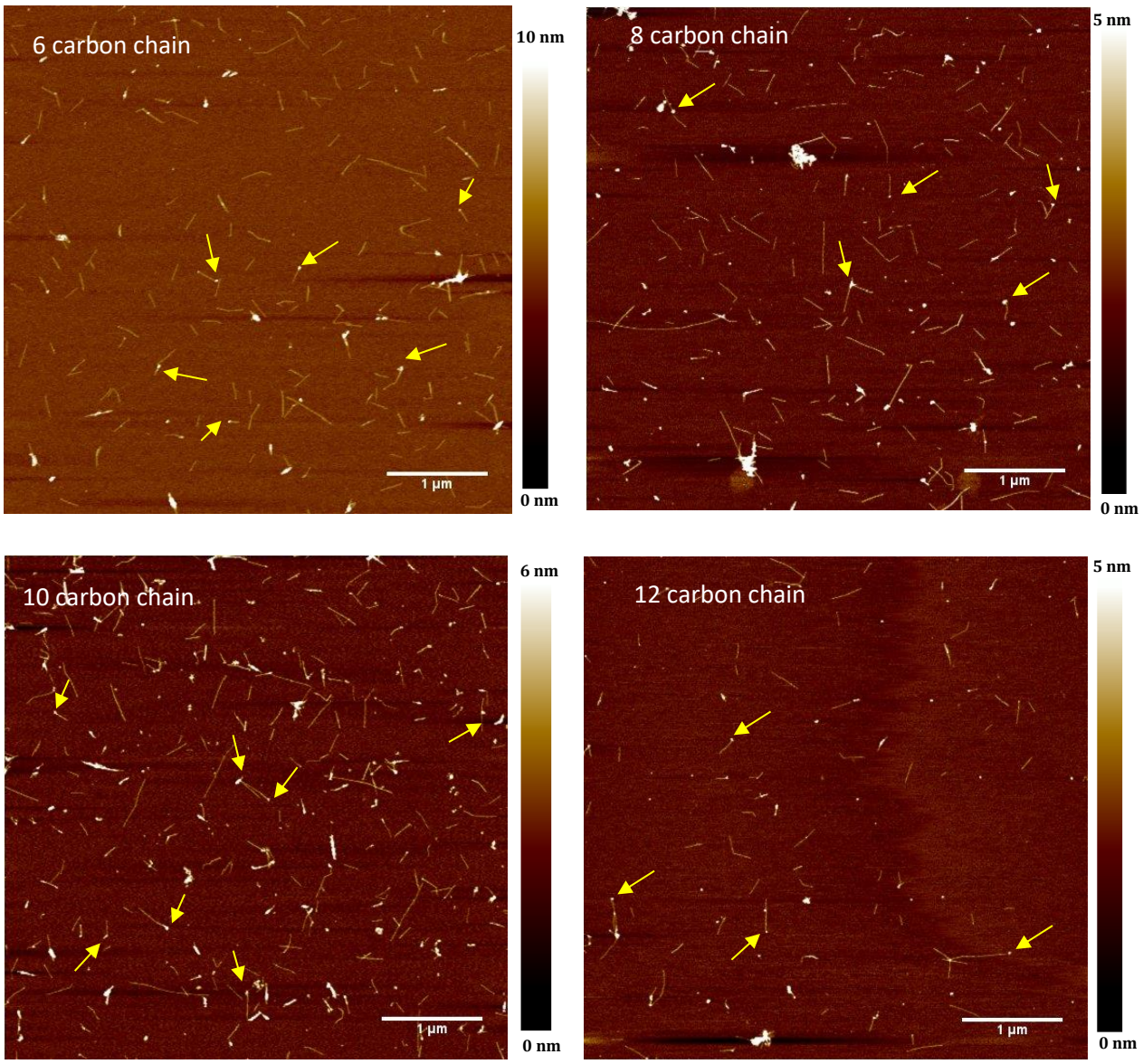

***Figure 52**: Typical topography AFM images of the nanohybrids assembled using 6C, 8C, 10C and 12C linkers.*

Time resolved measurements were carried out for the hybrids with 6, 8, 10 and 12 carbon alkyl chain, as shown in **Figure 53** for decay traces and **Table 4** for the fitting parameters. A small shortening of both lifetimes was observed for all the hybrids compared to the pristine QDs, but no substantial differences were measured among the linkers series for all cases. This shows that, independently by the linker employed, the decay follows the same biexponential trend with both lifetimes reduced equally for all linkers. This result suggests that the decay of the QDs in the hybrids is definitely affected by the presence of the attached CNT through the linkers, but it was not possible to discriminate the effect of each linker of different length on the QD-CNT electronic coupling. As stated in the

previous sections (4.2.3 and 4.2.4) this is most likely due to the low yield of the reaction as well as to the presence of free, unreacted QDs which suppressed the possibility to observe any differences.

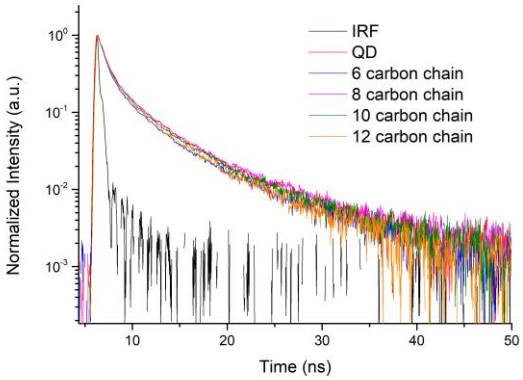

***Figure 53**: Normalized time-resolved photoluminescence measurements of pristine QD and CNT-QD hybrids using 6C, 8C, 10C and 12C linkers. Experimental kinetics have been fitted with a biexponential decay law, taking into account the effect of the measured instrumental response function (IRF, in black) through a deconvolution. The fitting parameters are shown in the table on right.*

Sample	a_1	t_1	t_2
QD	0.763 ± 0.006	0.809 ± 0.008	4.97 ± 0.05
6 carbon chain (6C)	0.760 ± 0.003	0.667 ± 0.008	4.64 ± 0.04
8 carbon chain (8C)	0.776 ± 0.003	0.667 ± 0.001	4.01 ± 0.05
10 carbon chain (10C)	0.773 ± 0.003	0.645 ± 0.008	4.42 ± 0.05
12 carbon chain (12C)	0.770 ± 0.003	0.616 ± 0.008	4.11 ± 0.04

***Table 4**: Fitting parameters for the Time resolved photoluminescence data using a biexponential decay for the hybrids with alkyl chains linkers.*

4.2.6 Stationary Photoluminescence of CNT

SSPL studies were carried out on the SWCNTs for each nanohybrid, as well as for the pristine nanotubes (**Figure 54**). The different peaks correspond to the different chiralities of the tubes in solution:

-1044 nm correspond to 6,5 chirality

-1080 nm correspond to 7,5 chirality

-1142 nm correspond to 7,6 chirality

-1274 nm correspond to 9,5 chirality

No significant variations in emission were observed between the nanotubes in the hybrids and the pristine SWCNTs, with only small difference in intensities which are most likely do to slightly different concentrations of the nanotubes. This is likely due to the high specificity of our functionalization, where single QDs are only tethered to the ends of the nanotubes, hence the electronic structure of the SWCNTs is preserved, with only local changes potentially occurring at the site of QDs attachment.

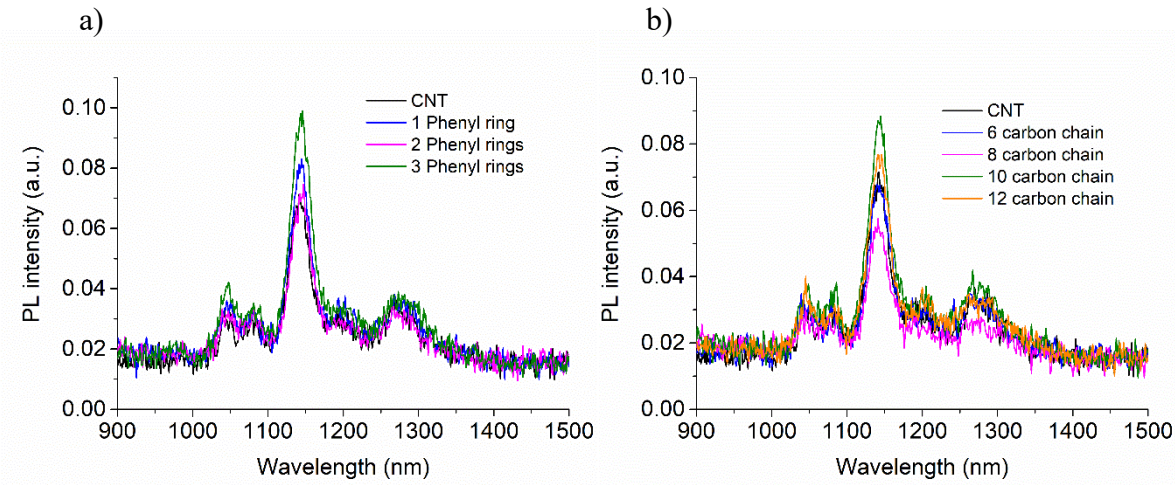

***Figure 54**: Photoluminescence spectra of pristine SWCNT and SWCNT-linkers-QD hybrids.*

4.3 DNA as a molecular ruler

A bio-inspired approach was pursued via the use of DNA as the linking moiety between CNT and QDs, due to its demonstrated ability to chemically program the assembly of nanoparticle-based materials.[183,184,193–195,185–192] DNA sequences with specific functionalities and length are commercially available and provide a facile system for varying the distance between the two components in a controlled fashion at a sub-nanometre scale. In particular, the number of bases in a double stranded (ds)DNA was altered, in order to regulate the distance between a SWCNT and a QD in 1:1 nanohybrids, where the DNA acts as a molecular ruler tuning the coupling between the two nanostructures with single-molecule control. The work presented here (paragraph 4.3) has been carried out in collaboration with Dr Mark Freeley, who carried out the assembly and the atomic force microscopy characterization. My contribution includes the photoluminescence measurements and the blinking analysis.

4.3.1 Assembly

In these hybrids the DNA plays a double function: it acts as a protecting agent towards the functionalization along the sidewalls but it is also employed as a molecular bridge to link QD and CNT. A heterobifunctional dsDNA containing a biotin at one end and an amino group at the opposite end was tethered to the carboxylic groups on the SWCNT termini via a amidation reaction (**Figure 55**). This effectively resulted in SWCNTs exhibiting biotin-terminating dsDNA at their end.

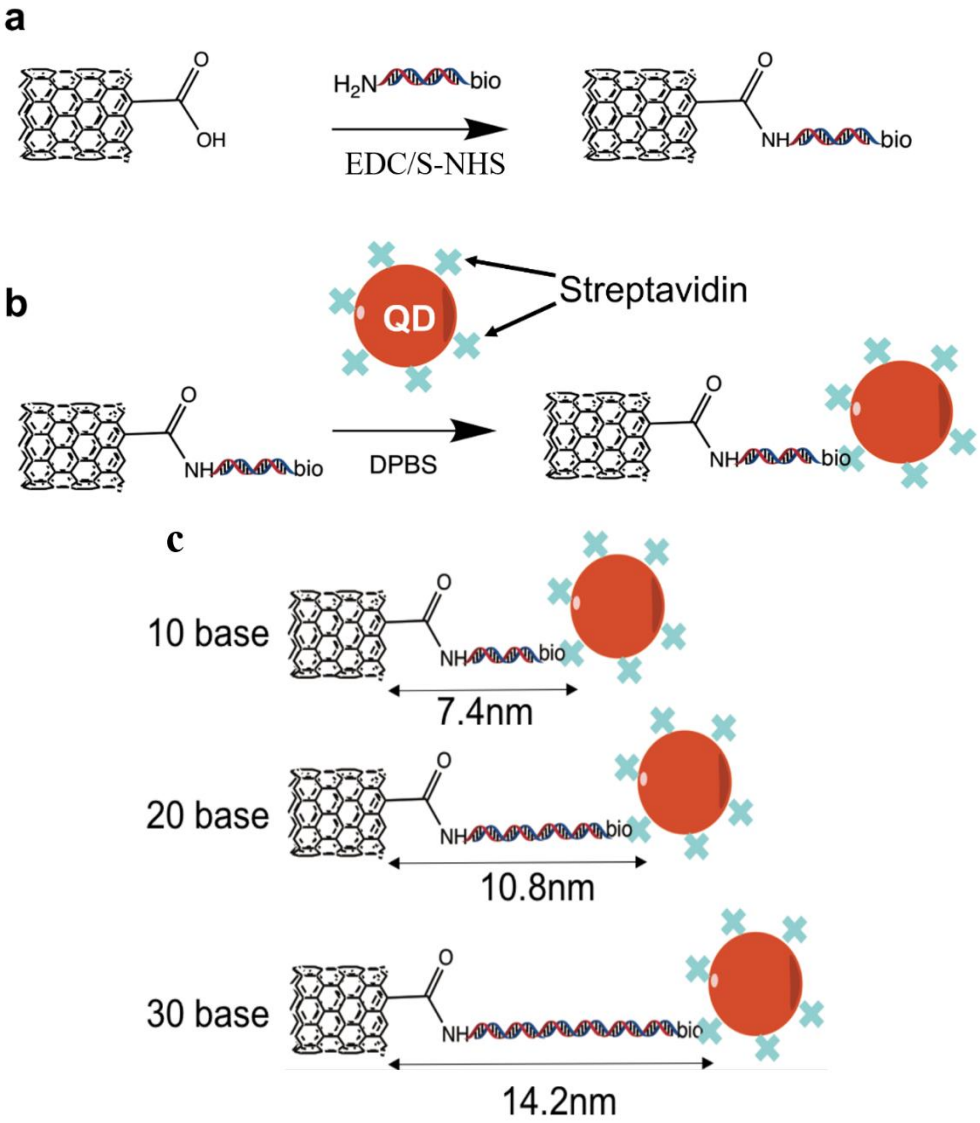

***Figure 55**: Scheme for the conjugation of dsDNA to SWCNTs via an amidation Reaction (a), and attachment of a QD to a DNA-modified SWCNT via the biotin-streptavidin Interaction (b). Schematic representation of the SWCNT-QD hybrids with 10 bp, 20 bp, and 30 bp linkers and related distances (c).*

Streptavidin-QD conjugates were then anchored to the SWCNTs biotin termini via biotin-avidin recognition[196] directly in solution. Biotin-streptavidin interactions are commonly used in molecular biology and biotechnology as this interaction is one of the strongest non covalent biological interaction, having a dissociation constant in the order of 4×10^{-14} M,[197] highly specific and stable towards temperature and pH changes and occurs in relatively short time.

Different duplexes were employed, namely 10, 20 and 30 base pair, which allow to precisely control the distance between QD and SWCNT (**Figure 55**c). The three DNA sequences (**Table 5**) of 10, 20 and 30 bp have length of 3.4 nm, 6.8 nm and 10.2 nm respectively. The QDs used are coated with streptavidin proteins adding 4 nm more to the linkers length. Therefore, the 10 bp, 20 bp, and 30 bp linked hybrids have approximate spacers of 7.4 nm, 10.8 nm, and 14.2 nm respectively.

Oligo name	Sequence
Am10b	Amine – CAGGCTCAGG
Bio10b	Biotin - CCTGAGCCTG
Am20b	Amine - TGCTATGCAGCAGGCTCAGG
Bio20b	Biotin - CCTGAGCCTGCTGCATAGCA
Am30b	Amine - TGCTATGCAGCGGTCAACTACAGGCTCAGG
Bio30b	Biotin-CCTGAGCCTGTAGTTGACCGCTGCATAGCA

Table 5*: List of sequences used for 30 bp, 20 bp, and 10 bp linkers.*

The formation of SWCNT-DNA-QD heterostructures was monitored by casting diluted solutions on mica, and imaging the substrate via Atomic Force Microscopy (AFM): **Figure 56**a shows a representative image of SWCNT-10bp-SWCNT, while **Figure 56** b and c shows representative AFM images for the 20 and 30 bp nanohybrids. **Figure 57** shows the topography AFM images and the respective height profile of the pristine CNT and QDs.

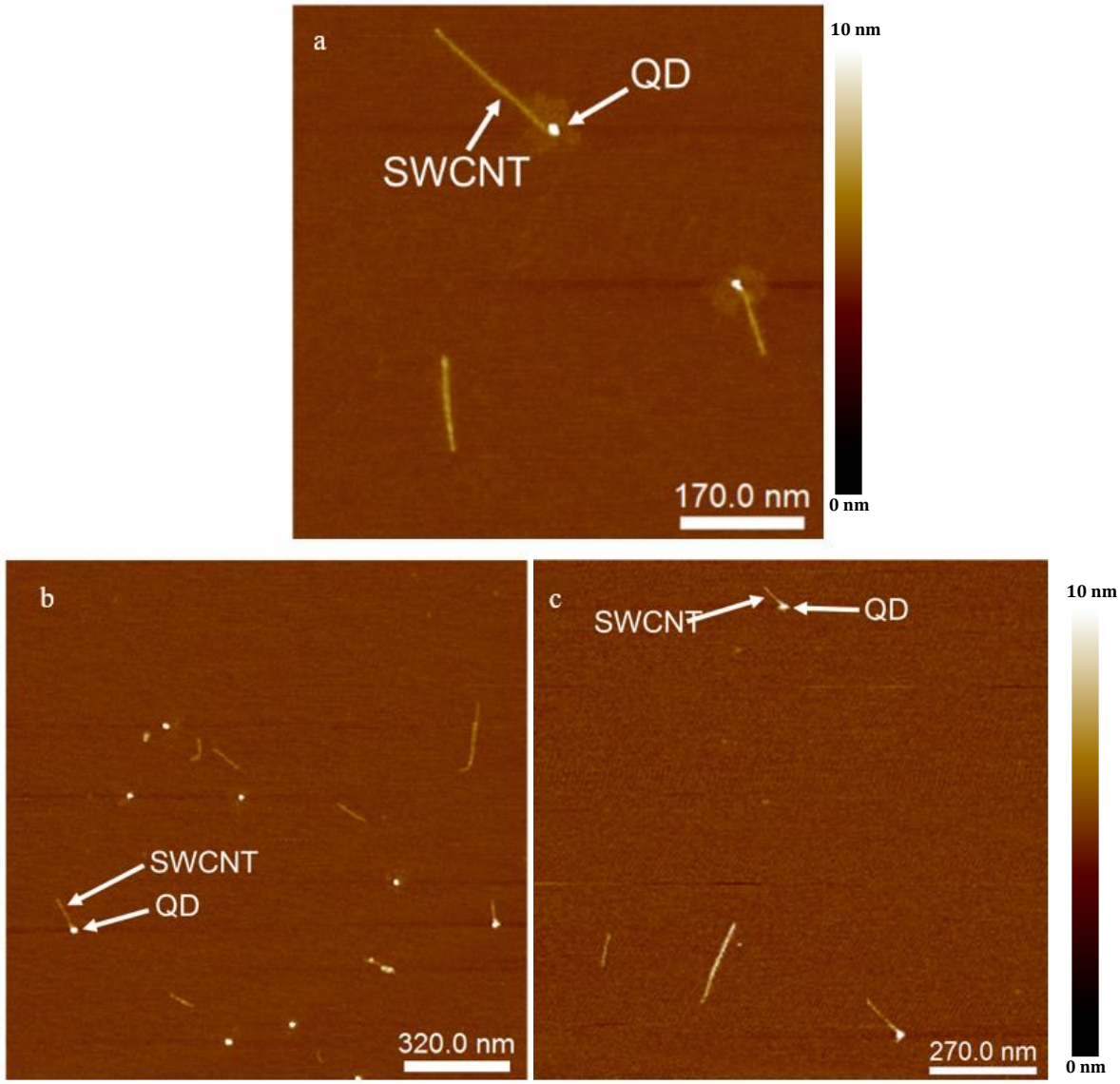

***Figure 56**: AFM topographical image on mica of SWCNT-QD hybrids: 10bp (a), 20bp (b) and 30bp (c). Scale bar for (b) and (c) is the same.*

The yields of formation of the SWCNT-QD nanohybrids, as measured by AFM, were found to be ~25%, where 100% of the heterostructures presented only one QD at one terminal end of the nanotube, i.e. were monofunctionalized. 2:1 SWCNT-QD nanohybrids formation was minimized by the mildness of the aforementioned nanotubes acid treatment, so that the SWCNTs ends were not saturated with carboxylic defects.[198–200] Furthermore, it is unlikely that more than one QD would attach to the same end of the SWCNT, due to spatial constraints.[201]

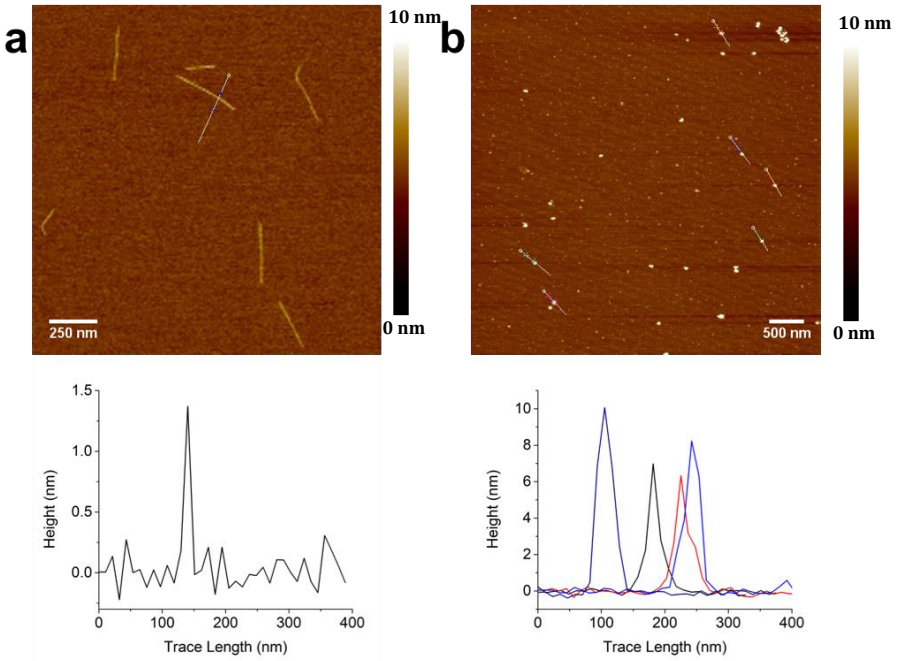

***Figure 57**: Topography AFM height analysis of (a) pristine SWCNT, (b) pristine QDs.*

4.3.2 Steady State Photoluminescence

In order to study the electronic coupling between the SWCNT and the QD and how it is affected by different DNA linkers, photoluminescence (PL) investigations were carried out. All nanohybrids were prepared by keeping the concentration of QDs constant across all samples so as to accurately determine the communication with the CNTs.

Figure 58 shows the stationary luminescence of pristine QDs as well as QDs simply mixed with SWCNT and the nanohybrids highlighting that the QDs emission was progressively quenched to a higher degree as the nanoparticle approached the end of the SWCNT in our heterostructures. Specifically, the QDs in the 30 bp hybrids were quenched by 47% relative to the pristine QDs emission, while the QDs in the 20 bp and 10 bp hybrids were quenched 52% and 63% respectively. The mix of QD with CNT without any DNA linkers showed a quenching of about 7% (**Figure 58**) so the observed quenching can be unambiguously attributed to some kind of electronic coupling, as described previously in Section 3.2.4. As shown in **Figure 58** there is a sequentially increase of PL quenching for 30, 20 and 10 bp hybrids suggesting that a gradually stronger coupling occurs when the QDs are positioned closer to the nanotubes.

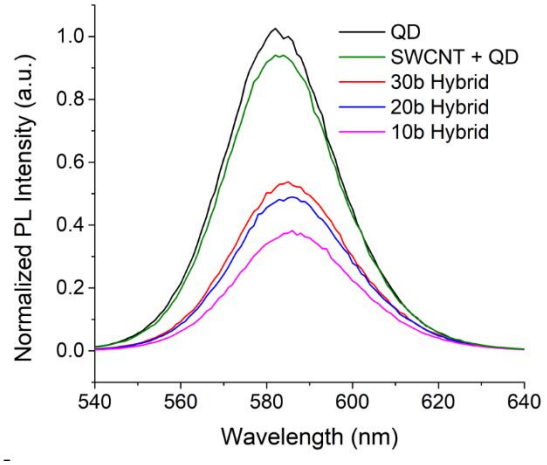

***Figure 58**: Stationary state fluorescence spectra of pristine QDs (black), SWCNTs and QDs in absence of DNA linker (green), and the 30 bp hybrid (red), 20 bp hybrid (blue), and 10 bp hybrid (pink).*

As a control experiment QDs were conjugated with dsDNA linkers in absence of any CNT as shown in **Figure 59** and a quenching of 40% was observed for the DNA functionalized QD for all sequences compare to the pristine QD but only very small differences were observed among each length of duplex compared to the relative quenching observed for the hybrids.

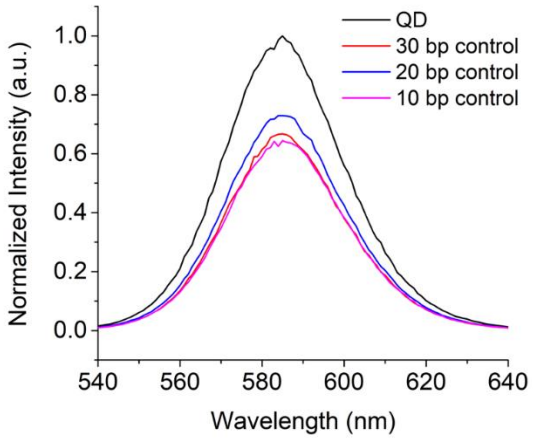

***Figure 59**: Stationary state fluorescence spectra for the control experiment of pristine QDs compared to QDs with DNA conjugated.*

4.3.3 Time Resolved Photoluminescence

Time-resolved PL (TRPL) investigations were carried out in order to investigate the decay dynamics of the electronic excitations in our heterostructures, and hence elicit the coupling mechanism between the two nanostructures forming the hybrids. **Figure 60** shows that pristine QDs exhibit a lifetime decay with a biexponential trace, as described in Chapter 3 section 3.2.6, with the shorter lifetime (t_1) attributed to the recombination of core states and the longer lifetime (t_2) to radiative recombination of excitons involving surface states. As the QD approaches the SWCNT in the monofunctionalized hybrids, both the lifetimes were observed to progressively shorten (see **Figure 60** and inset table). At the same time, in the transition from 30 bp to 10 bp, the emission follows a near-monoexponential decay with up to 98% of the emission concentrated on the shorter lifetime.

As stated in Chapter 3 the shortening of both lifetimes is a clear indication of electronic coupling while an increase in the amplitude of shorter lifetime at the expenses of the longer one is indicative of charge transfer. We can infer that, at longer coupling distances, energy transfer is likely the dominating process of electronic coupling between the QDs and the SWCNTs; as the linker's length shortens (10 bp), charge transfer becomes the dominating process.

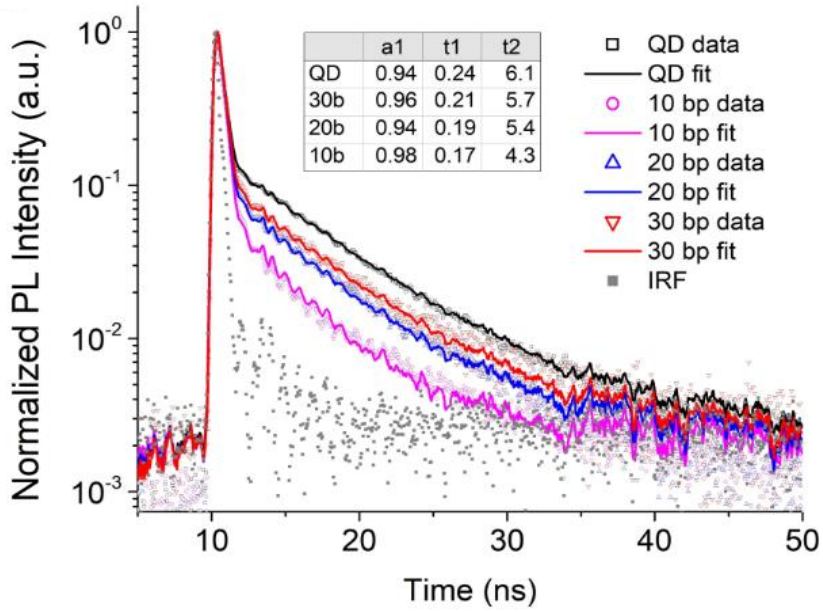

***Figure 60**: Normalized time-resolved photoluminescence measurements of pristine QDs (black), 30 bp hybrid (red), 20 bp hybrid (blue), and 10 bp hybrid (pink).*

TRPL control experiments were carried out where only the DNA linkers were attached to the QDs, in the absence of the SWCNTs and no difference in lifetime for the control DNA-QD samples when compared to the pristine QDs was observed (**Figure 61**a).

Differently, by simply mixing QDs with SWCNTs in the absence of the DNA linkers a decrease in lifetime was observed; interestingly the lifetime value of this mixture fell between the 30 bp and 20 bp nanohybrids (**Figure 61**). Differently, by simply mixing QDs with SWCNTs in the absence of the DNA linkers, a shorter lifetime was observed compared to the pristine QDs, with a value comparable to the 30 bp nanohybrid (see **Figure 61**b). This suggests that the average distance between the QD and the SWCNT in the mixture solution is comparable to the distance in the 30bp hybrid.

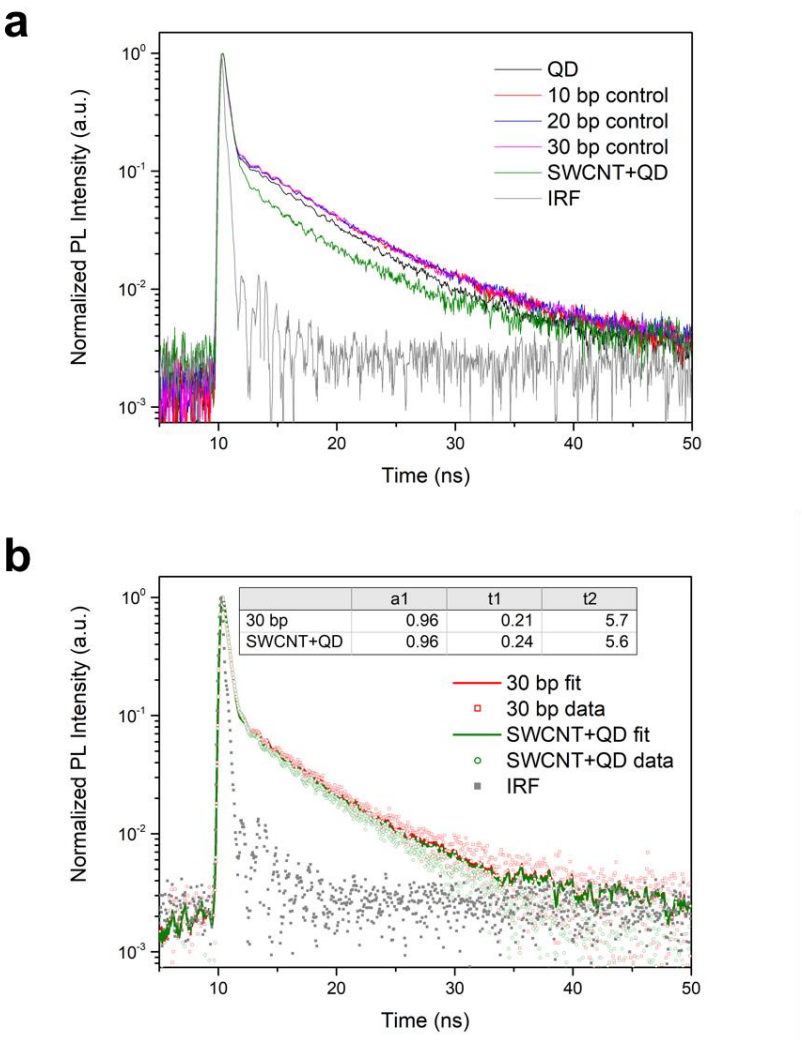

***Figure 61**: (a) Normalized time-resolved photoluminescence measurements for the control experiment of pristine QDs compared to QDs with DNA conjugated (b) Control experiment of 30 bp hybrid (red) and SWCNT and QD mixture (green).*

4.3.4 Steady State Photoluminescence of CNT

In addition to monitoring the QD emission, SSPL studies were carried out on the SWCNTs for each nanohybrid, as well as for the pristine nanotubes. The PL spectra of CNT have been reported to be modified when the tubes are functionalized in response to both energy transfer[82] or charge transfer processes.[99] The semiconducting SWCNTs used in these experiments emit, as expected, in the IR region (see **Figure 62**) where the observed peaks correspond to the different chiralities of tubes in solution:

- 1080 nm correspond to 6,5 chirality
- 1137 nm correspond to 7,5 chirality
- 1202 nm correspond to 8,4 chirality
- 1276 nm correspond to 7,6 chirality

No significant difference in emission was observed between the nanotubes in the hybrids and the pristine SWCNTs. This is likely due to the high specificity of our functionalization, where single QDs are only tethered to the ends of the nanotubes, hence the electronic structure of the SWCNTs is preserved, with only local changes potentially occurring at the site of QDs attachment.

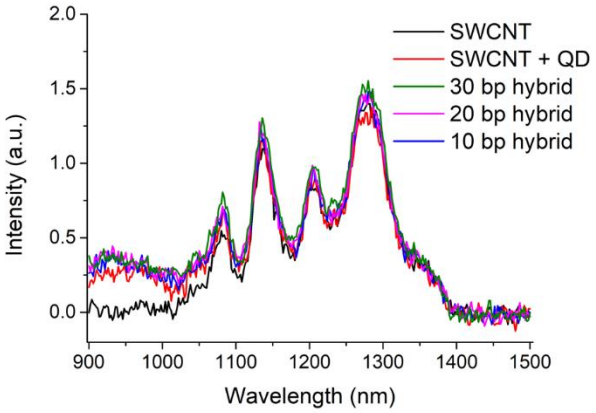

***Figure 62**: Stationary state fluorescence of pristine SWCNT (black), SWCNT and QD physically mixed (red) and SWCNT-QD hybrids 30bp (green), 20 bp (pink) and 10 bp (blue).*

4.3.5 Single Molecule Photoluminescence (blinking)

To further monitor the electronic coupling with single-particle resolution, single-molecule measurements were performed. We cast low-density films on glass substrates so to obtain physisorbed QDs or SWCNT-QD hybrids spaced at least 1 μm apart, therefore optically resolvable (**Figure 63**).

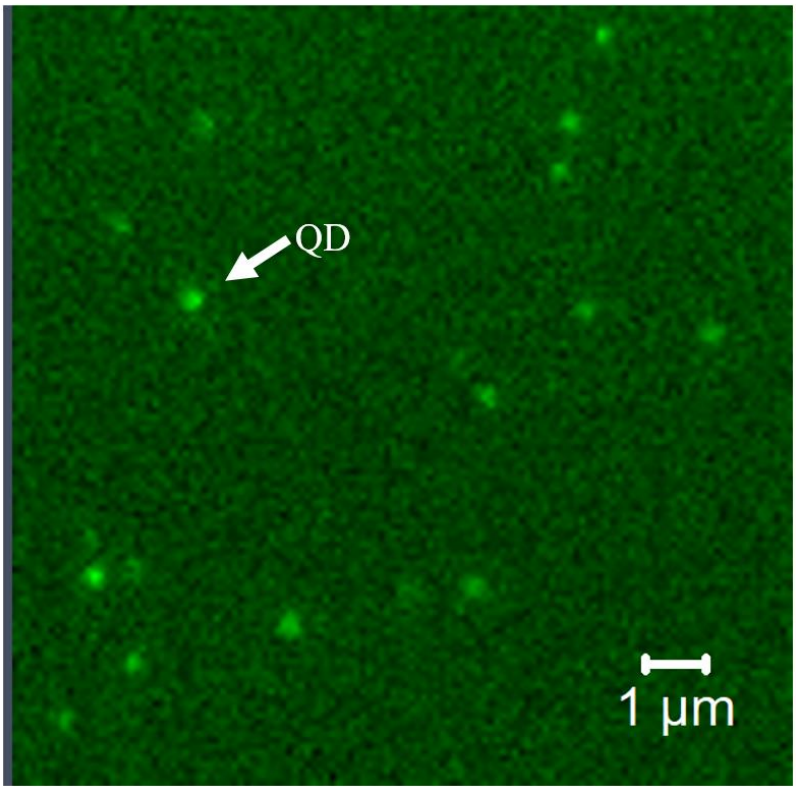

***Figure 63**: Representative image frames taken from the movies used to study the PL blinking of QDs.*

This allowed to carry out PL studies of individual nanoparticles and heterostructures on surfaces. Emission intensities from single QDs and SWCNT-QD hybrids were plotted against time as shown in **Figure 64**. When progressing from pristine QDs to 30 bp, 20 bp and 10 bp linked hybrids, longer OFF times (lower QD emissivity) were measured confirming that as the QD approach the carbon nanotube there is a progressive increase in the electronic coupling between the two nanostructures in agreement with the stationary and time resolved PL data (Sections 4.3.2 and 4.3.3).

By setting a threshold to discriminate between on and off states and accumulating the OFF time data for about 25 individual QD and CNT-DNA-QD heterostructures, probability distributions of OFF events can be constructed (see **Figure 64** and equations in Section 2.7) all of them following a power-law dependence (Section 2.7): pristine QDs were found to have an exponent of 1.66 – in agreement with literature values [46, 78-79] – while the 30 bp, 20 bp, and 10 bp nanohybrids were seen to follow a decreasing trend with exponents of 1.58, 1.48, and 1.39 respectively indicating a progressive increase to have longer and more frequent OFF states as the QD is located closer to the tube. These changes in the blinking statistics, can be explained by the progressive increase of charge transfer (CT) as the dominant mechanism responsible for the observed electronic coupling, with decreasing distance between the tubes and the QDs in the hybrids. The rate of CT to the CNTs is comparable with the intrinsic radiative decay rate of the QDs, hence the CT process becomes competitive with the emission process (ON state), leaving the QDs in a charged non-radiative state (OFF state) for longer times.

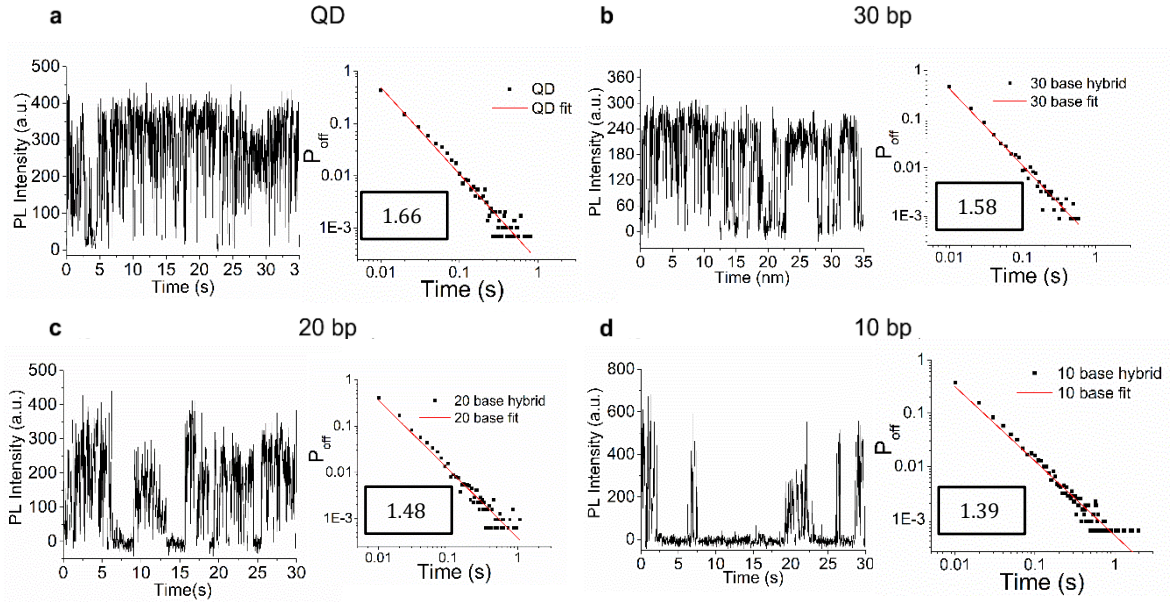

***Figure 64**: Representative blinking profiles of single and "Off" time probability distributions of (a) pristine QDs, (b) 30 bp linked SWCNT-QD, (c) 20 bp linked SWCNT-QD, and (d) 10 bp linked SWCNT-QD. The numbers in the inset correspond to the slope of linear fit.*

This trend is also confirmed by the plots of the occurrence of the PL intensities of the cumulated blinking traces shown in **Figure 65**. The graphs show the expected bimodal distributions with a peak distributed close to zero which correspond to the OFF states and a second distribution centred at higher intensities corresponding to the ON states. It can be noticed that as the QD is put closer to the CNT the occurrence of the on distribution showed a decrease in high and a progressive broadening confirming the reduction and shortening of on states as DNA sequence length is reduced.

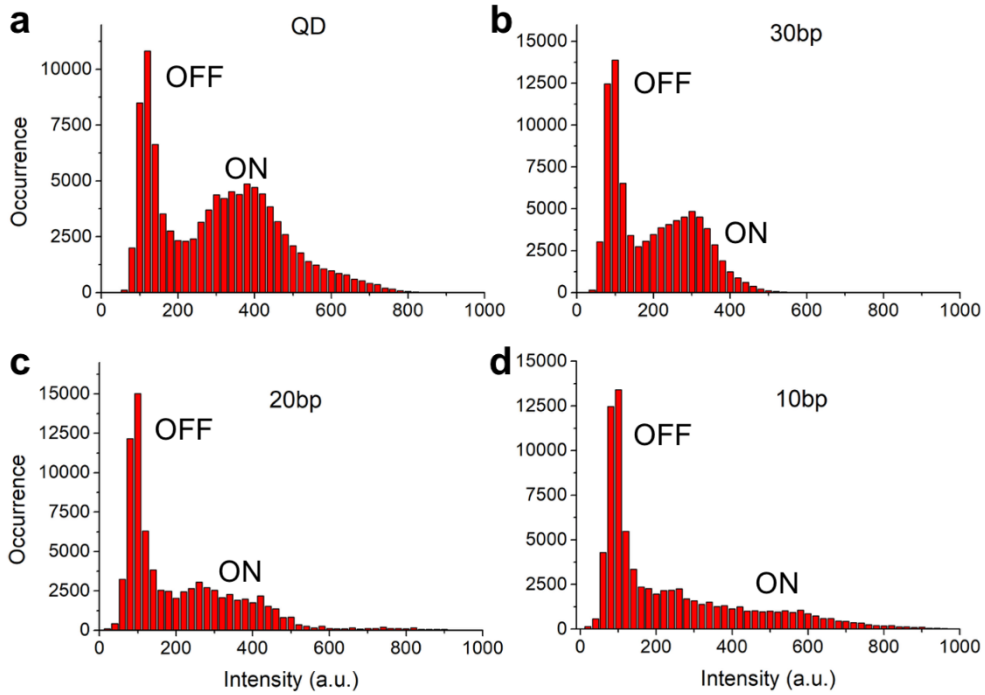

***Figure 65**: Histograms of the emission intensities from accumulated blinking traces for (a) pristine QDs, (b) 30 bp hybrids, (c) 20 bp hybrids, and (d) 10 bp hybrids.*

4.4 Conclusions

In summary, in this chapter is presented the controlled assembly of one-to-one SWCNT-QD nanohybrids via the use of different linkers, e.g. π-conjugated molecules, alkyl chains and dsDNA: the electronic coupling between the two nanomoieties was tuned employing linkers of different length, chemical nature and degree of conjugation. This approach allowed to investigate the importance of the bridging moiety between QDs and SWCNTs in the hybrids enabling a further control over the processes occurring at the interface.

AFM images showed the successful assembly strategy of QD-CNT hybrids where QDs were attached only at the terminal ends of SWCNTs. Low yields of hybrid formation were obtained for the conjugated linkers with 1, 2 and 3 phenyl rings, and for the alkyl chains linkers (about 5 % in all cases), while higher yield of attachment were obtained using DNA linkers (35 %).

In the case of conjugated and alkyl chains linkers, even if a reduction of the lifetimes was observed in the hybrids compared to the pristine QDs, no significant differences were observed among the linkers employed; this is likely due to the low yield of the coupling reaction with very few hybrids formed, hence it was not possible to investigate the effective role of the linkers on the CNT-QD electronic coupling.

A different approach could be used in the future to increase the yield of the reaction, for example, by directly changing the capping agent on the QD surface with a ligand exchange procedure and then perform the coupling with the CNT via a different covalent reactions: ongoing experiments in the Palma group show higher yields of reaction employing click, photolysis and diazonium-salt one-step based reactions (unpublished results). Moreover, a further step could be developed in order to remove free QDs in solution (through filtration or density gradient centrifugation techniques) which may be responsible for the incapacity to distinguish the effect of each linker on the electronic coupling by smoothing out the PL signal. These preliminary results, using conjugated and alkyl chains linkers, were not entirely satisfactory but were found to be very important in the development of the assembly and photophysical characterization of QD-CNT hybrids were DNA was employed as the bridging moiety.

Differently, in the case of the DNA linkers, SSPL demonstrated a distant dependence quenching on the emission of the QD, where a closer proximity to the SWCNT increased the extent of the electronic coupling. TRPL measurements and single molecule fluorescence microscopy investigations on individual QDs and heterostructures confirmed the DNA distant dependence trend of the QD-SWCNT coupling. Moreover, these measurements indicated that charge transfer becomes the dominating coupling process as the distance between the tubes and the QDs is controllably reduced.

The work described in this chapter provides a general strategy for the regulation of the electronic coupling in solution processable organic-inorganic heterostructures with single particle control; its general applicability is of great interest in the assembly of single

molecules optoelectronic nanodevices and fundamental investigations of energy and charge transfer processes at the nanoscale.

5 GRAPHENE NANOFLAKES-QUANTUM DOTS HYBRIDS

5.1 Introduction

In Chapters 3 and 4 the assembly and photo-physical investigations of 0D-1D hybrids was discussed where quantum dots (QDs) were attached with single particle control solely to the terminal ends of individual SWCNTs. Here an assembly strategy in water is discussed for the formation of semiconductor quantum dots - graphene nanoflakes hybrids, where QDs are tethered to graphene nanoflakes (GNF) via the formation of a covalent bond. The synthetized GNF-QD hybrids were further integrated into a photovoltaic device showing improved generated photocurrent.

The combination of graphene and semiconducting nanocrystals (quantum dots, QDs) in functional heterostructures has attracted growing interest[16,202–204] due to the tuneable emitting and efficient broadband light harvesting properties of QDs, and the mechanical robustness and excellent charge transport properties of graphene, as new functionalities and enhanced photo-response properties can emerge at this organic-inorganic interface.[205–207] Graphene and semiconductor quantum dots have been widely studied and a number of devices have been developed for several applications including sensors,[208] photodetectors,[209,210] solar cells,[211,212] transistors,[213] optoelectronics,[214,215] and catalysis.[216–218] In such devices the QDs act as the photo active component while graphene based materials are usually employed to enhance charge extraction from the nanocrystals and favour the transport of photo-generated carriers. Nevertheless, main challenges need to be overcome, such as the graphene relatively high inertness and low solubility which results in major issues in terms of assembly and processability. This is even more pronounced for water based approaches, where the high degree of hydrophobicity of graphene promotes aggregation and subsequent precipitation hampering a full control over the hybrids formation.[219] The most common route in order to overcome such a problem, is the functionalization of graphene through the introduction of oxygen containing groups as defects on the sp2 carbon network resulting in the formation of graphene oxide (GO).[16,220] Such procedure increases the material solubility through the

introduction of oxygen containing groups as defects which can be further used as anchoring groups for the subsequent chemical attachment of other components. However, this results in unspecific and uncontrolled functionalization, with defects that can be localized anywhere on the inner graphitic plane as well as at the edges; even if oxides can be removed through a subsequent reduction generating reduced graphene oxide (rGO), this adds yet another step and cannot remove the majority of the structural defects introduced by the oxidation process.

Key to the implementation of these QD-graphene hybrid materials into devices is also the control over the nature of the interface between the two components as well as the effective electronic coupling, as a strong QD-carbon moiety connection is a required condition in order to have better electrochemical performances. In this regard a covalent immobilization to form nanohybrids would ensure a stronger chemical bond and a superior coupling compared to 'graphene composites' or 'nanocarbon composites' made by physical mixing methods.

A self-assembly strategy in water is presented for the functionalization of graphene nanoflakes with quantum dots where graphene nanoflakes are characterized by a high density of carboxylic groups at the edges that act as anchoring groups for the covalent attachment of CdSe/ZnS quantum dots. Evidence of strong electronic coupling between the two nanomoities is shown through stationary and time resolved photolumiscence in solution and on surface with single particle control, and through Raman spectroscopy, providing evidence of charge transfer. A solar cell is also fabricated based on our GNF-QD material, which generated higher photocurrent compared to the same device made of only QDs. The work presented here was carried out in collaboration with Dr Martin Rosillo-Lopez and Dr Christoph G. Salzmann from University College London for the GNF synthesis, and Dr Andrea Zampetti, Ioannis Ierides and Prof Franco Cacialli from University College London for the measurements on the devices.

5.2 Assembly

Water soluble carboxylated graphene nanoflakes (GNF) were employed, prepared through oxidative break-down of multiwalled carbon nanotubes in a mixture of concentrated sulfuric acid and nitric acid, as previously reported.[221] These graphene nanoflakes are characterized by a relatively low defect density on graphene internal basal plane while they show high density of carboxyl groups along the edges[222,223] (Figure 66 a and b).

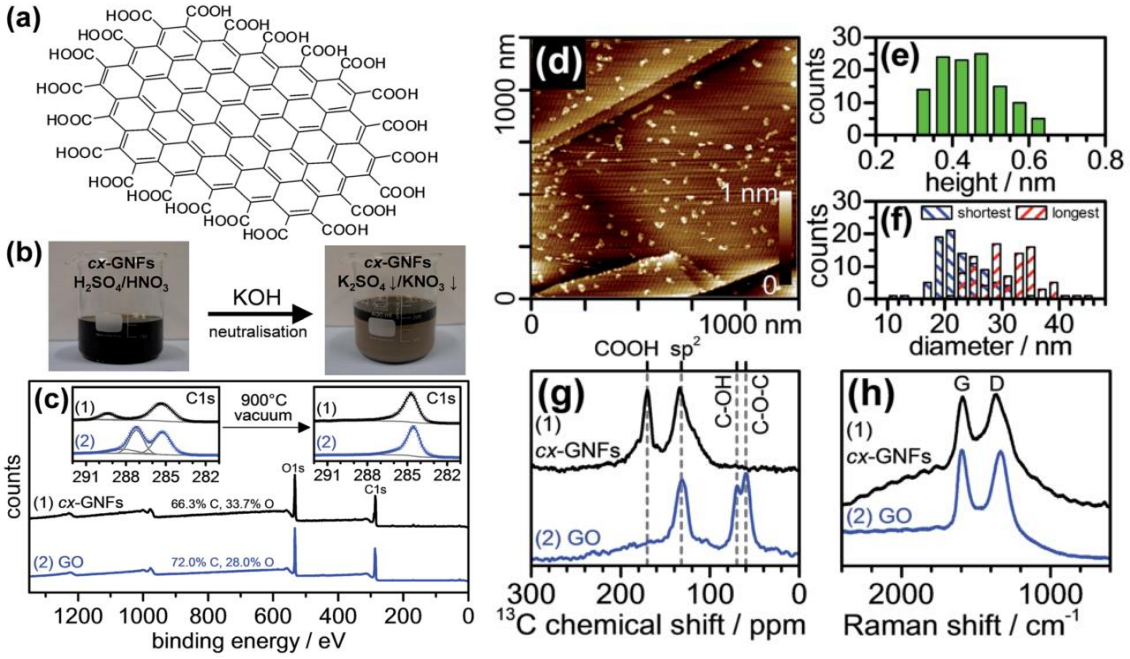

***Figure 66**: Chemical composition and structure of GNFs. (a) Idealised chemical structure of a small cx-GNF. (b) Photographic images of the filtered reaction mixture before and after neutralisation. (c) X-ray photoelectron spectra of GNFs and GO. The insets show the C1s region before and after heating to 900 C under high vacuum. (d) Atomic force microscopy image of GNFs spin-coated onto highly oriented pyrolytic graphite. (e) Height and (f) diameter distribution of the GNFs. (g) 13C solid-state NMR and (h) Raman spectra of GNFs and GO.(taken from ref* 221*).*

The purity of the GNFs is illustrated by the X-ray photoelectron spectrum in **Figure 66**c which shows no other elements than carbon and oxygen with the presence of sp2 carbon confirmed by a high-resolution spectrum of the C1s. Consistent with the XPS results, the 13C solid-state NMR spectrum of GNFs shown in **Figure 66**g indicates the presence of sp2 carbon and carboxylic acids, and the absence of alcohol and epoxide groups which are characteristic for GO. The Raman spectra of GNFs and GO on the other hand are quite similar which may indicate that the graphenic regions within our GO are of similar dimensions as the GNFs (**Figure 66**h). It has been demonstrated that the carboxyl groups at the edges of the nanoflakes are in dynamic equilibrium with carboxylic anhydride groups in water (**Figure 67**) which are characterized by a high reactivity towards nucleophilic attack at the carbonyl carbon atom[221] and therefore offer themselves for straightforward chemical functionalization under mild conditions.

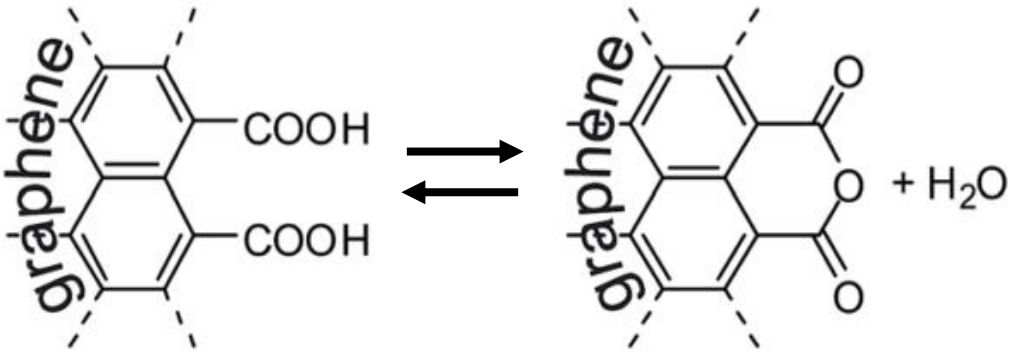

***Figure 67**: Reaction scheme of the anhydride formation in the GNF.*

Taking advantage of this high reactivity, commercially available, water soluble amino functionalized QD were employed, which rapidly attack the C=O groups at the edges of the nanoflakes forming amide bonds (**Figure 68**). The formation of amide bonds between amine groups and the carboxylic groups in similar system has been previously proved through FTIR and zeta potential measurements.[221] This strategy allows to covalently attach QDs to the graphene nanoflakes in a very easy way by simply mixing the two components in water, in an environmentally friendly and biocompatible solutions.

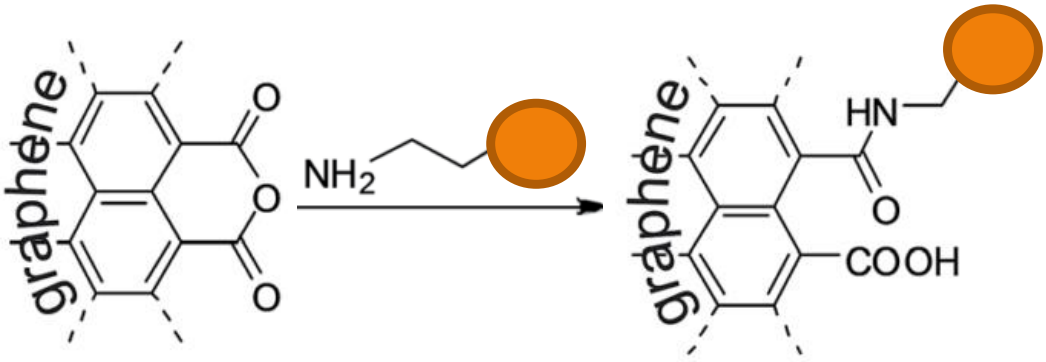

***Figure 68**: Schematic of GNF-QD reaction formation in water.*

Diluted nanohybrids solutions were cast on highly pyrolytic graphite (HOPG) and imaged via atomic force microscopy. **Figure 69** shows topography AFM images of the pristine materials GNFs and QDs, while **Figure 70** is a typical topography AFM image of QD-GNF nanohybrids: the QDs are completely surrounded by the nanoflakes with more than

one flake covalently attached to a QD, or in some cases flakes can be found bridging two or more QDs into small aggregates.

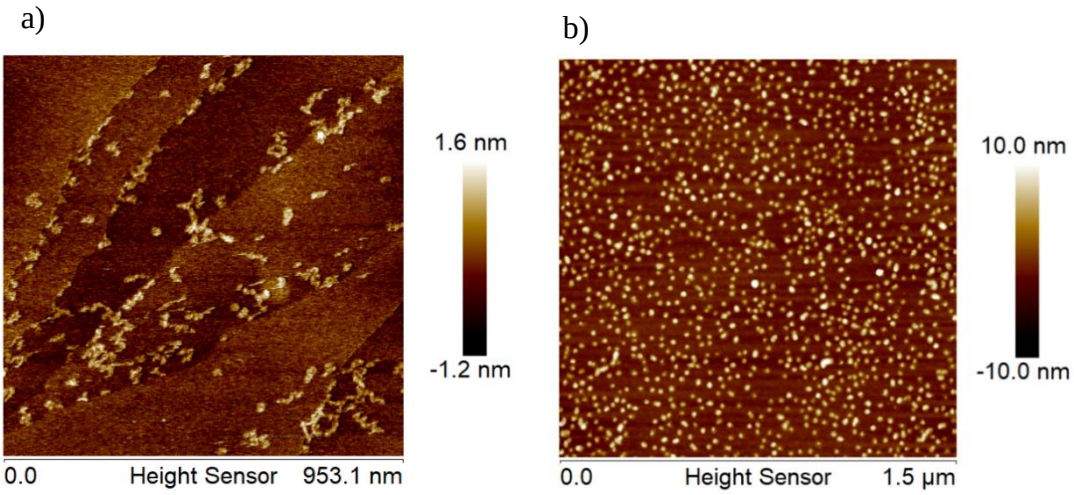

***Figure 69**: Topography AFM images of pristine GNFs (a) and pristine QDs (b).*

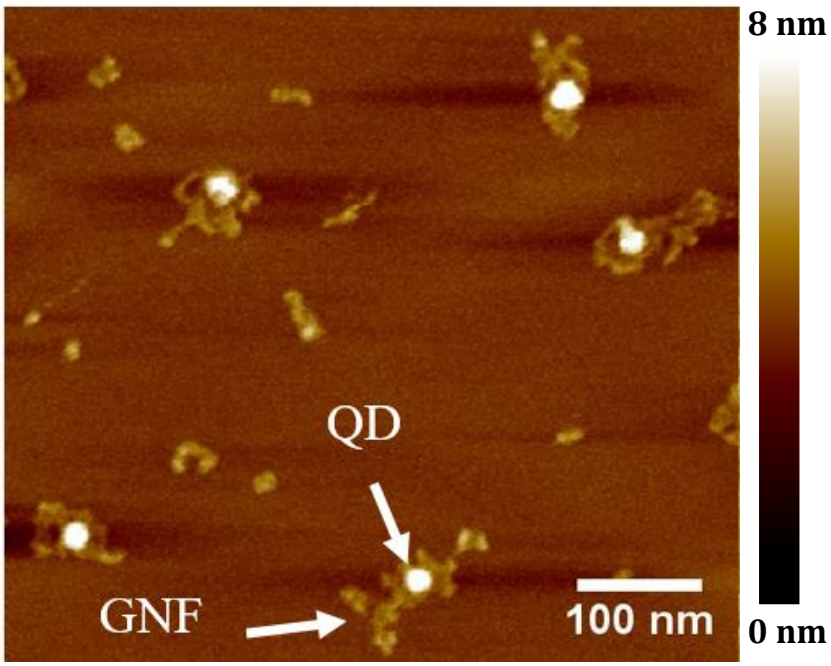

***Figure 70**: Topography AFM images of GNF-QD hybrids.*

5.3 Photo-physical Characterization

5.3.1 Introduction

Evidence of electronic coupling in graphene-based materials and QDs hybrids has been previously reported, and both energy transfer as well as charge transfer have been proposed as mechanisms for the deactivation of the excited state of QDs tethered to graphene. Such a variety of results and interpretations is mainly due to the diversity of the specific systems investigated: the use of different graphene-based material (either pure graphene, GO o rGO), the organic capping agents used to modify the surface of the QDs as well as the nature of the chemical bond (covalent or non-covalent/electrostatic interactions). All of these parameters affect the degree of the electronic coupling between the two components hence resulting in a completely different interface with remarkably various effects on the physical chemical properties of the resulting hybrids.

Brus and co-workers[224] demonstrated the occurrence of resonant (Forster) energy transfer from individual CdSe/ZnS nanocrystal spun coated onto a single and few layers graphene sheets. In particular, they observed a strong quenching of the photoluminescence of the nanocrystals together with a suppression of the quantum dots blinking (**Figure 71**).

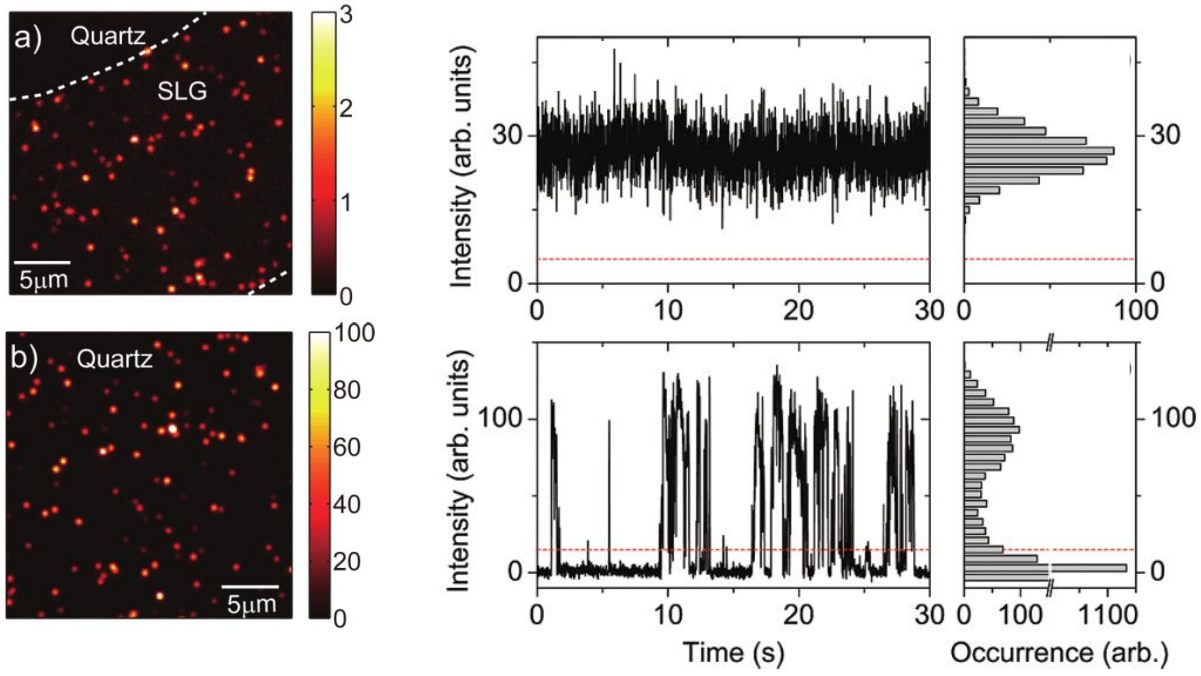

***Figure 71**: Fluorescence images for nanocrystals on a graphene monolayer (a) and on a quartz substrate (b). Fluorescence time traces from an individual nanocrystal lying on a*

graphene monolayer (c) and on a quartz substrate (d). The dashed horizontal lines indicate the intensity thresholds used to define the "on" and "off" states used in the text. Figures d and f are histograms of the emission intensities corresponding to figures c and d, respectively.(taken from ref 224*).*

Moreover, Federspiel and co-workers[160] further investigated the distance dependence of energy transfer from individual QDs to a graphene monolayer separated by a MgO thin films of different thicknesses. For increasing distances, it was found that the measured decay rate decreases significantly and that the energy transfer rate from individual nanocrystals to graphene decays as $1/d^4$.

Additionally, several papers reported the enhancement of the efficiency of solar cells based on graphene-semiconductor QD compared to devices based on QD only.[213,214,225–227] The increment in the efficiency of the graphene based device can be explained through an increase of the ejection of charges from the QD core to the graphene which acts as a hole trapping agent.

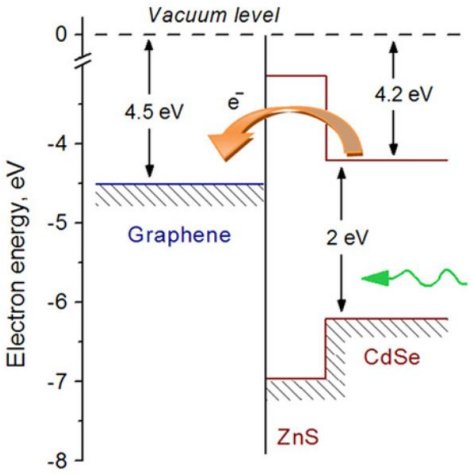

Figure 72*: Energy level diagram of the CdSe/ZnS QDs in contact with SLG.(taken from ref* 214*).*

Figure 72 shows the energy levels for a system involving CdSe/ZnS core/shell QD coupled with graphene: light can be absorbed by QD where electrons are excited from the conduction to the valence band; a possible route for the excited electrons could be

injection into the graphene in a lower energy level. Moreover, when graphene–QD materials are incorporated in a photovoltaic device under illumination, the presence of the electrolyte or other hole transporting materials favours the regeneration of the QD neutrality hence enabling a more continuous charge transfer (**Figure 73**).

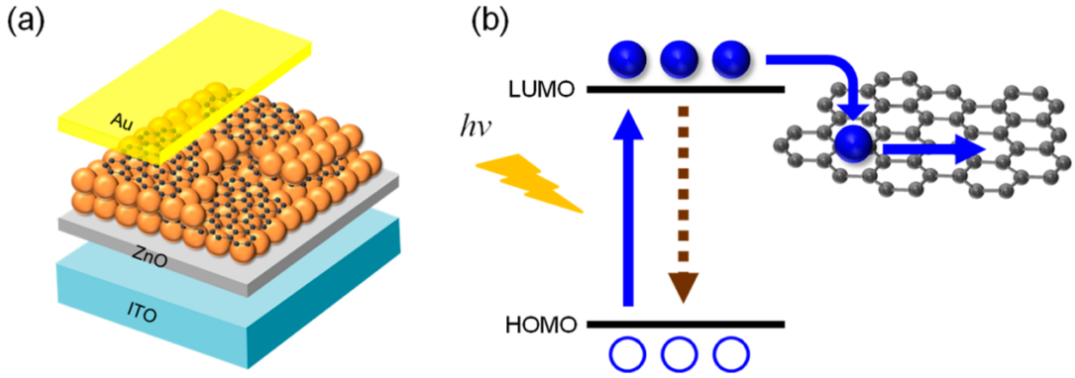

***Figure 73**: Schematic of (a) hybrid solar cell of graphene and semiconductor nanocrystals and (b) electron-transfer interaction.(taken from ref* 227*).*

Both electron transfer and energy transfer are possible mechanisms for the deactivation of the excited states of QD in contact with graphene but how is it possible to control these two processes with the aim of favouring the charge transfer process over the energy transfer process? One solution could be to increase the rate of electron transfer by improving the electronic coupling between nanocrystal and graphene through strengthening the chemical bond (covalent bond).

5.3.2 Steady State Photoluminescence

In order to demonstrate electronic coupling between the two nanomoieties the stationary photoluminescence of QDs was monitored by comparing solutions of pristine QDs and QD-GNF hybrids processed in exactly the same way (see methods Section 2.4.1). A 93 % quenching of the stationary luminescence of QDs was observed when attached to the GNFs compared to pristine QDs (**Figure 74**) which is a strong evidence of electronic coupling as described previously in similar systems.[201,226] The origin of such a quenching can be ascribed to either energy transfer[224] or charge transfer.[226]

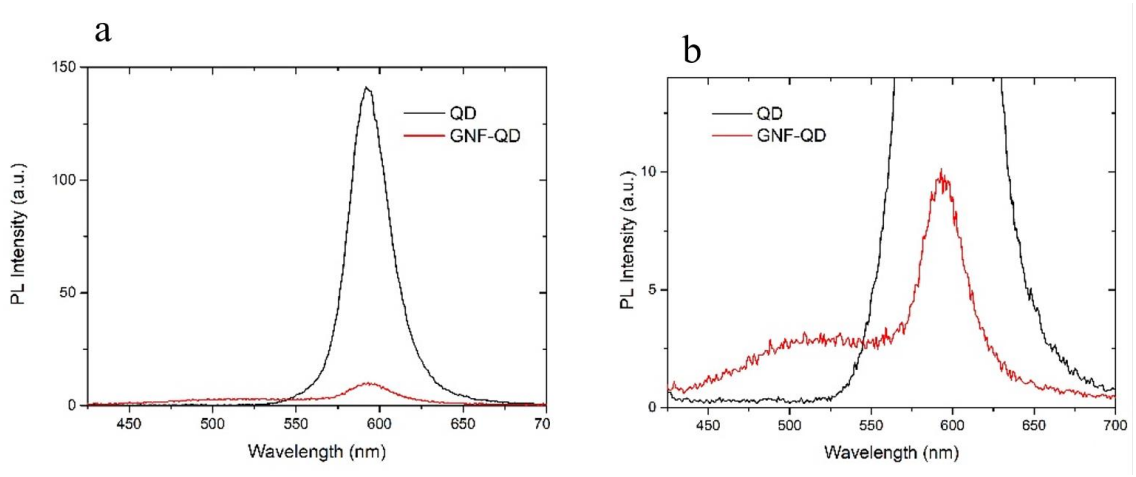

***Figure 74**: Photoluminescence spectra of QDs and GNF-QD hybrids. Samples were excited at 420 nm. The spectrum of QD-GNF hybrids shows a little shoulder centred at around 520 nm which is due to the luminescence of the nanoflakes themselves.*

5.3.3 Steady State Photoluminescence of Graphene Nanoflakes

The nanoflakes show a photoluminescence centred at 520 nm, in this regard they are very similar to GO and rGO, and its origin is generally ascribed to the presence of defects on the graphene honeycomb structure. These defects can be sp3 carbon, such as epoxy or hydroxyl groups in the inner part of the graphitic plane or carboxyl and carbonyl groups at the edges (see Section 1.1.2 in Chapter 1). The stationary and time resolved of this emission was investigated but found no difference in both intensity and lifetime as shown in **Figure 75**a and b. A possible explanation for the lack of variations in the GNF PL intensity and decay could be due to local effects of the quantum dots which are expected to be present only at the edges of the nanoflakes.

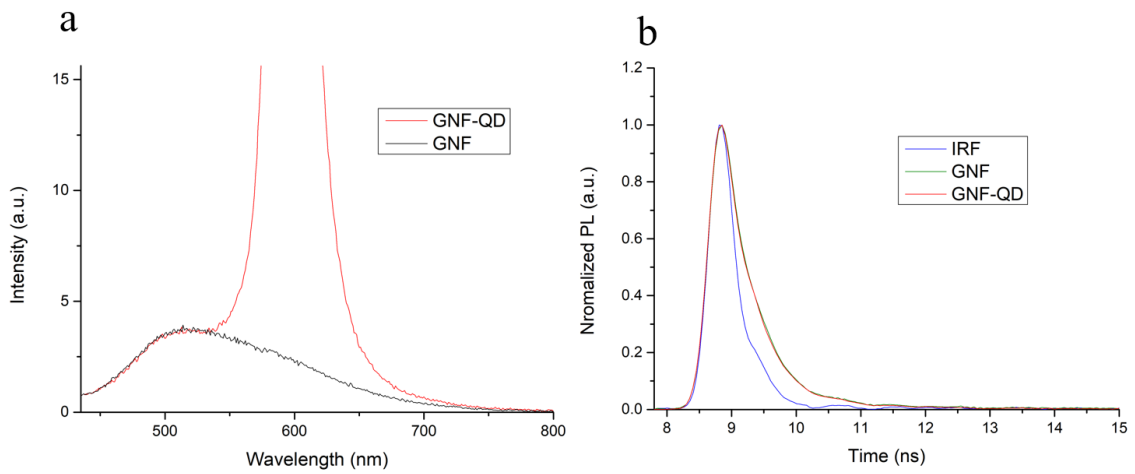

***Figure 75**: Stationary and time resolved photoluminescence of pristine GNF and GNF-QD hybrids. Samples were excited at 420 nm. Time resolved emission traces were collected at 520 nm.*

5.3.4 Quantum Yield (QY)

Quantum yield measurements were carried out in order to normalize the emission intensity of the QD photoluminescence by the different absorbance of the two samples (**Figure 76**) when estimating the quenching factor: since the graphene nanoflakes have a higher absorbance compared to the QDs, part of the incident light can be competitively absorbed by the nanoflakes and in turns the intensity of the QD photo-luminescence can be reduced with the effect of overestimating the PL quenching.

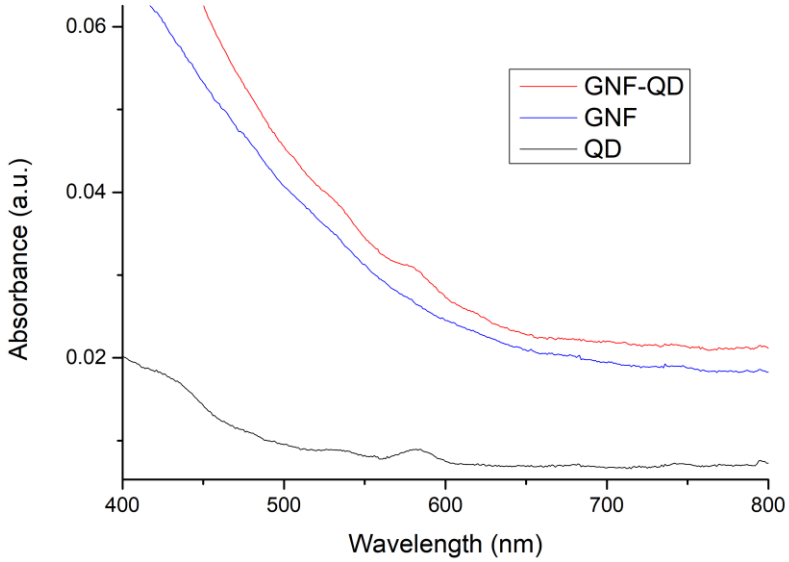

***Figure 76**: Uv-vis absorbance spectra of pristine QD (black), pristine GNF (blue) and GNF-QD hybrids (red).*

The calculated quantum yield values resulted to be: 0.225 ± 0.001 for the QDs and 0.0050 ± 0.0003 for the QD-CNT hybrids, indicating that with the same amount of absorbed photons when the QDs are attached to nanoflakes the number of emitted photons is about 45 times less than the pristine QDs.

5.3.5 Photoluminescence quenching in GNF-QD hybrids at different pH and solvent polarity

It was further studied how the change of pH and the polarity of the solvent affect the formation of the covalent bond, by monitoring the extent of the QD photoluminescence quenching in the hybrids. It is reasonable to assume that the quenching of the QDs PL, when attached to GNFs, as an indication of the degree of amidation reaction for the tethering of the QDs to the GNFs: higher is the quenching higher would be the electronic coupling between the two nanostructures hence higher would be the extent of the QDs attachment.

In order to be able to compare the PL intensities, and hence the PL quenching, each pair of samples of GNF-QD hybrids and pristine QDs, in the same conditions of pH and

solvent polarity, were processed in exactly the same way with the only difference of being respectively with or without the presence of GNFs. **Figure 77** shows the quenching of the PL of the QDs when attached to GNFs compared to the PL of the pristine QDs at different pH and at different water/EtOH volume ratio. The quenching was calculated according to the following equation:

$$Quenching = \left(1 - \frac{PL_{max}^{GNF-QD}}{PL_{max}^{QD}}\right) \times 100$$

with $PL_{max}{}^{QD}$ and $PL_{max}{}^{QD\text{-}GNF}$ representing the photoluminescence maxima at 594 nm of the QD and GNF-QD for each pair of samples with the same pH or solvent polarity. We observed a maximum PL quenching at pH 6 (80 %), and a 33% quenching at pH 7; the QD PL in the hybrids was quenched of only about 20 % in the other pH conditions investigated (pH 4.7, 8 and 9.5): (see Figure 77a). Differently, only slight variations were observed when the polarity of the solvent employed was altered (Figure **77**b)

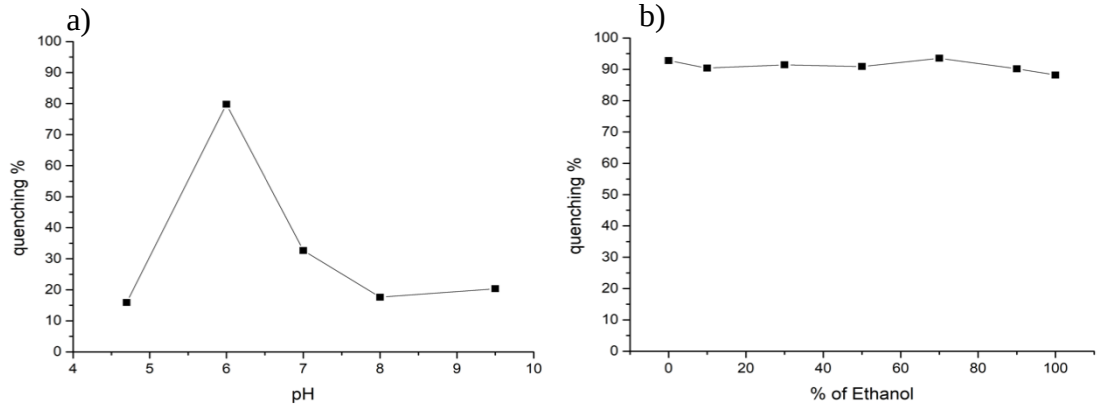

***Figure 77**: Photoluminescence quenching in GNF-QD hybrids at different pH (a) and at different percentage of ethanolic aqueous solutions (b).*

The change of quenching with the pH as well as the lack of any significant differences with solvent polarity, can be explained in terms of the covalent bond formation as illustrated in **Figure 78** describing the mechanism for the amide covalent bond formation

between the amino groups on the QDs and carbonyl groups on the GNFs: a nucleophilic attack of the amine on the carbonyl is followed by a deprotonation of the positive charged NH_2 group, the subsequent reorganization of charges in the intermediate allows the elimination of the leaving group and the formation of the amide bond.

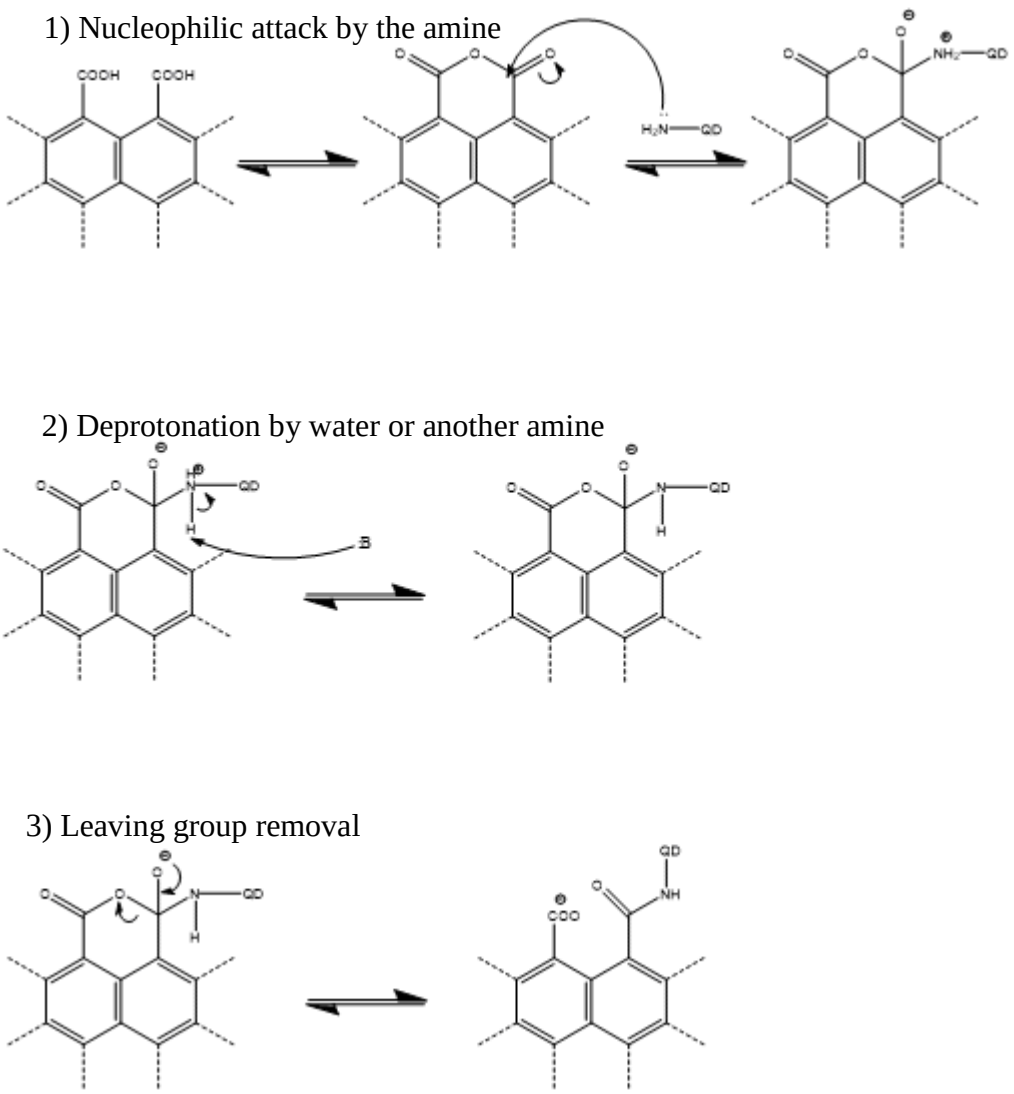

***Figure 78**: Schematic of the mechanism for the formation of the GNF-QD hybrids. B indicates a general basic compound.*

The pH can have a deep influence on the aforementioned reaction, in particular it is a key parameter for the stabilization of the various charged intermediates: if the pH is too low all the amino groups are protonated hampering the nucleophilic attack on the carbonyl and lowering the reaction yield; on the other hand a high pH promotes the formation of

the less reactive carboxyl group at the expenses of the anhydride lowering the yield of the reaction[228,144,229] (**Figure 79**). When there is no pH control over the course of the reaction, as in the case of the normal coupling conditions, the pH adjusts naturally around the optimum pH conditions as no acid or basic sub products are generated during the amide bond formation.

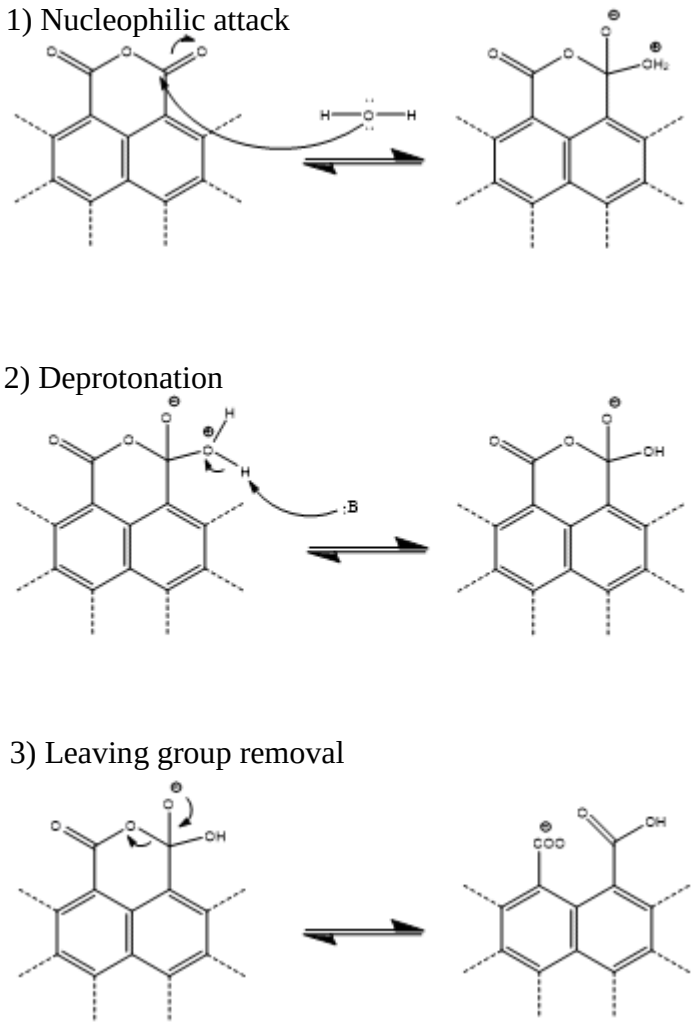

Figure 79*: Schematic for the base catalysed internal rearrangement for the formation of carboxyl groups from cyclic anhydride. B indicates a general basic compound.*

In this system, the best conditions were fulfilled around pH 6, where the highest degree of quenching (80%) was observed, in line with the pH depended reaction mechanisms discussed above and shown in (**Figure 78** and **Figure 79**). Moreover, the lack of any significant changes in the quenching of the QD emission, when the polarity of the solvent

is changed, supports the generation of a covalent bond rather than an electrostatic interaction, as only in the latter case a different distribution of the charges at the interface, induced by the solvent polarity, could potentially affect the GNF-QD interactions and the QDs emission in the hybrids.

5.3.6 Time resolved Photoluminescence

Since the quenching of stationary photoluminescence can be ascribed both to energy transfer as well as charge transfer between the excited state of QDs and the graphene nanoflakes, the decay dynamics of the electronic excitations in the system was investigated through time-resolved photoluminescence (TRPL). **Figure 80** compares the decay traces of the pristine QD and GNF-QD hybrids: pristine QDs are characterized by a typical bi-exponential decay where the shorter lifetime (t_1 = 0.83 ns) accounts for the emissive recombination of internal core states, while the longer one (t_2 = 3.3 ns) accounts for the radiative recombination of excitons involving surface states as previously described in Section 3.2.6. The two processes contribute almost equally to the total PL with 53 % of the total emission related to the core states emission and the remaining 47 % contribution related to the surface emission.

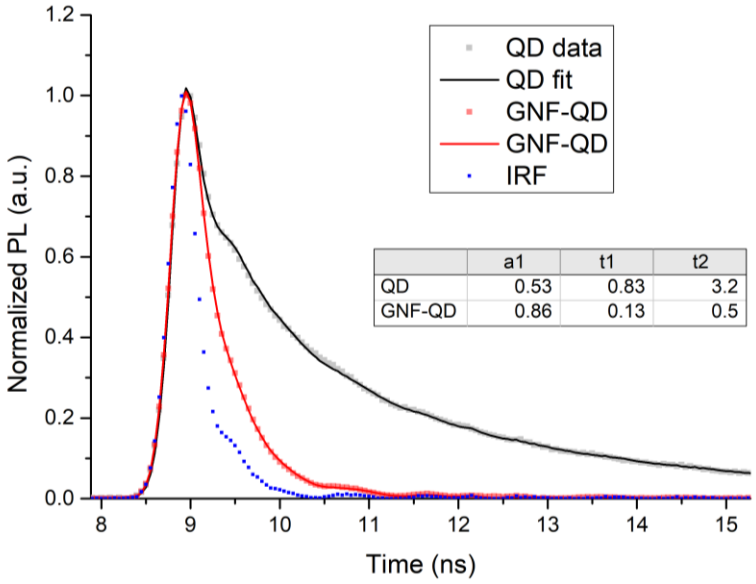

	a1	t1	t2
QD	0.53	0.83	3.2
GNF-QD	0.86	0.13	0.5

***Figure 80**: Normalized time-resolved photoluminescence measurements of QDs (black) and GNF-QD hybrids (red). Experimental kinetics have been fitted with a biexponential*

decay law, taking into account the effect of the measured instrumental response function (IRF, in blue) through a deconvolution. The fitting paraments are shown in the table.

In the case of the GNF-QD hybrids a shortening of both short and long lifetimes (t_1= 0.13 ns and t_2 = 0.5 ns) was observed while the PL decay followed a nearly monoexponential decay with 83 % of the emission due to the core recombination processes. The reduction of the total lifetime together with the increase of the contribution of the faster component to the total emission is an indication of charge transfer, as previously described in Section 3.2.6 for QD-SWCNT hybrids.

5.3.7 Single Molecule Photoluminescence Investigations (blinking)

To further investigate the nature of the electronic coupling between the two nanostructures PL studies of individual nano-structures with single particle control were carried out. We cast diluted solutions of the nanostructure on glass substrates in order to obtain physisorbed structures spaced at least 1 μm apart, hence optically resolvable (**Figure 81**).

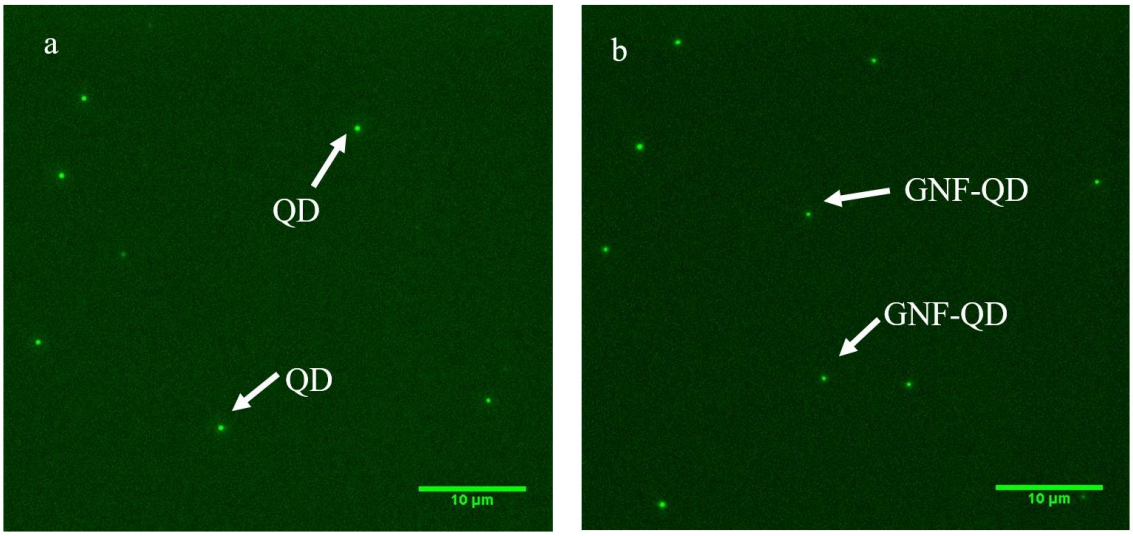

***Figure 81**: Representative image frames taken from the movies used to study the PL blinking of QDs (a) and GNF-QD hybrids (b).*

As described previously in Section 1.4.3 quantum dots exhibit dynamic fluctuation of fluorescence intensity (i.e. “blinking”), which is usually indicative of single emission behaviour: the bright states (ON states) correspond to the radiative recombination of light generated electron-hole pairs, while the states with no luminescence (OFF states) correspond to a non-radiative Auger mediated recombination which results in the ejection of charges from the nanocrystal leaving it in a charged ‘dark’ state.

Figure 82 a and c show two examples of the blinking traces of pristine QDs and GNF-QD nanohybrids respectively, highlighting how the trajectories are very different: QDs exhibit very short OFF periods which rapidly switch to ON states which dominate the blinking process; differently, GNF-QD hybrids show a prevalence of OFF states which are generally longer and more frequent. This behaviour is also confirmed by the histograms of the normalized intensities shown in **Figure 82** b and d, where the occurrence of the intensities of the combined traces of all the QD and GNF-QD investigated (over 30 QDs and QD-GNF hybrids) are characterized by two peaks which correspond to the OFF period at low PL intensity (at about 0.1) and ON periods (at about 0.8). The histogram related to the QD shows almost the same occurrence for the on and OFF states, while in the case of the GNF-QD hybrids we observed an increase of the occurrence of the OFF states which are almost double compared to the occurrence of the OFF states for the pristine QDs. As observed previously in the case of the QD-SWCNT hybrids in Section 3.2.7, the reduction of the blinking and the higher occurrence of OFF states can be explained with an increase of the Auger recombination process in the hybrids where the nanoflakes favour a charge extraction process leaving the QDs in a charged dark state for longer periods.

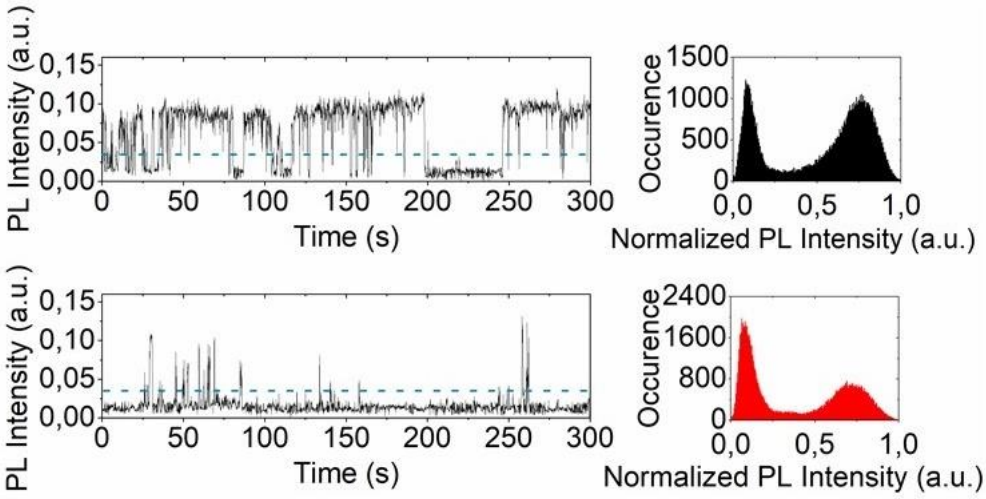

***Figure 82**: Typical fluorescence intensity traces for pristine QD (a) and GNF-QD hybrids (b). The dashed blue lines indicate the threshold used to discriminate between on and off states. Cumulated normalized fluorescence intensity histograms from over 30 traces for single QD (c) and GNF-QD (d).*

By selecting a threshold (blue line in **Figure 82** a and c) it is possible to discriminate between ON and OFF periods and for each time bin a probability of OFF states can be calculated, as shown in **Figure 83**, which confirms the different blinking behaviour.

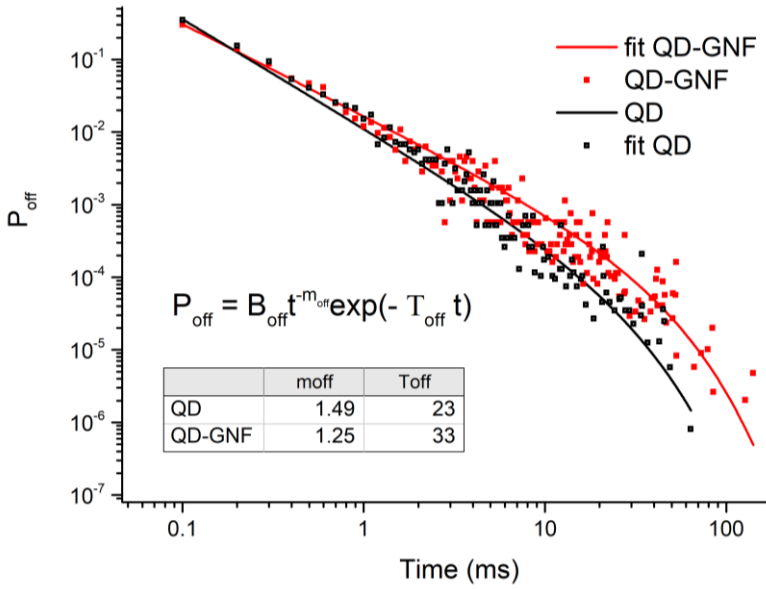

***Figure 83**: Probability density of off states constructed from over 30 single QD (black) and GNF-QD hybrids (red). Solid lines are best fit to the equation in the inset together with the fitting parameters.*

Both QD and GNF-QD show a power law distribution but deviate from this distribution at longer times as previously reported by other groups.[157,158] The probabilities can be fitted with a truncated power law (equation in the inset of **Figure 83**), where B_{off} is the amplitude, m is the power law exponent and T_{off} is the saturation rate; typical exponent for this type of QD are reported in literature to be between 1.5 and 1.7.[155,154] The calculated values of the exponents for pristine QD and the GNF-QD hybrids are respectively 1.49 and 1.25. The smaller m_{off} (table in **Figure 83**) indicates an increased probability density of longer off events as previously described in Section 3.2.7 for the SWCNT-QD hybrids and similar systems[157,158,201] and further confirms electron transfer process as a deactivation pathway of photoexcitated QDs.[32,33,35]

5.3.8 Raman Spectroscopy

Raman spectroscopy is a powerful technique to investigate the electronic structure of graphene and its derivative materials,[32,33,35] and can shed light on the behaviour of electron-hole pairs and excitons as intermediate states hence allowing the study of the effects of charge transfer processes in graphene. In particular, charge transfer events can alter the carrier concentration and mobility into the graphene with the effect of shifting the Fermi energy and therefore changing the graphene electronic and optical properties.[32,33]

Significant modifications in the properties of graphene, in particular its phonon spectrum and electronic structure, are reported to occur when electrons or holes are introduced by electrochemical means:[230–233] if the HOMO of a molecule is above the Fermi level of graphene, charges can be injected into the graphitic plane and the molecule acts as a donor; if, on the other hand, the molecule LUMO is below the Fermi level of graphene, charges can be transferred from the graphene to the molecule which in this case acts as an acceptor (**Figure 84**).

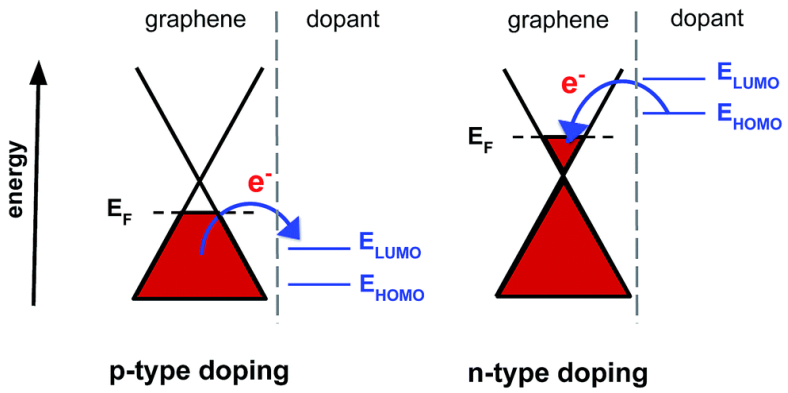

***Figure 84**: Representation of p- and n-doping of graphene. Next to the graphene band diagram, the energy diagram of the electron donor or acceptor is shown. (taken from ref* 234*).*

Electrical[231] and chemical[234,235] doping are well known methods that affect the optical properties of graphene based materials; in n-type doped graphene, or adsorption of molecules with electron-donating groups, the G band hardens and narrows with increasing doping, analogous to the trend seen in graphene doped via the field effect while at high doping, beyond those accessible by the field effect, the G peak strongly softens and broadens[236]; in p-type doped graphene, or adsorption of molecules with electron-withdrawing groups, it upshifts and softens.[232] In our system charge transfer can occur from photoexcitated electrons from the quantum dots into the graphene (or vice versa), hence the Raman features of the GNFs are expected to potentially show similar modification as in the case of doping.

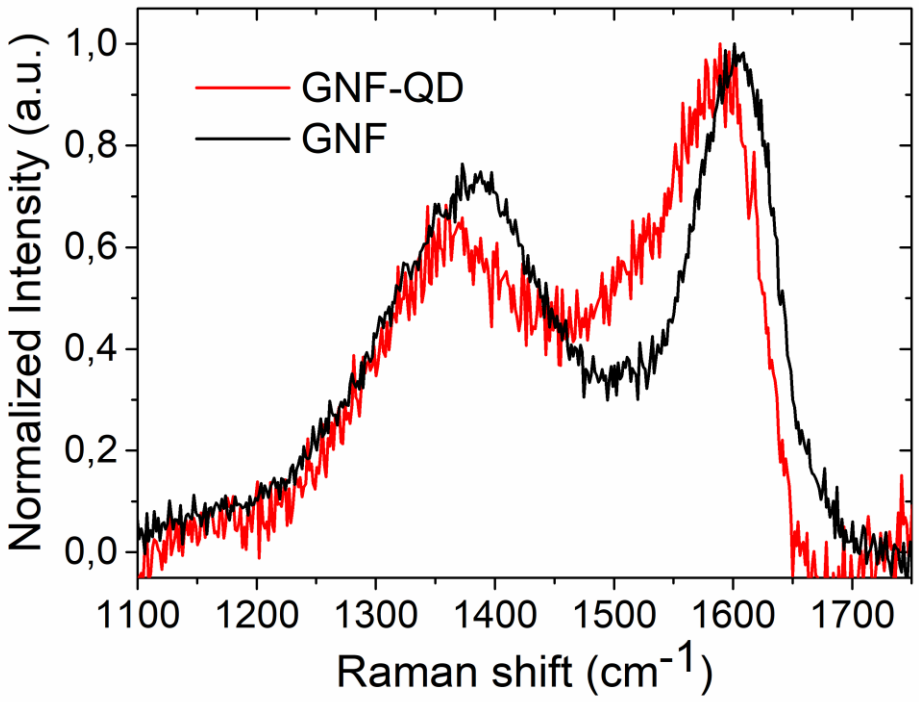

***Figure 85**: Raman spectra of pristine graphene nanoflakes (black) and GNF-QD hybrids (red).*

Figure 85 shows the characteristic D and G band for the pristine graphene (black curve) at 1387 and 1604 cm^{-1} respectively: The G peak corresponds to the high frequency E_{2g} phonon at the Γ point of the graphene brilloune zone while the D peak is due to the breathing modes of the six atoms ring and requires a defect for its activation. The G and D peaks are also presented in the spectrum of the hybrids (**Figure 85** red curve) but the D peak is down shifted by 18 cm^{-1} while the G peak is down shifted by 15 cm^{-1}.

The observed down shift of the G and D bands of the GNFs compared to the pristine graphene indicates that the electronic levels in graphene are perturbed by the presence of the QDs, suggesting a strong coupling between the two nanomoieties.[237] This confirms the nature of the covalent bond, as only a strong overlap of electronic orbitals can cause such a perturbation which are not expected for weak or electrostatic interactions.[203,238]Moreover, a down shift of the features can be ascribed to electron transfer from the photoexcited QD to the nanoflakes, as previously observed for graphene[232,233] and single walled carbon nanotubes doped with electron donor compounds[239] which transfer electrons to the carbon π* states reducing the energy

required for the Raman transitions. These founding, in agreement with the time resolved and blinking data, suggests charge transfer events between the QD and GNF as possible deactivation pathways for the QD exited states.

5.3.9 Solar Cell device fabrication and Photocurrent Measurements

In order to exploit the electron transfer process occurring at the QD-GNF interface, solar cell devices were fabricated where GNF-QD hybrids were employed as active component in TiO_2 photoanodes. The device schematic is shown in **Figure 86** and consists of a TiO_2 electrode, where the GNF-QD hybrids have been deposited, acting as the photoactive anode, and a platinum counter electrode, separated by a Na_2S solution as electrolyte.

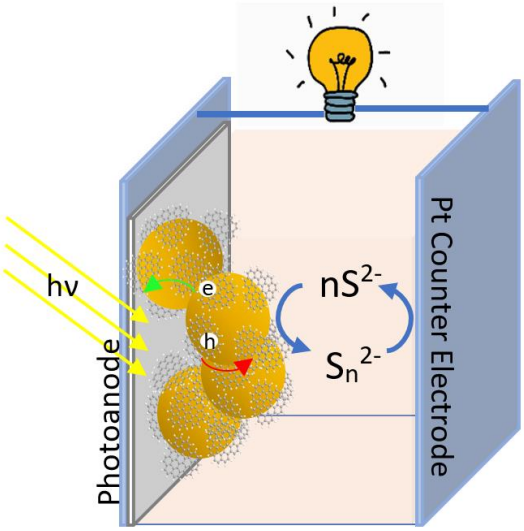

***Figure 86**: Schematic of the Solar cell configuration.*

The working principle of the cell is very similar to a dye-sensitized solar cell:[240]

1) the incident photon is absorbed by the QDs on the TiO_2 surface

2) electrons are excited in the QDs and are injected into the TiO_2 leaving the QDs partially charged

3) the injected electrons in the TiO_2 conduction band are transported through the titania layer to the back contact and reach the counter electrode

4) the oxidized QDs accepts electrons from the redox mediator (S_2^-/S_n^{2-})[211] regenerating the QDs neutrality

$$nS_2^- \rightarrow S_n^{2-} + e^-$$

$$QD^+ + e^- \rightarrow QD$$

5) the oxidized redox mediator diffuses toward the platinum counter electrode to be reduced and complete the cycle.

$$S_n^{2-} + e^- \rightarrow nS_2^-$$

Photocurrent measurements were performed with the solar cells which were exposed to cycles of dark and light of 20 seconds, and it was observed that the photocurrent response, when the TiO_2 was sensitized with our GNF-QD hybrids compared to only QDs, increased by more than 3 times as shown in **Figure 87**. One of the key steps for the efficient work of the solar cell is the charge extraction process from the QDs into the TiO_2 and in the presence of the GNFs increases the extent of this process providing higher generated currents compared to the QD-only device, as previously reported for similar graphene based devices[226,241,242] as well as for C60[243] and CNTs devices.[118]

As a control experiment, solar cells were prepared where, first a GNF layer was deposited on the TiO_2 anode, followed by a deposition of a QDs layer (blue curve in Figure 87). In this case, no significant variations of the photo-generated current was observed compared to the devices with only QDs. This indicates that in the absence of a covalent bond between the two components the electronic coupling is not strong enough to enhance the charge extraction from the QDs, resulting in no improvement in the generated photocurrent.

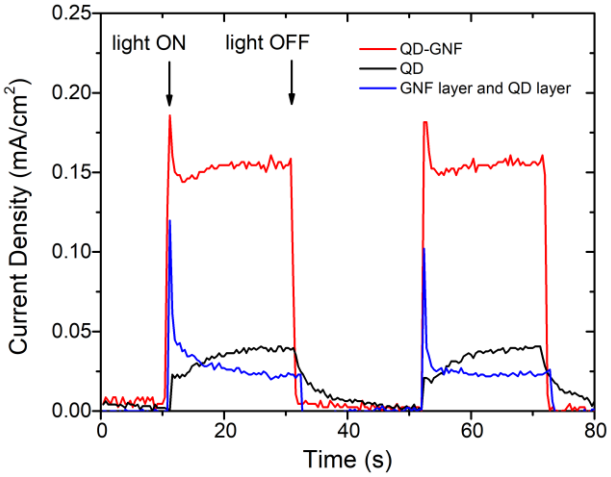

***Figure 87**: Photocurrent response to on/off illumination cycles of the fabricated solar cells using QD (black), GNF-QD hybrids (red) and for devices fabricated by depositing first a layer of GNF and then a layer of QD (blue). In all cases the same amount of QD or GNF (in the case of the red and blue carve) were used in the device fabrication.*

5.4 Conclusions

In conclusion, a facile and green assembly strategy was presented for the formation of GNF-QD nanohybrids in aqueous solution, where graphene nanoflakes have been covalently attached to quantum dots. Photoluminescence studies of the GNF-QD hybrids in solution and on surface with single particle control, show evidence of strong coupling between the two nanomoieties, suggesting that a charge transfer mechanism is responsible for the deactivation of the excited QDs. This was further explored by Raman spectroscopy, which confirmed electron injection processes from the excited QD into the graphene. Finally, we exploited the charge transfer process in the GNF-QD hybrids in solar cell devices that exhibited improved photocurrent compared to the QDs only based devices.

To the best of our knowledge this is the first fully aqueous assembly of graphene-QD hybrids with evidence of charge transfer process at the single nanohybrid level, where a further implementation in a solar-cell device showed improved photocurrent response. Future challenges will focus on the development of the device in order to improve its performances through the use of different electrolytes and the fabrication of solid-state solar cells.

6 GRAPHENE ELECTRODE-QD

6.1 Introduction

Graphene's high temperature stability, its extreme thinness (single atomic layer), the possibility to anchor molecules through covalent or non-covalent immobilization[244] and the integration with the already established silicon based electronic[245] are all characteristics that make graphene the ideal candidate for a wide range of applications including transistors,[246] sensors,[247] and solar cells.[226] In particular, graphene is a very promising material as a nanoelectrode for electronic devices not only because it could replace the usually more expensive metals, but also because a full control over the generated gap between graphene sheets has been achieved up to nanometer sizes.[248]

The advantage of controlling nanogap between electrodes relies on the ability to tune the gap dimensions tailoring its size to accommodate even single molecules or small particles of the appropriate size bridging the two electrodes. A typical configuration for graphene patterned electrodes is shown in **Figure 88**, where the graphene sheets are deposited on silicon substrates and patterning of metal electrodes enables electrical contact.

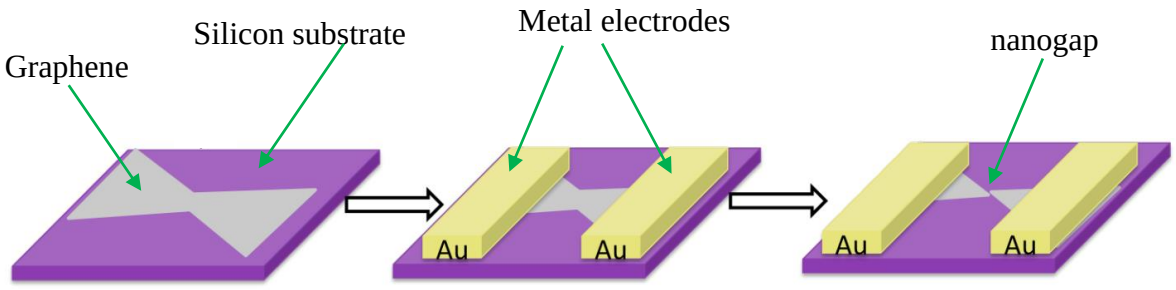

***Figure 88**: Schematic for the patterning of graphene electrodes on silicon for the generation of nanogaps. Electrical contact is ensured through patterning of metal electrodes.*

Different strategies have been used for the development of graphene based molecular electronic devices where molecules are immobilized in the nanogap both in a covalent

and non-covalent strategy: Bouilly et al[249] connected nanoscale graphene gaps terminated with carboxylic acid groups with diamine molecules via covalent bond formation (**Figure 89**c), while other approaches involve the immobilization of molecules between graphene electrodes through non-covalent interactions.[250] In this approach the connecting molecule is characterized by a core unit which allows the current flowing through the device and extended conjugated "arms", acting as anchoring groups, that allow the binding of the molecule to the graphene plane through π-π staking (**Figure 89** a and b).

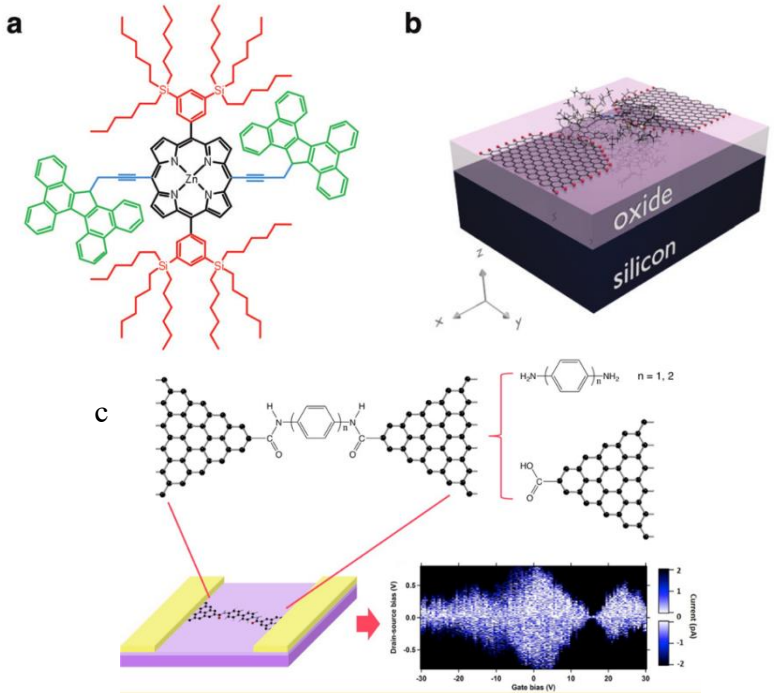

Figure 89*: Schematic of two graphene based molecular electronic devices where single molecules are immobilized into the graphene nanogap: (a) schematic of a molecule characterized by a core unit which allows the current flowing through the device and extended con conjugated "arms" which can form non-covalent (taken from ref* 250*) interaction with the graphene (b) and (c)covalent (taken from ref* 249*) immobilization of molecule between graphene electrodes through amide bond formation.*

Nevertheless, it is still a challenge to investigate what kind of chemical groups are generated when a graphene nanogap is formed and therefore what kind of chemical reactions can be used to covalently tether molecules on graphene nanoelectrodes. The major issue in the individualization of the chemical groups at the nanogap, as well as at

the graphene edges, is represented by the limited spatial resolution of the conventional techniques used, such as FTIR or Raman, which are normally performed in solution or powder: the necessity to investigate specific areas of the graphene layers/electrodes, namely the confined region where the nanogap is generated, and not the entire surface represents a challenge.

In this chapter a selective approach is presented to investigate the chemical groups existing at the nanogap, generated by electroburning, and at the edges of graphene electrodes on surface. This strategy involves the use of quantum dots with amino groups on their surface which were used as anchoring groups to chemically bind the nanoparticles to specific functional groups present on the graphene. Even if in all cases QDs with amino groups on the surface were employed, a selective reaction for each chemical group investigated was carried out towards the attachment of QDs to only carboxyl groups (COOH), only aldehyde groups (CHO) or solely to hydroxyl groups (OH), which are all expected to be present on the graphene edges. After the functionalization, the electrodes were imaged via AFM allowing to locate the QDs and hence identify the chemical groups for the specific reaction that was carried out, as shown in the schematic of the approach in **Figure 90**.

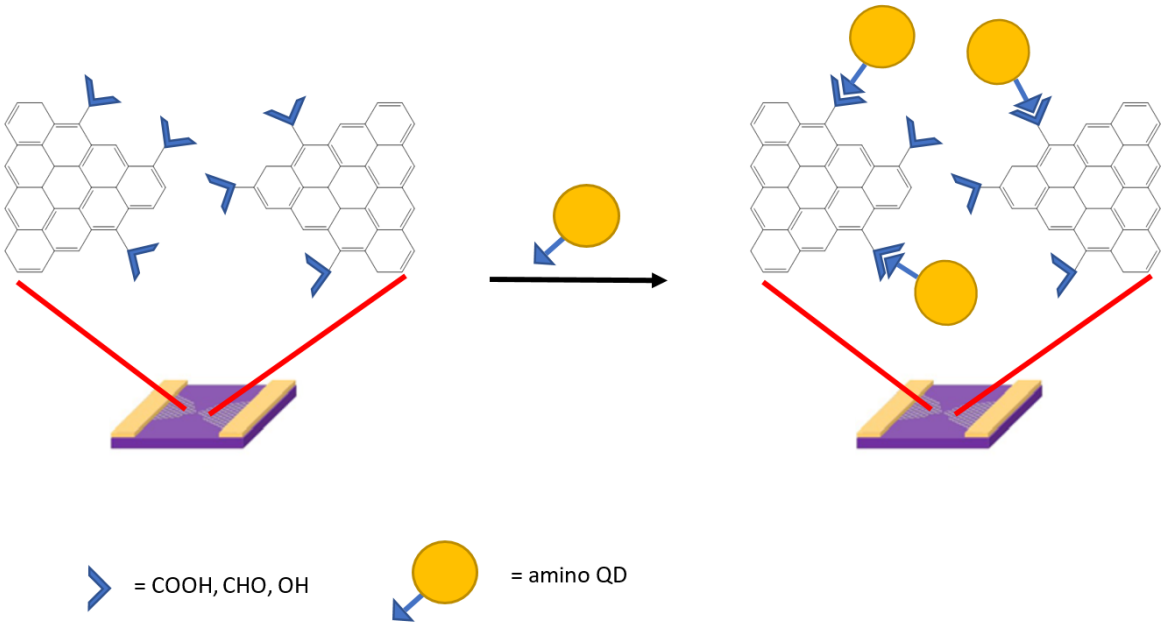

***Figure 90**: Schematic of the strategy to covalently attach QDs to different chemical groups (carboxyl, aldehyde, hydroxyl) which are expected to be present on the graphene electrode edges and at the nanogap.*

Through this approach, single QDs can be spotted via AFM identifying the nature and the location of the chemical groups to which they are attached providing a mini library of the chemical functionalities available and hence the chemical reactions that can be carried out on graphene for further functionalization.

6.2 Fabrication of Graphene Electrodes

Graphene electrodes were fabricated by Dr Jan Mol's group at the University of Oxford, through electroburning methods. This approach relies on the current induced breakdown of graphene. The size of the nano-gaps can be controlled by feedback-controlled electroburning[251] where a voltage (V) ramp is applied to the graphene, while the current (I) is continuously recorded. The variations in the conductance ($G= I/V$) are monitored with a feedback condition which is set at a given point after the current drops. Upon the occurrence of such a drop, the voltage is swept back to zero and the process is repeated until the resistance exceeds the set value[252] (**Figure 91**).

Figure 91 shows also the device fabrication process which involves the depositing of a single CVD grown layer graphene on a pre-patterned silicon chip using electron beam lithography and metal evaporation. After the single layer graphene (SLG) is transferred onto the metal electrodes it is patterned into notched ribbons by exposing a negative resist using electron beam lithography followed by oxygen plasma etching.

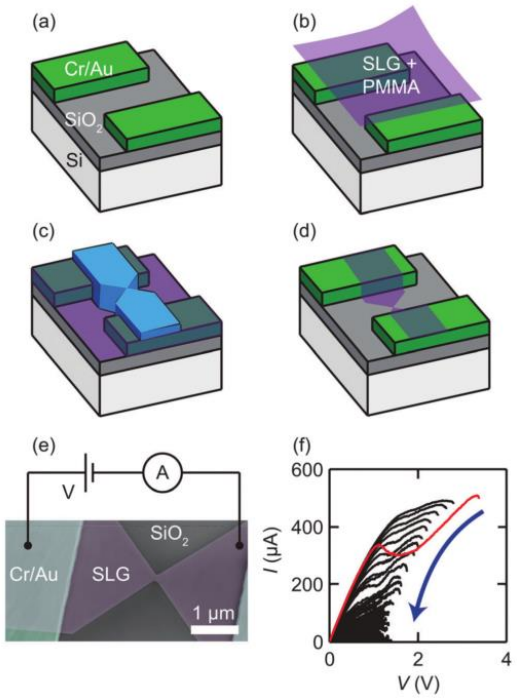

Figure 91*: (a–d) Schematics for the fabrication process of the devices. (e) Scanning electronmicrograph of a single layer graphene (SLG) notched ribbon between two Cr/Au contacts. (f) Current–voltage (I–V) traces recorded during the feedback-controlled electroburning. (taken from ref* 251*).*

The *I–V* traces measured after the electroburning process are characteristic of transport through a single tunnel junction. The size of the nanogap (*d*) can be estimated by fitting the *I–V* traces to a simplified Simmons model:[248,253,254]

$$j \approx \frac{e}{2\pi h d^2}\left[(\varphi - \mu_L)e^{-2d\frac{\sqrt{2m(\varphi-\mu_L)}}{\hbar}} - (\varphi - \mu_R)e^{-2d\frac{\sqrt{2m(\varphi-\mu_R)}}{\hbar}}\right]$$

where ϕ is the average barrier height assuming the work functions of the left and right electrodes are the same, *d* is the barrier width, μ_L and μ_R are the chemical potentials of the left and right electrodes, m is the effective electron mass

6.3 Chemical Reactions

6.3.1 Introduction

Different chemical coupling reactions were employed to explore the presence of specific chemical groups: carboxylic groups (COOH), or hydroxyl groups (OH), or aldehyde groups (CHO) on the graphene nanogaps. AFM was employed in order to image the samples before and after the chemical reaction occurred: the presence of QDs at specific locations on the graphene surface (e.g. the edges, the nanogap), would indicate the successful functionalization strategy: see **Figure 90**.

A typical AFM image of a graphene electrode is shown is **Figure 92** and it can be noticed that close to the notched region, the graphene is much cleaner compared to regions further away. This is an indication of residual resist removal from current annealing during the electroburning process.[251]

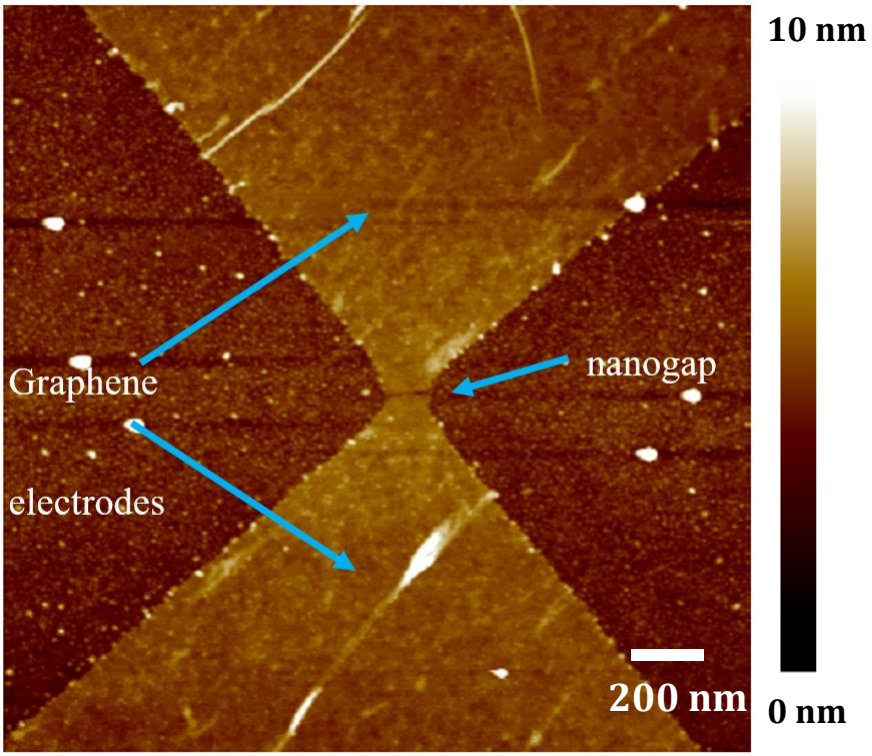

***Figure 92**: Typical topography AFM image of the graphene electrodes employed.*

For all reactions amino functionalized QDs were used: CdS,Se/ZnS core/shell QDs with amine groups on the surface (ocean nanotech) to check the presence of carboxyl groups

through EDC/S-NHS coupling, aldehyde groups through reductive amidation reaction, and hydroxyl groups through DSC coupling and Mannich reaction.

6.3.2 EDC/S-NHS Coupling for the Identification of Carboxyl Groups

In order to check the presence of carboxylic groups an EDC/S-NHS mediate amidation reaction has been performed. This reaction involves the formation of an amide linkage made by the condensation of a primary amine on the quantum dots surface with a carboxylic acid group on the graphene layer: see **Figure 93**. The mechanism for the EDC/S-NHS mediated amidation reaction has been already described in Section 3.2.1.

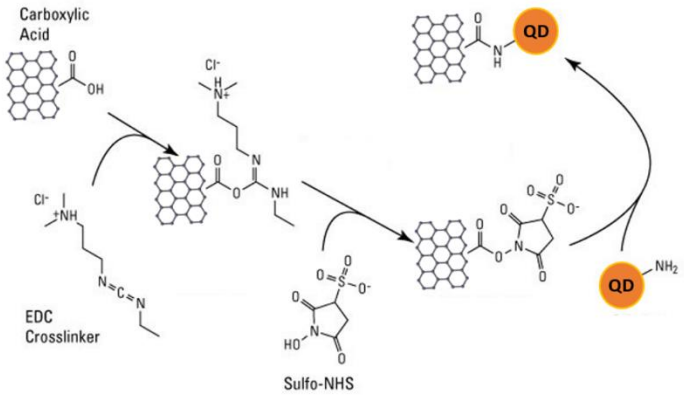

***Figure 93**: Mechanism for the EDC/S-NHS reaction coupling to immobilize amino terminated QD to carboxyl groups on the graphene highlighting the various intermediate compounds.*

6.3.3 Reductive Amidation Reaction for the Identification of Aldehyde Groups

In order to check the presence of aldehyde groups a reductive amidation was carried out, which involves the formation of a Schiff base intermediate between an aldehyde group on the graphene and a primary amine on the quantum dots surface followed by chemical reduction through sodium cynobohydride leading to the formation of a secondary amine: see **Figure 94**.

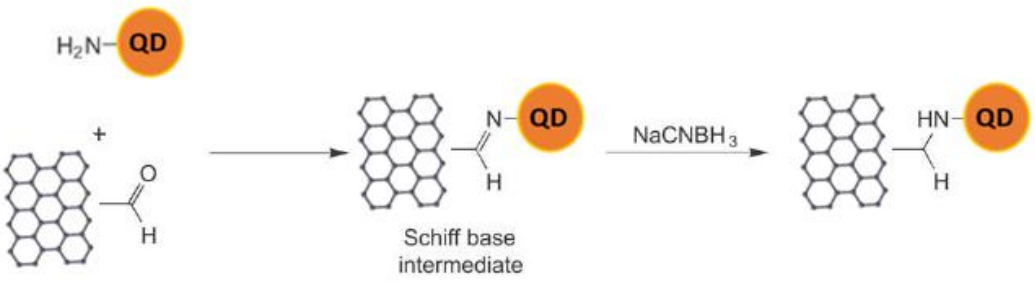

***Figure 94**: Schematic for the reductive amidation reaction to immobilize amino terminated QD to aldehyde groups on the graphene.*

Immobilization by reductive amination of amine-containing biological molecules onto aldehyde-containing solid supports has been previously reported:[255] aldehydes and ketones can react with primary amines to form imines or Schiff bases, a compound with a carbon nitrogen double bond (see **Figure 95**).

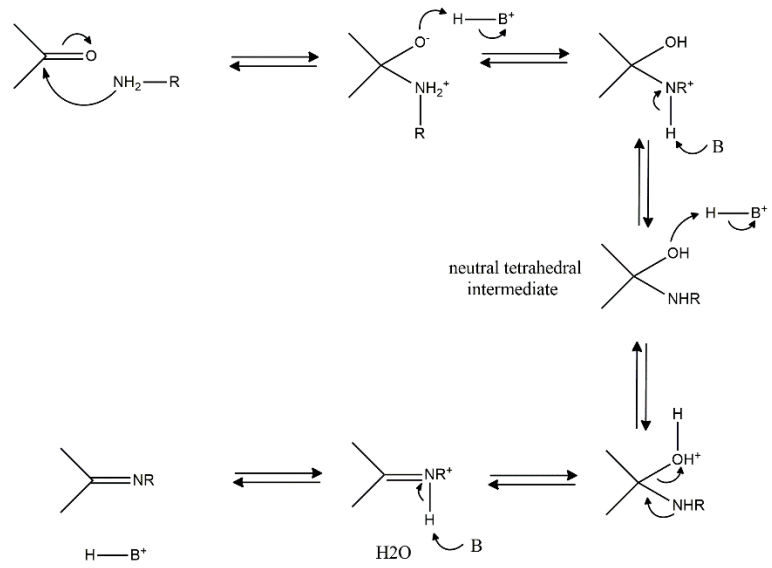

***Figure 95**: Schematic of the formation of a Schiff base.*

The Schiff base formation involves the addition of an amine to an aldehyde or ketone which is overall a nucleophilic addition-elimination reaction: nucleophilic addition of an amine to form an unstable tetrahedral intermediate, followed by elimination of water,[144]

as shown in **Figure 95**. A Schiff base is a relatively labile bond that is readily reversed by hydrolysis in aqueous solution because there are two groups that can be expelled from the tetrahedral intermediate even if the equilibrium favours the nitrogen protonated intermediate since the nitrogen is more basic than the oxygen.

An import factor in the formation of Schiff bases is the pH, because there must be sufficient acid present to protonate the tetrahedral intermediate so that water rather than the more basic OH- is the leaving group. On the other hand, if the pH is too low all the amine groups will be protonated resulting in not being anymore nucleophiles that will not react with carbonyl groups. The optimum pH for the reaction is basic, although good yield can be realized from pH 7 to 10, at higher pH (9–10) the formation of the Schiff bases is more efficient, and the yield of conjugation or immobilization reactions can be dramatically increased.[144]

A higher formation of Schiff bases is obtained at alkaline pH but they are still not completely stable, hence a further step is necessary in order to obtain a much more stable product. To this extent a reductive step is usually performed obtaining a secondary or tertiary amine. A number of reducing agents can be used to convert specifically the Schiff base into an alkylamine linkage such as sodium borohydride or sodium cyanoborohydride with the latter being less aggressive than the former resulting in a milder reaction with less side reactions towards other possible chemical groups; moreover, sodium cyanoborohydride has a high specificity toward the Schiff base structure and will not affect the original aldehyde groups.

6.3.4 DSC Coupling for the Identification of Hydroxyl and Carboxyl Groups

N,*N*-Disuccinimidyl carbonate (DSC) is the smallest homobifunctional NHS ester crosslinking reagent available and it is merely a carbonyl group-containing two NHS esters.[144] The compound is highly reactive toward nucleophiles and in aqueous solutions, it rapidly will hydrolyze to form two molecules of NHS with release of CO_2. On the other hand, in nonaqueous environments it can react with two amine groups to form a substituted urea derivative with loss of two molecules of NHS, but the reagent can be also used in anhydrous organic solvents to activate a hydroxyl group to succinimidyl carbonate derivative reactive toward amine groups (**Figure 96**). With the same mechanism disuccinimidyl carbonate (DSC) can be used to activate amino and carboxy groups other

than hydroxyl groups to form asymmetric ureas and carbamates respectively, upon reaction of the activated reagents with primary amines, hence DSC is not a specific activating agent for hydroxyl groups,[256] but also for COOH groups. In this regard, DSC-activated hydroxylic compounds can be used for conjugation with an amine-containing molecule to form a stable derivative. The linkage created from this reaction is a urethane derivative or a carbamate bond, displaying good stability.[257]

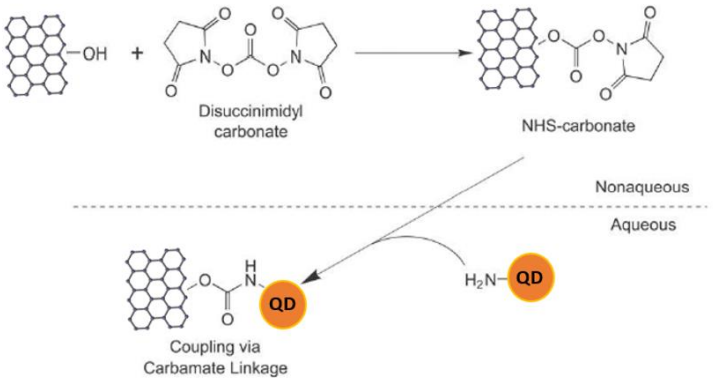

***Figure 96**: Schematic of the DSC coupling reaction to immobilize amino terminated QD to carboxyl and hydroxyl groups on the graphene.*

6.3.5 Mannich Type Reaction for the Identification of Hydroxyl Groups

The Mannich reaction is a classical method for the preparation of β-amino ketones and aldehydes and in practice in this kind of reaction enolizable aldehydes or ketones serve as the CH-acidic substrate.[258] The most common strategy is to heat up the carbonyl compound with formaldehyde and an amine in a protic solvent, allowing the formation of an iminium intermediate which can react with the enolic form of the ketone, as shown in **Figure 97**.

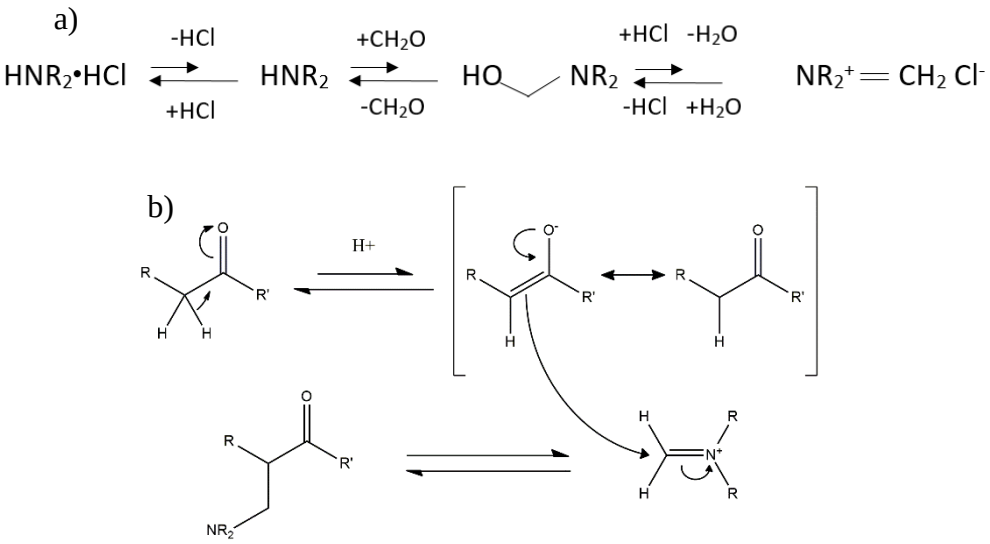

***Figure 97**: Mechanism for the formation of the iminium intermediate (a) and mechanism of the Mannich type reaction (b).*

Mannich type reactions have been widely used to modify proteins at the tyrosine residue with a three component coupling reaction under mild conditions[259] (**Figure 98**): here the aldehyde may participate in a condensation reaction with an amine compound and a substance containing a sufficiently-active hydrogen, yielding an alkylated derivative that effectively crosslinks the two molecules through the carbonyl group of the aldehyde.

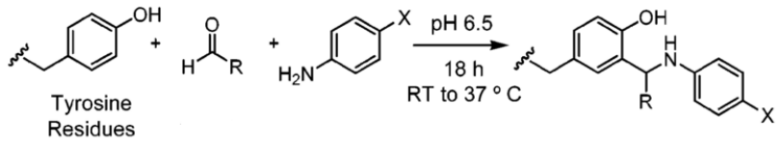

***Figure 98**: Mannich type reaction on a tyrosine residue. (taken from ref* 259*).*

For the specific case of graphene, the reaction scheme is illustrated in **Figure 99** where the reaction consists of the condensation of formaldehyde with the amine groups on the QD surface forming the iminium intermediate which can then react with the enolic form of the deprotonated OH group on the graphene.

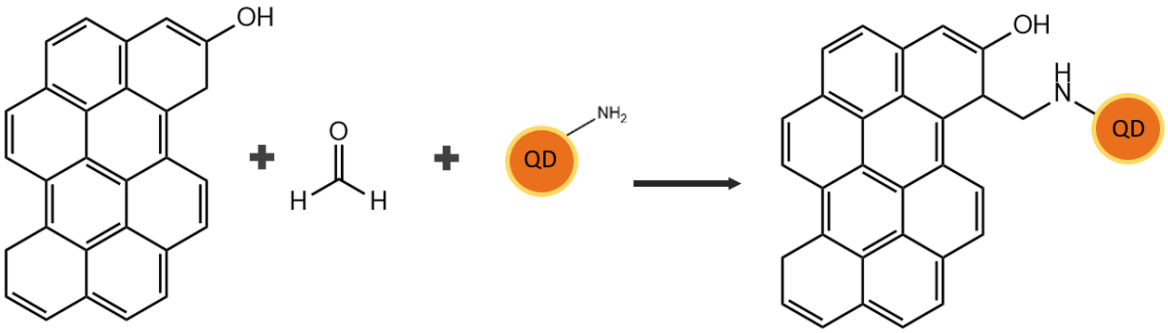

***Figure 99**: Schematic of the Mannich type reaction for the attachment of amino terminated QD to hydroxyl group on the graphene.*

6.4 Results

In order to verify the covalent attachment of the QDs, the same electrode was imaged via AFM before and after each coupling reaction, and the two images were compared. AFM images were collected for more than 10 electrodes for each reaction performed.

The EDC/S-NHS reaction was carried out to investigate the presence of carboxyl groups (COOH). **Figure 100**a and c show the clean electrodes before the coupling where no particles are identified except for small features which cannot be misled for QDs as their size is between 2 and 3 nm hence smaller than the average QD size (7 nm). **Figure 100** b and d show the electrodes after the coupling procedure and QDs can be easily spotted along the edges of the graphene electrode as long as on the gap and on the internal areas as indicated by the arrows. The QDs were found to cover homogeneously the entire surface of the electrodes preferentially as small aggregates.

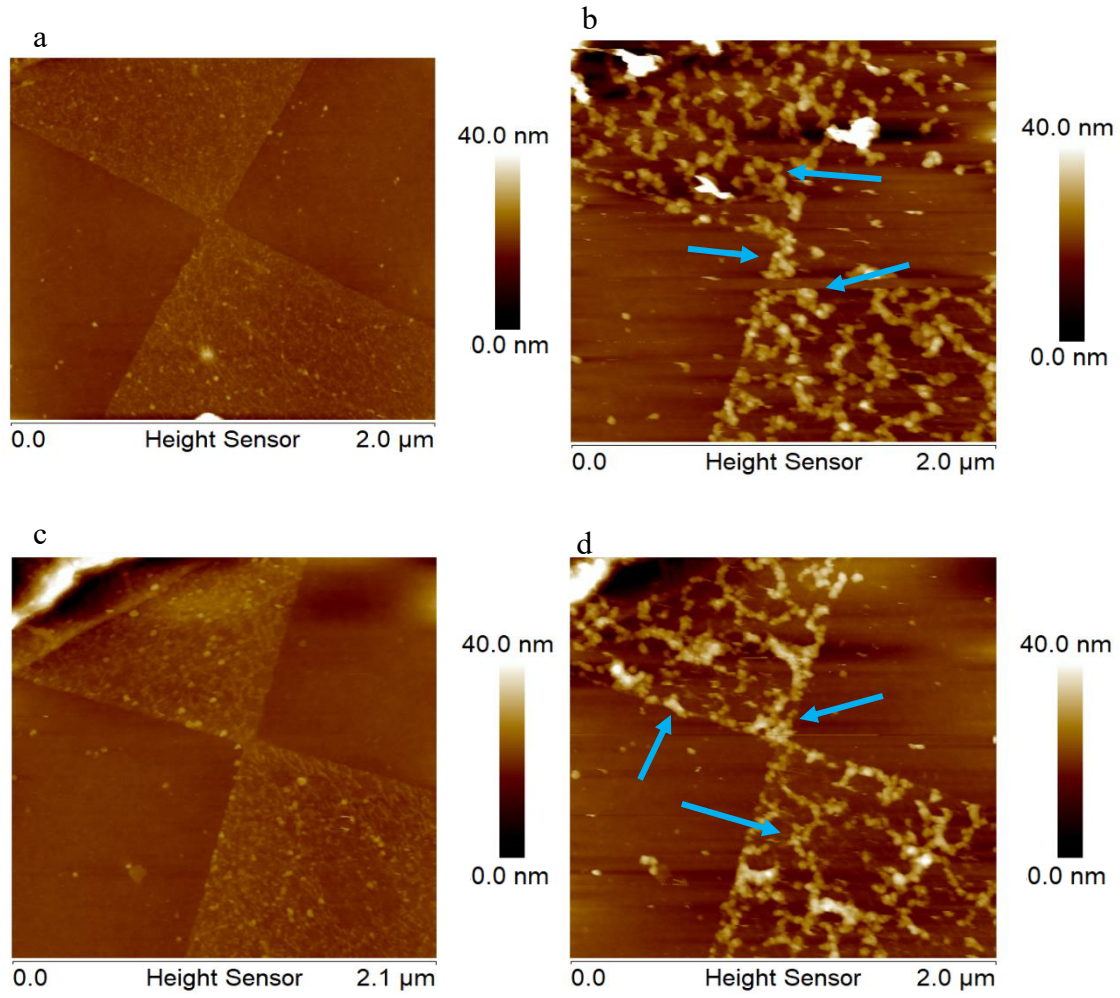

***Figure 100**: Topography AFM images of graphene electrodes before (left) and after (right) functionalization with QDs through EDC/S-NHS coupling reaction. Figures in the same rows a-b, c-d are AFM images of the same electrode. Arrows indicate the attached QD.*

The AFM topographical images of the electrodes before and after the reductive amidation reaction for the identification of aldehyde groups (CHO) are shown in **Figure 101**. By comparing the two images the QDs can be easily identified as indicated by the arrows. Also in this case QDs are present at the edges of the graphene, on the nanogap and also on the inner plane but in this case QDs are distributed more equally on the electrode surface with fewer aggregates. It was speculated that in this case less CHO groups are expected on the graphene compared to the COOH groups hence sparser and less aggregated QDs are observed.

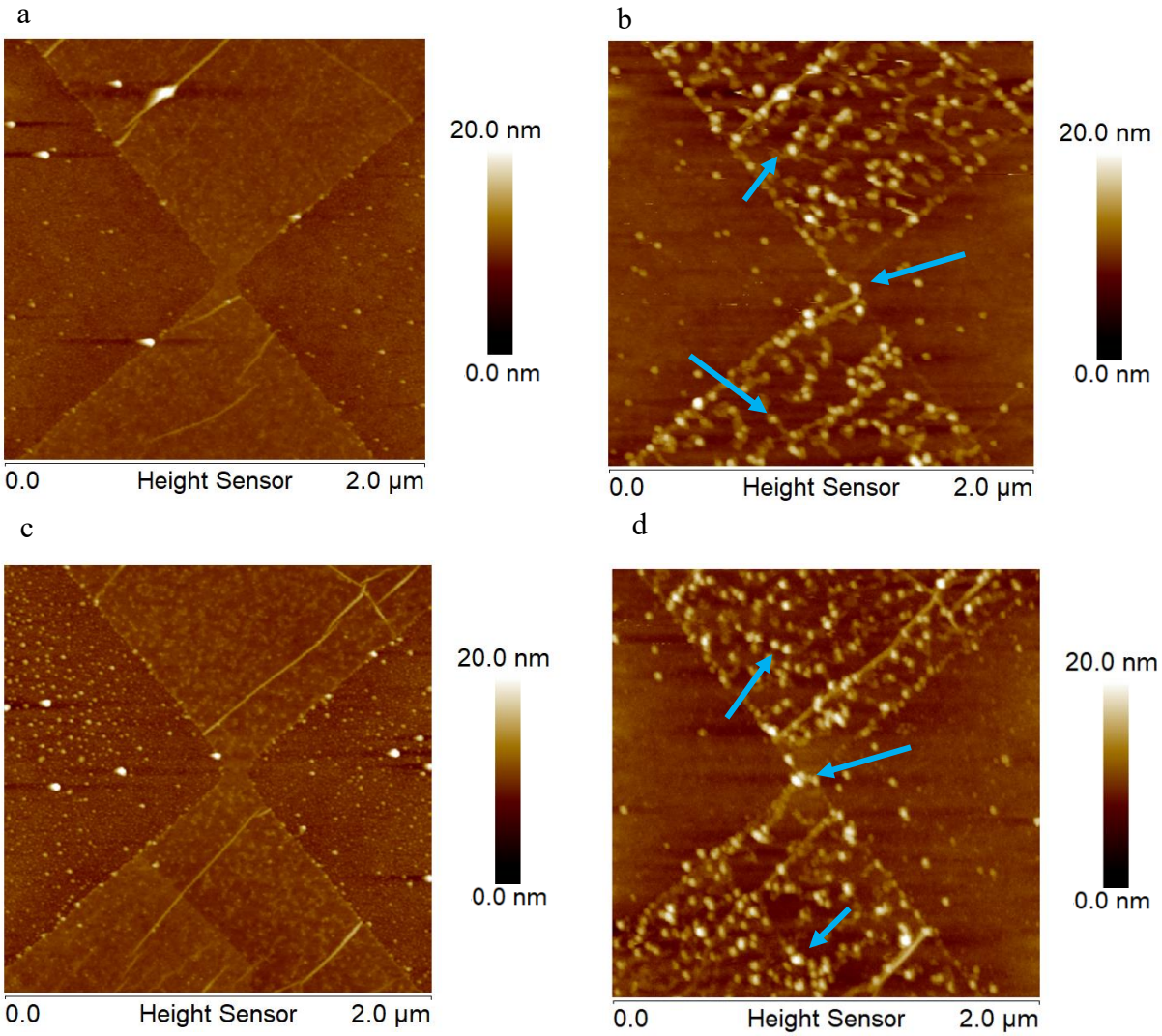

***Figure 101**: AFM images of graphene electrodes before (left) and after (right) functionalization with QDs through reductive amidation reaction. Figures in the same rows a-b, c-d, e-f are AFM images of the same electrode. Arrows indicate the attached QD.*

Figure 102 shows AFM images before (left) and after (after) the DSC coupling reaction of amino QD for the identification of hydroxyl and carboxyl groups. By comparing the two images the QDs can be easily identified, as indicated by the arrows, and were found mainly at the edges of the graphene electrodes and also in small aggregates on the inner parts.

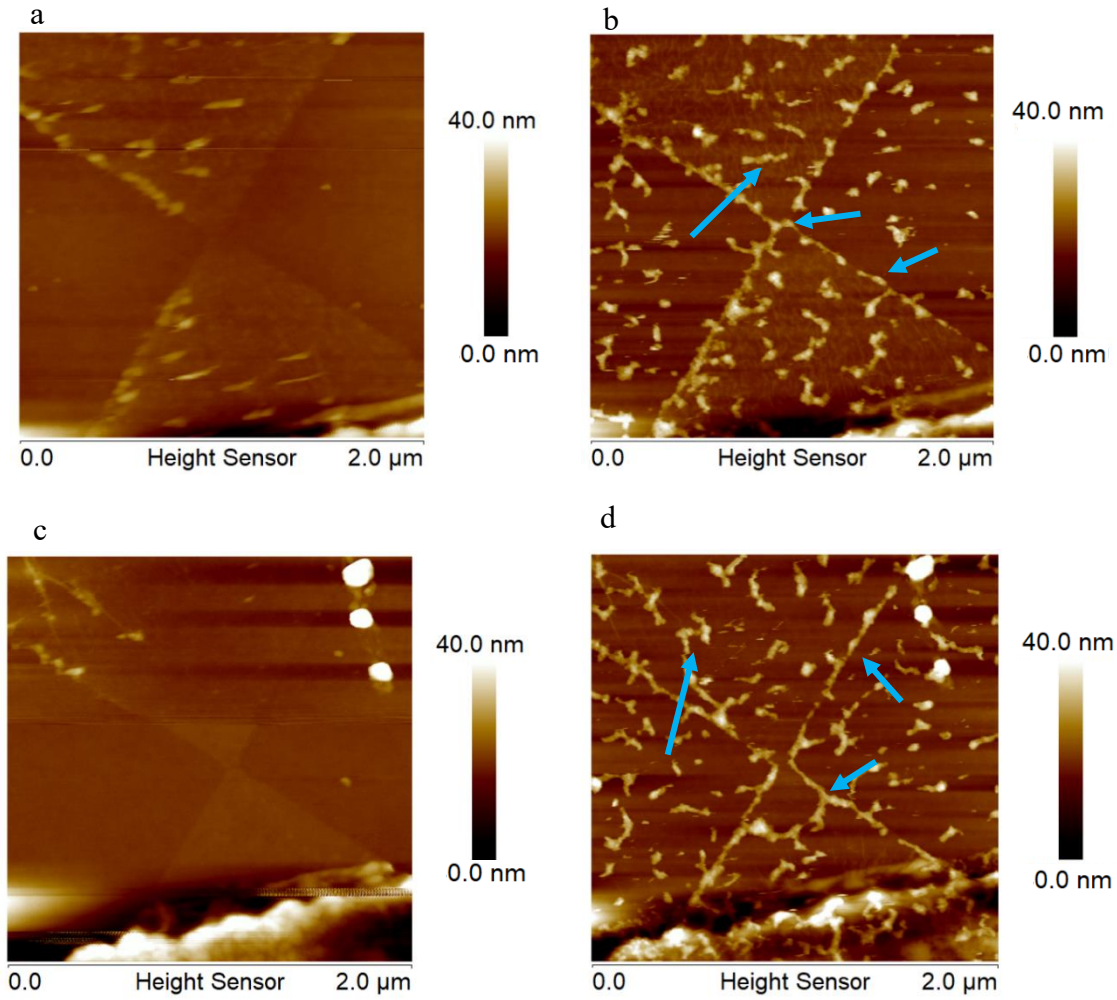

***Figure 102**: Topography AFM images of graphene electrodes before (left) and after (right) functionalization with QDs through DSC coupling reaction. Figures in the same rows a-b, c-d are AFM images of the same electrode. Arrows indicate the attached QD.*

Figure 103 shows the AFM images of the same electrode before and after the Mannich reaction was carried out, for the identification of hydroxyl groups. In this case, only in very few cases QDs were found attached on the gap and sometimes on the edges, while no QDs were observed on the basal plane of the electrodes.

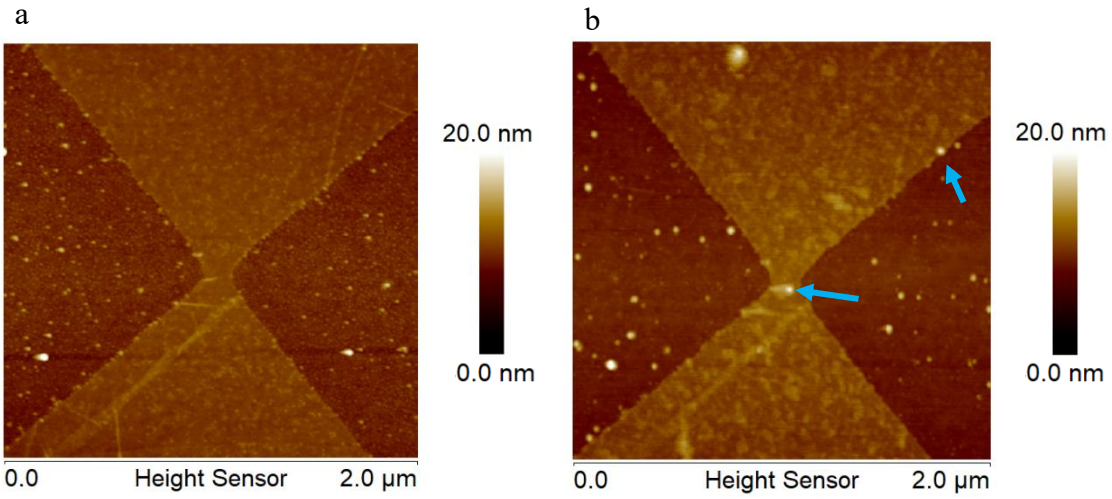

***Figure 103**: Topography AFM images of the same graphene electrode before (left) and after (right) functionalization with QDs through Mannich type reaction. Arrows indicate the attached QD.*

Possible explanation for the lack of attached QD performing this reaction can be the low yield of the reaction itself as well as the scarcity of active hydrogen atoms in α position to the hydroxyl group undergoing the functionalization. This is a necessary requirement for the Mannich reaction to take place and it can only be satisfied under a precise graphene configuration. **Figure 104** shows the two possible configurations of graphene edges,[260,261] namely armchair (a) and zig zag (b), highlighting how only in an armchair configuration there are active hydrogen in α position to the hydroxyl group and hence only in this edge configuration a Mannich type reaction can occur. It was speculated that the majority of the graphene edges are likely to have a zig zag structure hence making impossible for the Mannich reaction to occur, that could explain why no QDs are spotted on the electrodes once the reaction has been carried out.

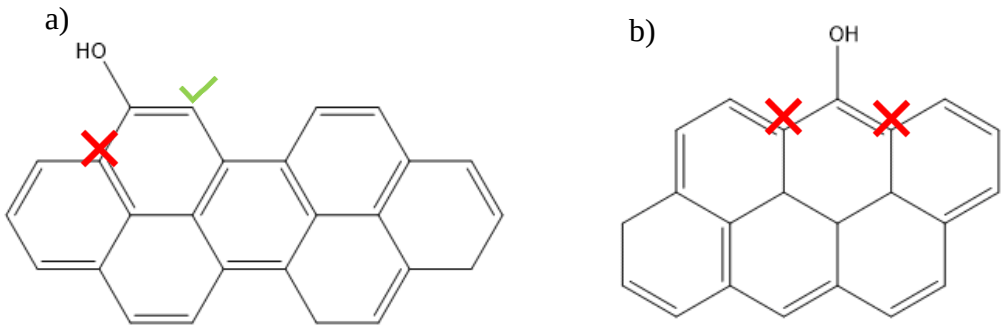

***Figure 104**: Possible configurations of graphene edges namely armchair (a) and zig zag (b). The green mark shows the carbon with an active hydrogen, in α position to the OH, available for the Mannich reaction while the red crosses indicate the carbons in α position to the OH group were the Mannich reaction cannot occur.*

6.5 Conclusions

In this chapter a relatively facile way is presented to investigate some of the chemical groups present at the edges of graphene electrodes through the immobilization of amino functionalized QDs which were selectively and specifically attached to carboxyl, aldehyde and ketones, hydroxyl groups. Once the selective reaction was carried out electrodes were imaged via AFM allowing the individualization of the dots hence the chemical group targeted by that specific reaction. From the AFM topography images there is evidence of attachment of QDs for the EDC/S-NHS coupling, DSC coupling and reduction amidation reaction which confirm the presence of carboxy groups (COOH), hydroxyl groups (OH) and aldehyde groups (CHO) onto the graphene electrodes.

QDs can be found at the edges of the graphene electrode and around the gap area where there is the higher concentration of defects. But QDs were also attached to the inner part of the electrodes. This can be due to both the presence of defects on the inner plane of the electrodes but more likely their presence can be ascribed to unspecific bonding to the left-over photoresist which might not have been completely removed during the cleaning procedure. This is also suggested by the fact that in few cases, as it can be seen from the AFM images, pristine electrodes show small features even if no functionalization has been carried out. A different situation appears in the case of the Mannich type reaction where few QDs or no QDs at all were found attached on the graphene; this is probably due to the zig zag configuration of the graphene edges which does not allow this reaction

to occur. The knowledge of the chemical groups on graphene is of uttermost importance to understand the chemical reactions that can be performed for the tethering of molecules and nanoparticles allowing further graphene functionalization and device implementation. Chemical reactions can be used to attach the desired molecules or particles to the carboxy groups (COOH), hydroxyl groups (OH) and aldehyde groups (CHO) onto the graphene electrodes as their presence has been confirmed by our experiments. Potential different approaches to investigate the edges of graphene electrodes, not only in terms of functionality but also structure, would be high resolution TEM,[262–266] as well as STM.[267–269] These techniques provide a direct evidence of the chemical functionalities and defects on the graphene sheet.

7 CONCLUSIONS AND FUTURE CHALLENGES

The development of functional heterostructures is central in the field of nanotechnology for the design of novel optoelectronic devices. In particular organic-inorganic hybrids have emerged as a promising class of functional materials where size related effects and the combined characteristics of the different components result in new functionalities and electronic properties at the interface.

In this thesis the controlled formation of quantum dots-nanocarbon hybrids is described and the further characterization in solution as well as on surface with single molecule resolution. A water-based approach was developed for the functionalization of carbon nanotubes with quantum dots. A single particle control was achieved where single QDs were attached exclusively at the terminal ends of single-walled carbon nanotubes through covalent bond. Photoluminescence studies were performed both in solution (stationary and time-resolved) and on surface at the single nanohybrid level, showing evidence of electronic coupling between the two nanomoieties. Moreover, the level of control demonstrated here was further investigated in detail via the use of ligands of different length and chemical nature bridging the QDs and the CNTs in the hybrids. This strategy allowed a further control and tunability of the electronic coupling at the organic–inorganic interface for a higher understanding of the energy and charge transfer processes involved. Conjugated linkers with 1, 2 and 3 phenyl rings were employed showing promising results for the tunability of the electronic coupling in QD-CNT nanohybrids: the nature of the linker affects the electronic coupling, with a progressive reduction of lifetimes observed when the number of phenyl rings increases and hence with the increasing degree of conjugation. Nevertheless, the analysis of the decay and the blinking statistics did not allow to elucidate the role played by the linker in the deactivation of the excited QD in the hybrids. The use of alkyl chain as linkers with increasing number of carbon atoms (6 to 12 carbon alkyl chains) resulted in a shortening of both QD lifetimes for all the linkers but no difference was detected regardless of the linker used. This was likely due to the low yield of the coupling reaction (less than 5%) with very few hybrids formed and the

presence of free QDs that covered the PL signal with the impossibility to distinguish the effect of each different linker.

These preliminary studies would suggest that most likely both energy transfer and charge transfer are competitive and simultaneous mechanisms involved in the deactivation of the QD excited state when attached to CNT bridged with different linkers and even though it was not possible to discriminate the effect of the nature of the single linker, our findings were useful for the development of the assembly strategy and photophysical characterization of the DNA-linker hybrids. In this case, DNA of differing length, from 10 bp to 30 bp, was employed as a molecular ruler in the one to one QD-CNT hybrids. Photoluminescence studies in solution and on surface, with single particle resolution, demonstrated a distance dependence electronic coupling indicating that charge transfer becomes the dominating coupling process as the distance between the tubes and the QDs is controllably reduced.

The knowledge developed makes a significant contribution to the fabrication of nanohybrid materials with single-particle control, for solution-processable organic-inorganic heterostructures. Single molecule control is an important feature in the design of novel QD-based optoelectronic and light-energy conversion devices following the ongoing process of downscaling conventional technologies. Further research includes fundamental studies involving the use of carbon nanotubes of single chirality to understand how the nature of the CNT (metallic or semiconductor) affects the electronic coupling. Moreover, a further step towards the integration of such materials into devices would be to increase the yield of the hybrid formation as well as separate the hybrids from free QDs and CNTs in order to obtain high concentrated solution of “pure” hybrids.

Future work, currently ongoing in the Palma group, involves the functionalization of the carbon nanostructures with other nanoparticles such as gold nanoparticles or fluorescent conjugated polymer nanoparticles. This functionalization can be achieved through the techniques developed in this thesis, such as the use of DNA wrapped CNT for the selective functionalization of the terminal ends, the Sulfo-NHS/EDC coupling for the tethering of amino terminated particles or the use of functional groups on the DNA wrapped around the tubes which would allow an extensive side wall functionalization of the tubes.

The approach described in Chapters 3 and 4 could be also used to functionalize both terminal ends of the CNTs each with a different nanoparticle: for example, one terminal

end could be functionalized with a QD and the other with a gold nanoparticle or another QD with a different emission. These nanostructures would allow to study how the coupling between the nanoparticles at the terminal ends is affected by the presence of the CNT (i.e. the chirality, the metallic or semi-conductive nature of the tube as well as its length).

Moreover, the aforementioned nanohybrids can be implemented into devices through immobilization between electrodes. Recently, within the Palma group, a dielectrophoresis technique has been developed to immobilize carbon nanotubes between gold electrodes: DNA wrapped CNTs were functionalized with different, aptamer sequences that were employed as selective recognition elements for specific biomarkers.[270] The same strategy will be used to immobilize CNTs functionalized with quantum dots or nanoparticles and these hybrids could then be employed as photodetectors or photo-transistors, where the CNTs act as transducer and the nanoparticles can work as the active components.

In this regard, another carbon nanostructure was investigated as a potential transducer and nanoelectrode: graphene. In chapter 5 we discussed how we assembled quantum dots-graphene nanoflakes hybrids. Here graphene nanoflakes were employed, characterized by low defects density on the basal plane and a high density of carboxylic groups predominantly/only at the edges that can then act as anchoring groups for the covalent tethering of quantum dots. Evidence of charge transfer between the two nanomoities was demonstrated through stationary and time resolved photoluminescence in solution and on surface with single particle control, as well as through Raman spectroscopy. This was further exploited in the fabrication of photovoltaic cells that exhibit improved photocurrent, compared to the same device with only QDS, due to the graphene electron-acceptor nature witch favours charge extraction processes from the photoexcited QD. Further studies would focus on the optimization of the device fabrication to ensure higher Incident photon-to-current efficiency. Important aspects are the deposition of the material on the electrode to ensure higher loading and a better packing as well as the optimization of the charge re-neutralization of the QD on the anode through a specific designed electrolyte or the implementation into solid state solar cells.

Finally, QDs were covalently attached to graphene electrodes on silicon surface in order to investigate the chemical groups present at the graphene edges as well as on the electrode nanogap. Amino QDs were selectively and univocally attached to carboxyl groups, aldehyde groups and hydroxyl groups which can be found onto the graphene

edges. Atomic force microscopy was employed to image the electrodes before and after the functionalization hence allowing the localization of the nanoparticles and therefore the chemical groups to which they were attached. This strategy resulted in a facile approach to study the chemical nature of the graphene edges overcoming current issues such as the necessity to investigate specific areas of the graphene layers/electrodes and the limited spatial resolution of the conventional techniques.

Future work will take advantage of the demonstrated presence of these chemical groups on the graphene to further explore the graphene covalent functionalization with molecules as well as nanoparticles allowing the development of single molecule devices for optoelectronic applications. In particular, a single QD (or molecule/nanoparticle) could potentially be immobilized in a covalent way in the nanogap bridging two graphene electrodes allowing to carry out fundamental studies on light induced QD-graphene processes at the interface as well as the development of single particle phototransistors and photosensors. By and large, the work presented in this thesis focused on the assembly and characterization of QD-nanocarbon hybrids, contributing to understanding the processes involved. Important challenges remain in terms of morphology, composition as well as control over the interface in order to allow a reliable and scalable introduction of the studied hybrids into actual devices. Single-molecule control over hybrid formation has been achieved and the assembled materials have been integrated into devices showing improved performances suggesting that the methods developed here may facilitate the advancement of new optoelectronic technologies based on QD-carbon nanohybrids.

The formation of nanocarbon-quantum dots hybrids materials presents at the moment several challenging aspects including the control of the interface between the nanomoieties especially for applications that involve charge transfer process, or the control of the morphology and phase composition, as well as the type and quality of carbon nanotubes and their biocompatibility for biological and medical applications. Further factors that strongly influence the performances of nanocarbon-QD hybrids involve the physical properties of the nanocarbon (e.g. metallic vs semiconducting) which affect conductivity but also light absorption and convenience in hybridization.

In this work some of these aspects have been addressed: the interface between nanotubes and QDs have been controlled through the use of different molecular linkers highlighting how the nature of the bridging molecule as well as the distance plays an important role in the electronic coupling between the nano-materials. Moreover, the morphology of the

assembled nanostructures has been controlled with only the terminal ends of CNT being functionalized with a single QD. Additionally, a water-based approach has been developed ensuring a biocompatible and environment friendly methodology.

Some of the most important and crucial aspects for the future development of these new nanohybrids materials for technological applications is to find synthetic strategies to produce materials with reproducible properties and performances. Nanocarbon-QD hybrids have the potential to become next generation functional materials and, in this regard, this work contributes significantly to the development of these hybrids for various applications including nanobiotechnology, energy storage/conversion, catalysis, electronic nanodevices.

8 REFERENCES

1. Waser, R. *Nanoelectronics and information technology : advanced electronic materials and novel devices*. (Wiley-VCH, 2012).
2. Ozin, G. A., Arsenault, A. C. & Cademartiri, L. *Nanochemistry : a chemical approach to nanomaterials*. (Royal Society of Chemistry, 2009).
3. Whitesides, G. M. & Grzybowski, B. Self-assembly at all scales. *Science* **295,** 2418–21 (2002).
4. Sneha, M., Oluwatobi, Samuel Oluwafemi Nandakumar, K. & Thomas, S. *APPLICATIONS OF NANOMATERIALS : advances and key technologies.* (WOODHEAD, 2018).
5. Tiwari, A. & Turner, A. P. F. *Biosensors nanotechnology*. (Wiley-VCH, 2014).
6. Garcia-Martinez, J. *Nanotechnology for the Energy Challenge*. (Wiley-VCH, 2013).
7. Liang, Y., Li, Y., Wang, H. & Dai, H. Strongly Coupled Inorganic/Nanocarbon Hybrid Materials for Advanced Electrocatalysis. *J. Am. Chem. Soc.* **135,** 2013–2036 (2013).
8. Wang, H. & Dai, H. Strongly coupled inorganic–nano-carbon hybrid materials for energy storage. *Chem. Soc. Rev.* **42,** 3088 (2013).
9. Jariwala, D., Sangwan, V. K., Lauhon, L. J., Marks, T. J. & Hersam, M. C. Carbon nanomaterials for electronics, optoelectronics, photovoltaics, and sensing. *Chem. Soc. Rev.* **42,** 2824–2860 (2013).
10. Acquah, S. F. A. *et al.* Review—The Beautiful Molecule: 30 Years of C 60 and Its Derivatives. *ECS J. Solid State Sci. Technol.* **6,** 3155–3162 (2017).
11. Van Noorden, R. Chemistry: The trials of new carbon. *Nature* **469,** 14–16 (2011).
12. Y.-M. Lin *et al.* Wafer-Scale Graphene Integrated Circuit. *Science* **332,** 1294–1297 (2011).

13. Anyuan Cao, Pamela L. Dickrell, W. Gregory Sawyer, Mehrdad N. Ghasemi-Nejhad & Pulickel M. Ajayan. Super-Compressible Foamlike Carbon Nanotube Films. *Science* **310,** 1307–1310 (2005).

14. Xiao, L. *et al.* Flexible, Stretchable, Transparent Carbon Nanotube Thin Film Loudspeakers. *Nano Lett.* **8,** 4539–4545 (2008).

15. Simon, P. & Gogotsi, Y. Materials for electrochemical capacitors. *Nat. Mater.* **7,** 845–854 (2008).

16. Shearer, C. J., Cherevan, A. & Eder, D. Application and Future Challenges of Functional Nanocarbon Hybrids. *Adv. Mater.* **26,** 2295–2318 (2014).

17. Eder, D. Carbon Nanotube - Inorganic Hybrids. *Chem. Rev.* **110,** 1348–1385 (2010).

18. Wallace, P. R. & Ace, P. R. W. The Band Theory of Graphite. *Phys. Rev.* **71,** 622 (1947).

19. J.W. McClure. Diamagnetism of Graphite. *Phys. Rev.* **104,** 666–671 (1956).

20. Novoselov, K. S. *et al.* Two-dimensional gas of massless Dirac fermions in graphene. *Nature* **438,** 197–200 (2005).

21. Novoselov, K. S. *et al.* Electric field effect in atomically thin carbon films. *Science* **306,** 666 (2004).

22. Geim, A. K. & Novoselov, K. S. The rise of graphene. *Nat. Mater.* **6,** 183–191 (2007).

23. Neto, A. H. C., Guinea, F., Peres, N. M. R., Novoselov, K. S. & Geim, A. K. The electronic properties of graphene. *Rev. Mod. Phys.* **81,** 109 (2007).

24. Das Sarma, S., Adam, S., Hwang, E. H. & Rossi, E. Electronic transport in two-dimensional graphene. *Rev. Mod. Phys.* **83,** 407–470 (2011).

25. Partoens, B. & Peeters, F. M. From graphene to graphite: Electronic structure around the K point. *Phys. Rev. B* **74,** 1–11 (2006).

26. Chen, C. . & Robertson, J. Nature of disorder and localization in amorphous carbon. *J. Non. Cryst. Solids* **227,** 602–606 (1998).

27. Dubois, S. M.-M., Zanolli, Z., Declerck, X. & Charlier, J.-C. Electronic properties

and quantum transport in Graphene-based nanostructures. *Eur. Phys. J. B* **72,** 1–24 (2009).

28. Robertson, J. & Reilly, E. P. O. Electronic and atomic structure of amorphous carbon. *Phys. Rev. B* **35,** 2946–2957 (1987).

29. Mathioudakis, C. *et al.* Electronic and optical properties of a-C from tight-binding molecular dynamics simulations. *Thin Solid Films* **482,** 151–155 (2005).

30. Eda, G. *et al.* Blue photoluminescence from chemically derived graphene oxide. *Adv. Mater.* **22,** 505–509 (2010).

31. Luo, Z., Vora, P. M., Mele, E. J., Johnson, A. T. C. & Kikkawa, J. M. Photoluminescence and band gap modulation in graphene oxide. *Appl. Phys. Lett.* **94,** 111909–32146 (2009).

32. Ferrari, A. C. Raman spectroscopy of graphene and graphite: Disorder, electron-phonon coupling, doping and nonadiabatic effects. *Solid State Commun.* **143,** 47–57 (2007).

33. Malard, L. M., Pimenta, M. A., Dresselhaus, G. & Dresselhaus, M. S. Raman spectroscopy in graphene. *Phys. Rep.* **473,** 51–87 (2009).

34. Ferrari, A. C. & Robertson, J. Interpretation of Raman spectra of disordrred and amorphous carbon. *Phys. Rev. B* **61,** 14 295 (2000).

35. Ferrari, A. C. & Basko, D. M. Raman spectroscopy as a versatile tool for studying the properties of graphene. *Nat. Nanotechnol.* **8,** 235–246 (2013).

36. Jorio, A., Dresselhaus, G. & Dresselhaus, M. S. *Carbon Nanotubes: Advanced Topics in the Synthesis, Structure, Properties and Applications*. (Springer US, 2008).

37. Reich, S., Thomsen, C. & Maultzsch, J. *Carbon Nanotubes. Basic Concepts and Physical Properties*. *Angewandte Chemie International Edition* **43,** (2004).

38. Roth, S. & Carroll, D. *One-dimensional metals : conjugated polymers, organic crystals, carbon nanotubes.* (Wiley-VCH, 2004).

39. Guldi, D. M. *et al.* CNT - CdTe Versatile Donor - Acceptor Nanohybrids. *J. Am. Chem. Soc* **128,** 2315–2323 (2006).

40. Hwang, S., Batmunkh, M., Nine, M. J., Chung, H. & Jeong, H. Dye-Sensitized Solar Cell Counter Electrodes Based on Carbon Nanotubes. *ChemPhysChem* **16,** 53–65 (2015).

41. Avouris, P., Chen, Z. & Perebeinos, V. Carbon-based electronics. *Nat. Nanotechnol.* **2,** 605–615 (2007).

42. Joselevich, E. Electronic Structure and Chemical Reactivity of Carbon Nanotubes: A Chemist's View. *ChemPhysChem* **5,** 619–624 (2004).

43. Nanot, S., Hároz, E. H., Kim, J.-H., Hauge, R. H. & Kono, J. Optoelectronic Properties of Single-Wall Carbon Nanotubes. *Adv. Mater.* **24,** 4977–4994 (2012).

44. Samsonidze, G. G. *et al.* The Concept of Cutting Lines in Carbon Nanotube Science. *J. Nanosci. Nanotechnol.* **3,** 431–458 (2003).

45. Mintmire, J. W., Dunlap, B. I. & White, C. T. Are Fullerene Tubules Metallic? *Phys. Rev. Lett.* **68,** 631 (1992).

46. Bachilo, S. M. *et al.* Structure-assigned optical spectra of single-walled carbon nanotubes. *Science* **298,** 2361–2366 (2002).

47. Wei, X. *et al.* Experimental determination of excitonic band structures of single-walled carbon nanotubes using circular dichroism spectra. *Nat. Commun.* **7,** 1–9 (2016).

48. Zhang, Y., Gu, H. & Iijima, S. Single-wall carbon nanotubes synthesized by laser ablation in a nitrogen atmosphere. *Appl. Phys. Lett* **73,** 3827 (1998).

49. Kumar, M. & Ando, Y. Chemical Vapor Deposition of Carbon Nanotubes: A Review on Growth Mechanism and Mass Production. *J. Nanosci. Nanotechnol.* **10,** 3739–3758 (2010).

50. Journet, C. *et al.* Large-scale production of single-walled carbon nanotubes by the electric-arc technique. *Nature* **388,** 756–758 (1997).

51. Jie Liu *et al.* Fullerene Pipes. *Science* **280,** 1253–1256 (1998).

52. Saito, T., Matsushige, K. & Tanaka, K. Chemical treatment and modification of multi-walled carbon nanotubes. *Phys. B Condens. Matter* **323,** 280–283 (2002).

53. Bahr, J. L. *et al.* Functionalization of Carbon Nanotubes by Electrochemical

Reduction of Aryl Diazonium Salts : A Bucky Paper Electrode. *J. Am. Chem. Soc* **123,** 6536–6542 (2001).

54. Kahn, M. G. C., Banerjee, S. & Wong, S. S. Solubilization of Oxidized Single-Walled Carbon Nanotubes in Organic and Aqueous Solvents through Organic Derivatization. *Nano Lett.* **2,** 1215–1218 (2002).

55. Britz, D. A. & Khlobystov, A. N. Noncovalent interactions of molecules with single walled carbon nanotubes. *Chem. Soc. Rev.* **35,** 637 (2006).

56. Fujigaya, T. & Nakashima, N. Non-covalent polymer wrapping of carbon nanotubes and the role of wrapped polymers as functional dispersants. *Sci. Technol. Adv. Mater.* **16,** 024802 (2015).

57. Pochorovski, I. *et al.* H-Bonded Supramolecular Polymer for the Selective Dispersion and Subsequent Release of Large-Diameter Semiconducting Single-Walled Carbon Nanotubes. *J. Am. Chem. Soc.* **137,** 4328–4331 (2015).

58. Vaisman, L., Wagner, H. D. & Marom, G. The role of surfactants in dispersion of carbon nanotubes. *Adv. Colloid Interface Sci.* **128–130,** 37–46 (2006).

59. Wei, B., Guan, P., Zhang, L. & Chen, G. Solubilization of carbon nanotubes by cellulose xanthate toward the fabrication of enhanced amperometric detectors. *Carbon N. Y.* **48,** 1380–1387 (2010).

60. Backes, C., Hauke, F. & Hirsch, A. The Potential of Perylene Bisimide Derivatives for the Solubilization of Carbon Nanotubes and Graphene. *Adv. Mater.* **23,** 2588–2601 (2011).

61. Zheng, M. *et al.* DNA-assisted dispersion and separation of carbon nanotubes. *Nat. Mater.* **2,** 338–342 (2003).

62. Khripin, C. *et al.* High-Resolution Length Fractionation of Surfactant-Dispersed Carbon Nanotubes. *Anal. Chem.* **85,** 1382–1388 (2012).

63. Arnold, M. S., Green, A. A., Hulvat, J. F., Stupp, S. I. & Hersam, M. C. Sorting carbon nanotubes by electronic structure using density differentiation. *Nat. Nanotechnol.* **1,** 60–65 (2006).

64. Tanaka, T. *et al.* Simple and scalable gel-based separation of metallic and semiconducting carbon nanotubes. *Nano Lett.* **9,** 1497–1500 (2009).

65. Liu, H., Nishide, D., Tanaka, T. & Kataura, H. Large-scale single-chirality separation of single-wall carbon nanotubes by simple gel chromatography. *Nat. Commun.* **2,** 309 (2011).

66. Xueying Huang,† Robert S. Mclean, and M. Z. High-Resolution Length Sorting and Purification of DNA-Wrapped Carbon Nanotubes by Size-Exclusion Chromatography. *Anal. Chem.* **77,** 77, 6225–6228 (2005).

67. Tu, X., Manohar, S., Jagota, A. & Zheng, M. DNA sequence motifs for structure-specific recognition and separation of carbon nanotubes. *Nature* **460,** 250–253 (2009).

68. Ao, G., Streit, J. K., Fagan, J. A. & Zheng, M. Differentiating Left- and Right-Handed Carbon Nanotubes by DNA. *J. Am. Chem. Soc.* **138,** 16677–16685 (2016).

69. Palma, M. *et al.* Controlled formation of carbon nanotube junctions via linker-induced assembly in aqueous solution. *J. Am. Chem. Soc.* **135,** 8440–8443 (2013).

70. Monthioux, M. *et al.* Sensitivity of single-wall carbon nanotubes to chemical processing: an electron microscopy investigation. *Carbon N. Y.* **39,** 1251–1272 (2001).

71. Rosca, I. D., Watari, F., Uo, M. & Akasaka, T. Oxidation of multiwalled carbon nanotubes by nitric acid. *Carbon N. Y.* **43,** 3124–3131 (2005).

72. Cheng, Y. C., Kaloni, T. P., Zhu, Z. Y. & Schwingenschlögl, U. Oxidation of graphene in ozone under ultraviolet light. *Appl. Phys. Lett.* **101,** (2012).

73. Geng, H.-Z. *et al.* Effect of Acid Treatment on Carbon Nanotube-Based Flexible Transparent Conducting Films. *J. Am. Chem. Soc.* **129,** 7758–7759 (2007).

74. Peng, X. & Wong, S. S. Controlling nanocrystal density and location on carbon nanotube templates. *Chem. Mater.* **21,** 682–694 (2009).

75. Banerjee, S. & Wong, S. S. Synthesis and Characterization of Carbon Nanotube − Nanocrystal Heterostructures. *Nano Lett* **2,** 195–200 (2002).

76. Hu, H. *et al.* Microwave-assisted covalent modification of graphene nanosheets with chitosan and its electrorheological characteristics. *Appl. Surf. Sci.* **257,** 2637–2642 (2011).

77. Freeley, M. *et al.* Site-Specific One-to-One Click Coupling of Single Proteins to

Individual Carbon Nanotubes: A Single-Molecule Approach. *J. Am. Chem. Soc.* **139,** 17834–17840 (2017).

78. Xu, Y. *et al.* A graphene hybrid material covalently functionalized with porphyrin: Synthesis and optical limiting property. *Adv. Mater.* **21,** 1275–1279 (2009).

79. Chen, J. *et al.* Functionalized Single-Walled Carbon Nanotubes as Rationally Designed Vehicles for Tumor-Targeted Drug Delivery. *J. Am. Chem. Soc.* **130,** 16778–16785 (2008).

80. Lotya, M., King, P. J., Khan, U., De, S. & Coleman, J. N. High-Concentration, Surfactant- Stabilized Graphene Dispersions. *ACS Nano* **4,** 3155–3162 (2010).

81. Yuan, W. Z. *et al.* Wrapping carbon nanotubes in pyrene-containing poly(phenylacetylene) chains: Solubility, stability, light emission, and surface photovoltaic properties. *Macromolecules* **39,** 8011–8020 (2006).

82. Ernst, F., Heek, T., Setaro, A., Haag, R. & Reich, S. Energy Transfer in Nanotube-Perylene Complexes. *Adv. Funct. Mater.* **22,** 3921–3926 (2012).

83. Ehli, C. *et al.* Manipulating single-wall carbon nanotubes by chemical doping and charge transfer with perylene dyes. *Nat. Chem.* **1,** 243–249 (2009).

84. Han, X., Li, Y. & Deng, Z. DNA-wrapped single-walled carbon nanotubes as rigid templates for assembling linear gold nanoparticle arrays. *Adv. Mater.* **19,** 1518–1522 (2007).

85. A. P. Alivisatos. Semiconductor Clusters , Nanocrystals , and Quantum Dots. *Science* **271,** 933–937 (1996).

86. Brus, L. E. Electron-electron and electron-hole interactions in small semiconductor crystallites : The size dependence of the lowest excited electronic state. *J. Chem. Phys.* **80,** 4403 (1984).

87. Bera, D., Qian, L., Tseng, T.-K. & Holloway, P. H. Quantum Dots and Their Multimodal Applications: A Review. *Materials (Basel).* **3,** 2260–2345 (2010).

88. Nozik, A. J. Quantum dot solar cells. *Phys. E* **14,** 115–120 (2002).

89. Efros, A. L. & Nesbitt, D. J. Origin and control of blinking in quantum dots. *Nat. Nanotechnol.* **11,** 661–671 (2016).

90. Efros, A. L. Interband absorption of light in a semicon- ductor sphere. *Sov Phys Semicond* **16,** 772–775 (1982).

91. Brus, L. E. A simple model for the ionization potential, electron affinity, and aqueous redox potentials of small semiconductor crystallites. *J. Chem. Phys.* **79,** 5566 (1983).

92. Weidman, M. C., Beck, M. E., Hoffman, R. S., Prins, F. & Tisdale, W. A. Monodisperse, Air-Stable PbS Nanocrystals *via* Precursor Stoichiometry Control. *ACS Nano* **8,** 6363–6371 (2014).

93. Efros, A. L. & Rosen, M. The electronic structure of semiconductive nanocrystals. *Annu. Rev. Mater. Sci.* **30,** 475–521 (2000).

94. Murray, C. B., Kagan, C. R. & Bawendi, M. G. Synthesis and Characterization of Manodisperse Nanocrystas and Close-Packed Nanocrystal Assemblies. *Annu. Rev. Mater. Sci.* **30,** 545–610 (2000).

95. Reiss, P., Protière, M. & Li, L. Core/shell semiconductor nanocrystals. *Small* **5,** 154–168 (2009).

96. Nirmal, M. *et al.* Fluorescence intermittency in single cadmium selenide nanocrystals. *Nature* **383,** 802–804 (1996).

97. Galland, C. *et al.* Two types of luminescence blinking revealed by spectroelectrochemistry of single quantum dots. *Nature* **479,** 203–207 (2011).

98. Kuno, M., Fromm, D. P., Hamann, H. F., Gallagher, a. & Nesbitt, D. J. Nonexponential "blinking" kinetics of single CdSe quantum dots: A universal power law behavior. *J. Chem. Phys.* **112,** 3117 (2000).

99. Oelsner, C., Antonia Herrero, M., Ehli, C., Prato, M. & Guldi, D. M. Charge transfer events in semiconducting single-wall carbon nanotubes. *J. Am. Chem. Soc.* **133,** 18696–18706 (2011).

100. Banerjee, S. & Wong, S. S. In-Situ Growth of 'Fused', Ozonized Single-Walled Carbon Nanotube - CdTe Quantum Dot Junctions. *Adv. Mater.* **16,** 34–37 (2004).

101. Banerjeet, S. & Wong, S. S. In situ quantum dot growth on multiwalled carbon nanotubes. *J. Am. Chem. Soc.* **125,** 10342–10350 (2003).

102. Raghuveer, M. S., Agrawal, S., Bishop, N. & Ramanath, G. Microwave-assisted

single-step functionalization and in situ derivatization of carbon nanotubes with gold nanoparticles. *Chem. Mater.* **18,** 1390–1393 (2006).

103. Chang, X., Dong, L., Yin, Y. & Sun, S. A novel composite photocatalyst based on in situ growth of ultrathin tungsten oxide nanowires on graphene oxide sheets. *RSC Adv.* **3,** 15005 (2013).

104. Dai, K. *et al.* In situ assembly of MnO2 nanowires/graphene oxide nanosheets composite with high specific capacitance. *Electrochim. Acta* **116,** 111–117 (2014).

105. Eder, D. & Windle, A. H. Carbon-inorganic hybrid materials: The carbon-nanotube/TiO2 interface. *Adv. Mater.* **20,** 1787–1793 (2008).

106. May, V. & Kühn, O. *Charge and energy transfer dynamics in molecular systems*. (Wiley-VCH, 2011).

107. Swathi, R. S. & Sebastian, K. L. Excitation energy transfer from a fluorophore to single-walled carbon nanotubes. *J. Chem. Phys.* **132,** 104502 (2010).

108. Marcus, R. A. On the Theory of Electron-Transfer Reactions. VI. Unified Treatment for Homogeneous and Electrode Reactions. *J. Chem. Phys.* **43,** 679–701 (1965).

109. Binnig, G. & Quate, C. F. Atomic Force Microscope. *Phys. Rev. Lett.* **56,** 930–933 (1986).

110. Grabolle, M. *et al.* Determination of the fluorescence quantum yield of quantum dots: Suitable procedures and achievable uncertainties. *Anal. Chem.* **81,** 6285–6294 (2009).

111. Rurack, K. & Spieles, M. Fluorescence quantum yields of a series of red and near-infrared dyes emitting at 600-1000 nm. *Anal. Chem.* **83,** 1232–1242 (2011).

112. Ferrari, A. C. & Basko, D. M. SI-Raman spectroscopy as a versatile tool for studying the properties of graphene. *Nat. Nanotechnol.* **8,** 235–246 (2013).

113. Huang, X., Mclean, R. S. & Zheng, M. High-resolution length sorting and purification of DNA-wrapped carbon nanotubes by size-exclusion chromatography. *Anal. Chem.* **77,** 6225–6228 (2005).

114. Khripin, C. Y., Tu, X., Howarter, J., Fagan, J. & Zheng, M. Concentration measurement of length-fractionated colloidal single-wall carbon nanotubes. *Anal.*

Chem. **84,** 8733–8739 (2012).

115. Talapin, D. V., Lee, J.-S., Kovalenko, M. V. & Shevchenko, E. V. Prospects of Colloidal Nanocrystals for Electronic and Optoelectronic Applications. *Chem. Rev.* **110,** 389–458 (2010).

116. Lan, X., Masala, S. & Sargent, E. H. Charge-extraction strategies for colloidal quantum dot photovoltaics. *Nat. Mater.* **13,** 233–40 (2014).

117. Kramer, I. J. & Sargent, E. H. The Architecture of Colloidal Quantum Dot Solar Cells: Materials to Devices. *Chem. Rev.* **114,** 863–882 (2014).

118. Robel, I., Bunker, B. a. & Kamat, P. V. Single-Walled Carbon Nanotube-CdS Nanocomposites as Light-Harvesting Assemblies: Photoinduced Charge-Transfer Interactions. *Adv. Mater.* **17,** 2458–2463 (2005).

119. Hu, L. *et al.* Light-Induced Charge Transfer in Pyrene/CdSe-SWNT Hybrids. *Adv. Mater.* **20,** 939–946 (2008).

120. Jeong, S., Shim, H. C., Kim, S. & Han, C.-S. Efficient Electron Transfer in Functional Assemblies of Pyridine-Modified NQDs on SWNTs. *ACS Nano* **4,** 324–330 (2010).

121. Hao, F. *et al.* High Electrocatalytic Activity of Vertically Aligned Single-Walled Carbon Nanotubes towards Sulfide Redox Shuttles. *Sci. Rep.* **2,** 368 (2012).

122. Sharf, T. *et al.* Single Electron Charge Sensitivity of Liquid-Gated Carbon Nanotube Transistors. *Nano Lett.* **14,** 4925–4930 (2014).

123. Sheeney-Haj-Ichia, L., Basnar, B. & Willner, I. Efficient Generation of Photocurrents by Using CdS/Carbon Nanotube Assemblies on Electrodes. *Angew. Chemie* **117,** 80–85 (2005).

124. Batmunkh, M., Biggs, M. J. & Shapter, J. G. Carbon Nanotubes for Dye-Sensitized Solar Cells. *Small* **11,** 2963–2989 (2015).

125. Li, C. *et al.* Photovoltaic Property of a Vertically Aligned Carbon Nanotube Hexagonal Network Assembled with CdS Quantum Dots. *ACS Appl. Mater. Interfaces* **5,** 7400–7404 (2013).

126. Kim, Y. K. & Park, H. Light-harvesting multi-walled carbon nanotubes and CdS hybrids: Application to photocatalytic hydrogen production from water. *Energy*

Environ. Sci. **4,** 685–694 (2011).

127. Cui, D. *et al.* Self-Assembly of Quantum Dots and Carbon Nanotubes for Ultrasensitive DNA and Antigen Detection. *Anal. Chem.* **80,** 7996–8001 (2008).

128. Li, X., Qin, Y., Picraux, S. T. & Guo, Z.-X. Noncovalent assembly of carbon nanotube-inorganic hybrids. *J. Mater. Chem.* **21,** 7527 (2011).

129. Zbydniewska, E. *et al.* Charge Blinking Statistics of Semiconductor Nanocrystals Revealed by Carbon Nanotube Single Charge Sensors. *Nano Lett.* **15,** 6349–6356 (2015).

130. Georgakilas, V. *et al.* Decorating carbon nanotubes with metal or semiconductor nanoparticles. *J. Mater. Chem.* **17,** 2679 (2007).

131. Peng, X., Chen, J., Misewich, J. a & Wong, S. S. Carbon nanotube-nanocrystal heterostructures. *Chem. Soc. Rev.* **38,** 1076–98 (2009).

132. Del Canto, E. *et al.* Critical investigation of defect site functionalization on single-walled carbon nanotubes. *Chem. Mater.* **23,** 67–74 (2011).

133. Tasis, D., Tagmatarchis, N., Bianco, A. & Prato, M. Chemistry of Carbon Nanotubes. *Chem. Rev.* **106,** 1105–1136 (2006).

134. Salzmann, C. G. *et al.* The Role of Carboxylated Carbonaceous Fragments in the Functionalization and Spectroscopy of a Single-Walled Carbon-Nanotube Material. *Adv. Mater.* **19,** 883–887 (2007).

135. Zhang, J. *et al.* Effect of Chemical Oxidation on the Structure of Single-Walled Carbon Nanotubes. *J. Phys. Chem. B* **107,** 3712–3718 (2003).

136. Haremza, J. M., Hahn, M. a., Krauss, T. D., Chen, S. & Calcines, J. Attachment of Single CdSe Nanocrystals to Individual Single-Walled Carbon Nanotubes. *Nano Lett.* **2,** 1253–1258 (2002).

137. Ravindran, S., Chaudhary, S., Colburn, B., Ozkan, M. & Ozkan, C. S. Covalent Coupling of Quantum Dots to Multiwalled Carbon Nanotubes for Electronic Device Applications. *Nano Lett.* **3,** 447–453 (2003).

138. Jennifer F. Campbell, Ingrid Tessmer,† H. Holden Thorp, and D. A. E. Atomic Force Microscopy Studies of DNA-Wrapped Carbon Nanotube Structure and Binding to Quantum Dots. *J Am Chem Sos* **130,** 10648–10655 (2008).

139. Zhou, Z. *et al.* Water-soluble DNA-wrapped single-walled carbon-nanotube/quantum-dot complexes. *Small* **5,** 2149–55 (2009).

140. Zhu, J. *et al.* Solution-Processable Carbon Nanoelectrodes for Single-Molecule Investigations. *J. Am. Chem. Soc* **138,** 2905−2908 (2016).

141. Olde Damink, L. H. H. *et al.* Cross-linking of dermal sheep collagen using a water-soluble carbodiimide. *Biomaterials* **17,** 765–773 (1996).

142. Williams, A. & Ibrahim, I. T. Carbodiimide Chemistry: Recent Advances. *Chem. Rev.* **81,** 589–636 (1981).

143. Nakajima, N. & Ikada, Y. Mechanism of Amide Formation by Carbodiimide for Bioconjugation in Aqueous Media. *Bioconjug. Chem.* **6,** 123–130 (1995).

144. Bott, R. *Bioconjugate Techniques*. (Elsevier, 2014).

145. Staros, J. V., Wright, R. W. & Swingle, D. M. Enhancement by N-hydroxysulfosuccinimide of water-soluble carbodiimide-mediated coupling reactions. *Anal. Biochem.* **156,** 220–222 (1986).

146. Peng, X., Misewich, J. a, Wong, S. S. & Sfeir, M. Y. Efficient charge separation in multidimensional nanohybrids. *Nano Lett.* **11,** 4562–8 (2011).

147. Biju, V., Itoh, T., Baba, Y. & Ishikawa, M. Quenching of photoluminescence in conjugates of quantum dots and single-walled carbon nanotube. *J. Phys. Chem. B* **110,** 26068–26074 (2006).

148. Shafran, E., Mangum, B. D. & Gerton, J. M. Energy transfer from an individual quantum dot to a carbon nanotube. *Nano Lett.* **10,** 4049–54 (2010).

149. Pan, B. *et al.* Effects of Carbon Nanotubes on Photoluminescence Properties of Quantum Dots. *J. Phys. Chem. C* **112,** 939–944 (2008).

150. Dresselhaus, M. S. & Eklund, P. C. Phonons in carbon nanotubes. *Adv. Phys.* **49,** 705–814 (2000).

151. Wang, X., Qu, L., Zhang, J., Peng, X. & Xiao, M. Surface-related emission in highly luminescent CdSe quantum dots. *Nano Lett.* **3,** 1103–1106 (2003).

152. Schlegel, G., Bohnenberger, J., Potapova, I. & Mews, A. Fluorescence Decay Time of Single Semiconductor Nanocrystals. *Phys. Rev. Lett.* **88,** 4 (2002).

153. Jha, P. P. & Guyot-Sionnest, P. Trion decay in colloidal quantum dots. *ACS Nano* **3,** 1011–1015 (2009).

154. Shimizu, K. *et al.* Blinking statistics in single semiconductor nanocrystal quantum dots. *Phys. Rev. B* **63,** 1–5 (2001).

155. Abramson, J., Palma, M., Wind, S. J. & Hone, J. Quantum dot nanoarrays: Self-assembly with single-particle control and resolution. *Adv. Mater.* **24,** 2207–2211 (2012).

156. Crouch, C. H. *et al.* Facts and artifacts in the blinking statistics of semiconductor nanocrystals. *Nano Lett.* **10,** 1692–1698 (2010).

157. Xu, Z. & Cotlet, M. Photoluminenscence blinking dynamics of colloidal quantum dots in the presence of controlled external electron traps. *Small* **8,** 253–258 (2012).

158. Jin, S. & Lian, T. Electron transfer dynamics from single CdSe/ZnS quantum dots to TiO2 nanoparticles. *Nano Lett.* **9,** 2448–2454 (2009).

159. Xu, Z. & Cotlet, M. Quantum Dot-Bridge-Fullerene Heterodimers with Controlled Photoinduced Electron Transfer. *Angew. Chemie Int. Ed.* **50,** 6079–6083 (2011).

160. Federspiel, F. *et al.* Distance Dependence of the Energy Transfer Rate from a Single Semiconductor Nanostructure to Graphene. *Nano Lett.* **15,** 1252–1258 (2015).

161. Freeley, M. *et al.* Site-Specific One-to-One Click Coupling of Single Proteins to Individual Carbon Nanotubes: A Single-Molecule Approach. *J. Am. Chem. Soc.* **139,** 17834–17840 (2017).

162. Holland, J. T., Lau, C., Brozik, S., Atanassov, P. & Banta, S. Engineering of Glucose Oxidase for Direct Electron Transfer via Site-Specific Gold Nanoparticle Conjugation. *J. Am. Chem. Soc.* **133,** 19262–19265 (2011).

163. Nag, O. K. *et al.* Quantum Dot–Peptide–Fullerene Bioconjugates for Visualization of *in Vitro* and *in Vivo* Cellular Membrane Potential. *ACS Nano* **11,** 5598–5613 (2017).

164. Bang, J. H. & Kamat, P. V. CdSe Quantum Dot–Fullerene Hybrid Nanocomposite for Solar Energy Conversion: Electron Transfer and Photoelectrochemistry. *ACS Nano* **5,** 9421–9427 (2011).

165. Bareket, L. *et al.* Semiconductor Nanorod–Carbon Nanotube Biomimetic Films for Wire-Free Photostimulation of Blind Retinas. *Nano Lett.* **14,** 6685–6692 (2014).

166. Chinta, J. P. *et al.* Carbon Nanotube and Semiconductor Nanorods Hybrids: Preparation, Characterization, and Evaluation of Photocurrent Generation. *Langmuir* **33,** 5519–5526 (2017).

167. Jiang, K. *et al.* Selective Attachment of Gold Nanoparticles to Nitrogen-Doped Carbon Nanotubes. *Nano Lett.* **3,** 275–277 (2003).

168. Ravindran, S., Chaudhary, S., Colburn, B., Ozkan, M. & Ozkan, C. S. Covalent Coupling of Quantum Dots to Multiwalled Carbon Nanotubes for Electronic Device Applications. *Nano Lett* **3,** 447–453 (2003).

169. Hu, J. *et al.* Efficient method to functionalize carbon nanotubes with thiol groups and fabricate gold nanocomposites. *Chem. Phys. Lett.* **401,** 352–356 (2005).

170. Han, X., Li, Y. & Deng, Z. DNA-Wrapped Single Walled Carbon Nanotubes as Rigid Templates for Assembling Linear Gold Nanoparticle Arrays. *Adv. Mater.* **19,** 1518–1522 (2007).

171. Georgakilas, V. *et al.* Decorating carbon nanotubes with metal or semiconductor nanoparticles. *J. Mater. Chem.* **17,** 2679 (2007).

172. Weizmann, Y., Chenoweth, D. M. & Swager, T. M. DNA−CNT Nanowire Networks for DNA Detection. *J. Am. Chem. Soc.* **133,** 3238–3241 (2011).

173. Vedala, H. *et al.* The effect of environmental factors on the electrical conductivity of a single oligo-DNA molecule measured using single-walled carbon nanotube nanoelectrodes. *Nanotechnology* **19,** 265704 (2008).

174. Lyonnais, S. *et al.* DNA-Carbon Nanotube Conjugates Prepared by a Versatile Method Using Streptavidin-Biotin Recognition. *Small* **4,** 442–446 (2008).

175. Nepal, D. & Geckeler, K. E. Proteins and Carbon Nanotubes: Close Encounter in Water. *Small* **3,** 1259–1265 (2007).

176. Guo, X., Gorodetsky, A. A., Hone, J., Barton, J. K. & Nuckolls, C. Conductivity of a single DNA duplex bridging a carbon nanotube gap. *Nat. Nanotechnol.* **3,** 163–167 (2008).

177. Wang, L. *et al.* Ligand-induced dependence of charge transfer in nanotube–

quantum dot heterostructures. *Nanoscale* **8,** 15553–15570 (2016).

178. Si, H.-Y., Liu, C.-H., Xu, H., Wang, T.-M. & Zhang, H.-L. Shell-Controlled Photoluminescence in CdSe/CNT Nanohybrids. *Nanoscale Res. Lett.* **4,** 1146–1152 (2009).

179. Grzelczak, M. *et al.* Photoluminescence Quenching Control in Quantum Dot–Carbon Nanotube Composite Colloids Using a Silica-Shell Spacer. *Adv. Mater.* **18,** 415–420 (2006).

180. Shafran, E., Mangum, B. D. & Gerton, J. M. Energy Transfer from an Individual Quantum Dot to a Carbon Nanotube. *Nano Lett.* **10,** 4049–4054 (2010).

181. Chen, Z., Berciaud, S., Nuckolls, C., Heinz, T. F. & Brus, L. E. Energy Transfer from Individual Semiconductor Nanocrystals to Graphene. *ACS Nano* **4,** 2964–2968 (2010).

182. Attanzio, A. *et al.* Carbon Nanotube-Quantum Dot Nanohybrids: Coupling with Single-Particle Control in Aqueous Solution. *Small* **13,** 1603042 (2017).

183. Mirkin, C. A., Letsinger, R. L., Mucic, R. C. & Storhoff, J. J. A DNA-based method for rationally assembling nanoparticles into macroscopic materials. *Nature* **382,** 607–609 (1996).

184. Alivisatos, A. P. *et al.* Organization of 'nanocrystal molecules' using DNA. *Nature* **382,** 609–611 (1996).

185. Jones, M. R., Seeman, N. C. & Mirkin, C. A. Programmable materials and the nature of the DNA bond. *Science* **347,** 840 (2015).

186. O'Brien, M. N., Lin, H.-X., Girard, M., Olvera de la Cruz, M. & Mirkin, C. A. Programming Colloidal Crystal Habit with Anisotropic Nanoparticle Building Blocks and DNA Bonds. *J. Am. Chem. Soc.* **138,** 14562–14565 (2016).

187. Mason, J. A. *et al.* Contraction and Expansion of Stimuli-Responsive DNA Bonds in Flexible Colloidal Crystals. *J. Am. Chem. Soc.* **138,** 8722–8725 (2016).

188. Qian, Z. & Ginger, D. S. Reversibly Reconfigurable Colloidal Plasmonic Nanomaterials. *J. Am. Chem. Soc.* **139,** 5266–5276 (2017).

189. Lermusiaux, L., Sereda, A., Portier, B., Larquet, E. & Bidault, S. Reversible Switching of the Interparticle Distance in DNA-Templated Gold Nanoparticle

Dimers. *ACS Nano* **6,** 10992–10998 (2012).

190. Aldaye, F. A. & Hanadi F., S. Modular Access to Structurally Switchable 3D Discrete DNA Assemblies. *J. Am. Chem. Soc* **129,** 13376–13377 (2007).

191. Maye, M. M., Kumara, M. T., Nykypanchuk, D., Sherman, W. B. & Gang, O. Switching binary states of nanoparticle superlattices and dimer clusters by DNA strands. *Nat. Nanotechnol.* **5,** 116–120 (2010).

192. Cui, D. *et al.* Self-Assembly of Quantum Dots and Carbon Nanotubes for Ultrasensitive DNA and Antigen Detection. *Anal. Chem.* **80,** 7996–8001 (2008).

193. Campbell, J. F., Tessmer, I., Thorp, H. H. & Erie, D. A. Atomic Force Microscopy Studies of DNA-Wrapped Carbon Nanotube Structure and Binding to Quantum Dots. *J. Am. Chem. Soc.* **130,** 10648–10655 (2008).

194. Zhou, Z. *et al.* Water-Soluble DNA-Wrapped Single-Walled Carbon-Nanotube/Quantum-Dot Complexes. *Small* **5,** 2149–2155 (2009).

195. Clémence Allain, David, M. & Teulade-Fichou, M.-P. FRET Templated by G-Quadruplex DNA: A Specific Ternary Interaction Using an Original Pair of Donor/Acceptor Partners. *J. Am. Chem. Soc* **128,** 11890–11893 (2006).

196. Weber, P. C., Ohlendorf, D. H., Wendoloski, J. J. & Salemme, F. R. Structural origins of high-affinity biotin binding to streptavidin. *Science* **243,** 85–8 (1989).

197. Michael Green, N. Avidin and streptavidin. *Methods Enzymol.* **184,** 51–67 (1990).

198. Riesz, P. & Kondo, T. Free radical formation induced by ultrasound and its biological implications. *Free Radic. Biol. Med.* **13,** 247–270 (1992).

199. Kaempgen, M., Lebert, M., Haluska, M., Nicoloso, N. & Roth, S. Sonochemical Optimization of the Conductivity of Single Wall Carbon Nanotube Networks. *Adv. Mater.* **20,** 616–620 (2008).

200. Palma, M. *et al.* Controlled Formation of Carbon Nanotube Junctions via Linker-Induced Assembly in Aqueous Solution. *J. Am. Chem. Soc.* **135,** 8440–8443 (2013).

201. Attanzio, A. *et al.* Carbon Nanotube-Quantum Dot Nanohybrids: Coupling with Single Particle Control in Aqueous Solution. *Small* **13,** 1603042 (2017).

202. Tong, L. *et al.* Recent progress in the preparation and application of quantum dots/graphene composite materials. *RSC Adv.* **7,** 47999–48018 (2017).

203. Cao, A. *et al.* A facile one-step method to produce graphene-CdS quantum dot nanocomposites as promising optoelectronic materials. *Adv. Mater.* **22,** 103–106 (2010).

204. Li, N., Cao, M. & Hu, C. Review on the latest design of graphene-based inorganic materials. *Nanoscale* **4,** 6205 (2012).

205. Geim, A. K. Graphene: Status and Prospects. *Science* **324,** 1530–1534 (2009).

206. Ferrari, A. C. *et al.* Science and technology roadmap for graphene, related two-dimensional crystals, and hybrid systems. *Nanoscale* **7,** 4598–4810 (2015).

207. Yeh, T.-F., Teng, C.-Y., Chen, L.-C., Chen, S.-J. & Teng, H. Graphene oxide-based nanomaterials for efficient photoenergy conversion. *J. Mater. Chem. A* **4,** 2014–2048 (2016).

208. Guo, W. *et al.* Oxygen-assisted charge transfer between ZnO quantum dots and graphene. *Small* **9,** 3031–3036 (2013).

209. Sun, Z. *et al.* Infrared photodetectors based on CVD-grown graphene and PbS quantum dots with ultrahigh responsivity. *Adv. Mater.* **24,** 5878–5883 (2012).

210. Sun, Y.-L. *et al.* Hybrid graphene/cadmium-free ZnSe/ZnS quantum dots phototransistors for UV detection. *Sci. Rep.* **8,** 5107 (2018).

211. Radich, J. G., Dwyer, R. & Kamat, P. V. Cu_2S Reduced Graphene Oxide Composite for High-Efficiency Quantum Dot Solar Cells. Overcoming the Redox Limitations of S_2^-/S_n^{2-} at the Counter Electrode. *J. Phys. Chem. Lett.* **2,** 2453–2460 (2011).

212. Sun, Y., Wu, Q. & Shi, G. Graphene based new energy materials. *Energy Environ. Sci.* **4,** 1113 (2011).

213. Konstantatos, G. *et al.* Hybrid graphene-quantum dot phototransistors with ultrahigh gain. *Nat. Nanotechnol.* **7,** 363–368 (2012).

214. Klekachev, A. V. *et al.* Electron accumulation in graphene by interaction with optically excited quantum dots. *Phys. E Low-Dimensional Syst. Nanostructures* **43,** 1046–1049 (2011).

215. Gravagnuolo, A. M. *et al.* On-the-Spot Immobilization of Quantum Dots, Graphene Oxide, and Proteins via Hydrophobins. *Adv. Funct. Mater.* **25,** 6084–6092 (2015).

216. Bu, Y., Chen, Z., Li, W. & Hou, B. Highly efficient photocatalytic performance of graphene-ZnO quasi-shell-core composite material. *ACS Appl. Mater. Interfaces* **5,** 12361–12368 (2013).

217. Chen, D., Zhang, H., Liu, Y. & Li, J. Graphene and its derivatives for the development of solar cells, photoelectrochemical, and photocatalytic applications. *Energy Environ. Sci.* **6,** 1362 (2013).

218. Xiao, F. X., Miao, J. & Liu, B. Layer-by-layer self-assembly of CdS quantum dots/graphene nanosheets hybrid films for photoelectrochemical and photocatalytic applications. *J. Am. Chem. Soc.* **136,** 1559–1569 (2014).

219. Bepete, G. *et al.* Surfactant-free single-layer graphene in water. *Nat. Chem.* **9,** 347–352 (2017).

220. Liu, J., Tang, J. & Gooding, J. J. Strategies for chemical modification of graphene and applications of chemically modified graphene. *J. Mater. Chem.* **22,** 12435 (2012).

221. Rosillo-Lopez, M., Lee, T. J., Bella, M., Hart, M. & Salzmann, C. G. Formation and chemistry of carboxylic anhydrides at the graphene edge. *RSC Adv.* **5,** 104198–104202 (2015).

222. Salzmann, C. G., Nicolosi, V. & Green, M. L. H. Edge-carboxylated graphene nanoflakes from nitric acid oxidised arc-discharge material. *J. Mater. Chem.* **20,** 314–319 (2010).

223. Rosillo-Lopez, M., Lee, T. J., Bella, M., Hart, M. & Salzmann, C. G. Formation and chemistry of carboxylic anhydrides at the graphene edge. *RSC Adv.* **5,** 104198–104202 (2015).

224. Chen, Z., Berciaud, S., Nuckolls, C., Heinz, T. F. & Brus, L. E. Energy transfer from individual semiconductor nanocrystals to graphene. *ACS Nano* **4,** 2964–8 (2010).

225. Guo, C. X. *et al.* Layered graphene/quantum dots for photovoltaic devices. *Angew. Chemie - Int. Ed.* **49,** 3014–3017 (2010).

226. Lightcap, I. V. & Kamat, P. V. Fortification of CdSe quantum dots with graphene oxide. Excited state interactions and light energy conversion. *J. Am. Chem. Soc.* **134,** 7109–7116 (2012).

227. Kim, B. S. *et al.* High Performance PbS Quantum Dot/Graphene Hybrid Solar Cell with Efficient Charge Extraction. *ACS Appl. Mater. Interfaces* **8,** 13902–13908 (2016).

228. Butler, P. J., Harris, J. I., Hartley, B. S. & Lebeman, R. The use of maleic anhydride for the reversible blocking of amino groups in polypeptide chains. *Biochem. J.* **112,** 679–89 (1969).

229. Yurkanis Bruice, P. *Organic Chemistry, 5th Edition*. (Pearson).

230. Yan, J., Zhang, Y., Kim, P. & Pinczuk, A. Electric field effect tuning of electron-phonon coupling in graphene. *Phys. Rev. Lett.* **98,** 1–4 (2007).

231. Das, A. *et al.* Monitoring dopants by Raman scattering in an electrochemically top-gated graphene transistor. *Nat. Nanotechnol.* **3,** 210–215 (2008).

232. Das, B., Voggu, R., Rout, C. S. & Rao, C. N. R. Changes in the electronic structure and properties of graphene induced by molecular charge-transfer. *Chem. Commun.* 5155–5157 (2008).

233. Liu, H., Liu, Y. & Zhu, D. Chemical doping of graphene. *J. Mater. Chem.* **21,** 3335–3345 (2011).

234. Misseeuw, L. *et al.* Optical-quality controllable wet-chemical doping of graphene through a uniform, transparent and low-roughness F4-TCNQ/MEK layer. *RSC Adv.* **6,** 104491–104501 (2016).

235. Lee, S. *et al.* Flexible organic solar cells composed of P3HT:PCBM using chemically doped graphene electrodes. *Nanotechnology* **23,** 344013 (2012).

236. Howard, C. A., Dean, M. P. M. & Withers, F. Phonons in potassium-doped graphene: The effects of electron-phonon interactions, dimensionality, and adatom ordering. *Phys. Rev. B - Condens. Matter Mater. Phys.* **84,** 1–4 (2011).

237. Markad, G. B., Battu, S., Kapoor, S. & Haram, S. K. Interaction between quantum dots of CdTe and reduced graphene oxide: Investigation through cyclic voltammetry and spectroscopy. *J. Phys. Chem. C* **117,** 20944–20950 (2013).

238. Hu, L. *et al.* Graphene Doping Improved Device Performance of ZnMgO/PbS Colloidal Quantum Dot Photovoltaics. *Adv. Funct. Mater.* **26,** 1899–1907 (2016).

239. Rao, A. M., Eklund, P. C., Bandow, S., Thess, A. & Smalley, R. E. Evidence for charge transfer in doped carbon nanotube bundles from Raman scattering. *Nature* **388,** 257–259 (1997).

240. O'Regan, B. & Grätzel, M. A low-cost, high-efficiency solar cell based on dye-sensitized colloidal TiO2 films. *Nature* **353,** 737–740 (1991).

241. Wu, Q. *et al.* Impacts of Reduced Graphene Oxide in CdS/CdSe Quantum Dots Co-sensitized Solar Cells. *J. Phys. Chem. C* **121,** 18430–18438 (2017).

242. Zhu, N. *et al.* Sandwiched confinement of quantum dots in graphene matrix for efficient electron transfer and photocurrent production. *Sci. Rep.* **5,** 1–14 (2015).

243. Brown, P. & Kamat, P. V. Quantum dot solar cells. Electrophoretic deposition of CdSe-C60 composite films and capture of photogenerated electrons with nC60 cluster shell. *J. Am. Chem. Soc.* **130,** 8890–8891 (2008).

244. Georgakilas, V. *et al.* Functionalization of graphene: Covalent and non-covalent approaches, derivatives and applications. *Chem. Rev.* **112,** 6156–6214 (2012).

245. Han, S. J., Garcia, A. V., Oida, S., Jenkins, K. A. & Haensch, W. Graphene radio frequency receiver integrated circuit. *Nat. Commun.* **5,** 1–6 (2014).

246. Schwierz, F. Graphene transistors. *Nat. Nanotechnol.* **5,** 487 (2010).

247. Shao, Y. *et al.* Graphene based electrochemical sensors and biosensors: A review. *Electroanalysis* **22,** 1027–1036 (2010).

248. Prins, F. *et al.* Room-Temperature Gating of Molecular Junctions Using Few-Layer Graphene Nanogap Electrodes. *Nano Lett.* **11,** 4607–4611 (2011).

249. Xu, Q. *et al.* Single Electron Transistor with Single Aromatic Ring Molecule Covalently Connected to Graphene Nanogaps. *Nano Lett.* **17,** 5335–5341 (2017).

250. Mol, J. A. *et al.* Graphene-porphyrin single-molecule transistors. *Nanoscale* **7,** 13181–13185 (2015).

251. Lau, C. S., Mol, J. A., Warner, J. H. & Briggs, G. A. D. Nanoscale control of graphene electrodes. *Phys. Chem. Chem. Phys.* **16,** 20398–20401 (2014).

252. Prins, F. *et al.* Room-temperature gating of molecular junctions using few-layer graphene nanogap electrodes. *Nano Lett.* **11,** 4607–4611 (2011).

253. Mangin, A., Anthore, A., Della Rocca, M. L., Boulat, E. & Lafarge, P. Reduced work functions in gold electromigrated nanogaps. *Phys. Rev. B* **80,** 235432 (2009).

254. Simmons, J. G. Generalized Formula for the Electric Tunnel Effect between Similar Electrodes Separated by a Thin Insulating Film. *J. Appl. Phys.* **34,** 1793–1803 (1963).

255. Sanderson, C. . & Wilson, D. V. A Simple Method for Coupling Proteins to Insoluble Polysaccharides. *Immunology* **20,** 1061–1065 (1971).

256. Morpurgo, M., Bayer, E. A. & Wilchek, M. N-hydroxysuccinimide carbonates and carbamates are useful reactive reagents for coupling ligands to lysines on proteins. *J. Biochem. Biophys. Methods* **38,** 17–28 (1999).

257. Miron, T. & Wilchek, M. A Simplified Method for the Preparation of Succinimidyl Carbonate Polyethylene Glycol for Coupling to Proteins. *Bioconjug. Chem.* **4,** 568–569 (1993).

258. Arend, M., Westermann, B. & Risch, N. Modern Variants of the Mannich Reaction. *Angew. Chemie Int. Ed.* **37,** 1044–1070 (1998).

259. Joshi, N. S., Whitaker, L. R. & Francis, M. B. A three-component Mannich-type reaction for selective tyrosine bioconjugation. *J. Am. Chem. Soc.* **126,** 15942–15943 (2004).

260. Jia, X., Campos-Delgado, J., Terrones, M., Meunier, V. & Dresselhaus, M. S. Graphene edges: a review of their fabrication and characterization. *Nanoscale* **3,** 86–95 (2011).

261. Liu, Z., Suenaga, K., Harris, P. J. F. & Iijima, S. Open and Closed Edges of Graphene Layers. *Phys. Rev. Lett.* **102,** 015501–015504 (2009).

262. Hashimoto, A., Suenaga, K., Gloter, A., Urita, K. & Iijima, S. Direct evidence for atomic defects in graphene layers. *Nature* **430,** 870–873 (2004).

263. Zhao, J. *et al.* Direct in situ observations of single Fe atom catalytic processes and anomalous diffusion at graphene edges. *Proc. Natl. Acad. Sci. U. S. A.* **111,** 15641–6 (2014).

264. Matei, D. G. *et al.* Functional Single-Layer Graphene Sheets from Aromatic Monolayers. *Adv. Mater.* **25,** 4146–4151 (2013).

265. Turchanin, A. *et al.* Conversion of Self-Assembled Monolayers into Nanocrystalline Graphene: Structure and Electric Transport. *ACS Nano* **5,** 3896–3904 (2011).

266. Booth, T. J. *et al.* Macroscopic Graphene Membranes and Their Extraordinary Stiffness. *Nano Lett.* **8,** 2442–2446 (2008).

267. Haldar, S., Amorim, R. G., Sanyal, B., Scheicher, R. H. & Rocha, A. R. Energetic stability, STM fingerprints and electronic transport properties of defects in graphene and silicene. *RSC Adv.* **6,** 6702–6708 (2016).

268. Stolyarova, E. *et al.* High-resolution scanning tunneling microscopy imaging of mesoscopic graphene sheets on an insulating surface. *Proc. Natl. Acad. Sci. U. S. A.* **104,** 9209–12 (2007).

269. Yu, Q. *et al.* Control and characterization of individual grains and grain boundaries in graphene grown by chemical vapour deposition. *Nat. Mater.* **10,** 443–449 (2011).

270. Xu, X. *et al.* Reconfigurable Carbon Nanotube Multiplexed Sensing Devices. *Nano Lett.* **18,** 4130–4135 (2018).